



Calhoun: The NPS Institutional Archive
DSpace Repository

Theses and Dissertations

1. Thesis and Dissertation Collection, all items

1999-06

Design and prototype development of a
wireless power transmission system for a
micro air vehicle (MAV)

Vitale, Robert L.

Monterey, California. Naval Postgraduate School

<http://hdl.handle.net/10945/8240>

Downloaded from NPS Archive: Calhoun



<http://www.nps.edu/library>

Calhoun is the Naval Postgraduate School's public access digital repository for research materials and institutional publications created by the NPS community. Calhoun is named for Professor of Mathematics Guy K. Calhoun, NPS's first appointed -- and published -- scholarly author.

Dudley Knox Library / Naval Postgraduate School
411 Dyer Road / 1 University Circle
Monterey, California USA 93943

NPS ARCHIVE
1999.06
VITALE, R.

DUDLEY KNOX LIBRARY
NAVAL POSTGRADUATE SCHOOL
MONTEREY CA 93943

NAVAL POSTGRADUATE SCHOOL MONTEREY, CALIFORNIA



THESIS

**DESIGN AND PROTOTYPE DEVELOPMENT OF
A WIRELESS POWER TRANSMISSION SYSTEM
FOR A MICRO AIR VEHICLE (MAV)**

by

Robert L. Vitale

June 1999

Thesis Advisor:

David C. Jenn

Second Reader:

Jeffrey B. Knorr

Approved for public release; distribution is unlimited.

REPORT DOCUMENTATION PAGE			Form Approved OMB No. 0704-0188.	
Public reporting burden for this collection of information is estimated to average 1 hour per response, including the time for reviewing instruction, searching existing data sources, gathering and maintaining the data needed, and completing and reviewing the collection of information. Send comments regarding this burden estimate or any other aspect of this collection of information, including suggestions for reducing this burden, to Washington Headquarters Services, Directorate for Information Operations and Reports, 1215 Jefferson Davis Highway, Suite 1204, Arlington, VA 22202-4302, and to the Office of Management and Budget, Paperwork Reduction Project (0704-0188) Washington DC 20503.				
1. AGENCY USE ONLY (Leave blank)	2. REPORT DATE June 1999	3. REPORT TYPE AND DATES COVERED Master's Thesis		
4. TITLE AND SUBTITLE Design and prototype development of a wireless power transmission system for a micro air vehicle (MAV)		5. FUNDING NUMBERS		
6. AUTHOR(S) Robert L. Vitale				
7. PERFORMING ORGANIZATION NAME(S) AND ADDRESS(ES) Naval Postgraduate School Monterey, CA 93943-5000		8. PERFORMING ORGANIZATION REPORT NUMBER		
9. SPONSORING/MONITORING AGENCY NAME(S) AND ADDRESS(ES)		10. SPONSORING / MONITORING AGENCY REPORT NUMBER		
11. SUPPLEMENTARY NOTES The views expressed in this thesis are those of the author and do not reflect the official policy or position of the Department of Defense or the U.S. Government.				
12a. DISTRIBUTION / AVAILABILITY STATEMENT Approved for public release; distribution is unlimited.		12b. DISTRIBUTION CODE		
13. ABSTRACT (maximum 200 words) Microwave radiation at 1.0 GHz and 1.3 GHz is used to demonstrate remote powering of a micro air vehicle (MAV). Several prototype microwave rectifier systems were fabricated in microstrip using EEsof® computer aided engineering (CAE) software to assist in their design. Radio frequency (RF) parameters of the rectifiers were measured on a vector network analyzer. RF-to-DC conversion efficiency was measured for several designs and with various circuit loads consisting of lumped elements and DC motors. A peak RF-to-DC conversion efficiency of 33 percent was achieved. MAV antenna designs were investigated by simulating 68 geometries using the GNEC® numerical electromagnetics computer program. Two prototype MAVs were assembled, each consisting of microwave rectifier, antenna and a miniature DC motor. It was demonstrated that a 1.8-Watt, 1.3-GHz microwave signal could power the DC motor at free space distance of 30 inches from transmitting antenna to prototype MAV. Greater operating distances are proposed by using higher transmitting power and antenna gain.				
14. SUBJECT TERMS MAV, Remotely Piloted Vehicle, Surveillance, Wireless Power Transfer, Microwave			15. NUMBER OF PAGES 194	
			16. PRICE CODE	
17. SECURITY CLASSIFICATION OF REPORT Unclassified	18. SECURITY CLASSIFICATION OF THIS PAGE Unclassified	19. SECURITY CLASSIFICATION OF ABSTRACT Unclassified	20. LIMITATION OF ABSTRACT UL	

Approved for public release; distribution is unlimited.

**DESIGN AND PROTOTYPE DEVELOPMENT OF A
WIRELESS POWER TRANSMISSION SYSTEM FOR A
MICRO AIR VEHICLE (MAV)**

Robert L. Vitale

DoD Civilian

B.S., California State University Sacramento, 1985

Submitted in partial fulfillment of the
requirements for the degree of

MASTER OF SCIENCE IN ELECTRICAL ENGINEERING

from the

NAVAL POSTGRADUATE SCHOOL

June 1999

ABSTRACT

Microwave radiation at 1.0 GHz and 1.3 GHz is used to demonstrate remote powering of a micro air vehicle (MAV). Several prototype microwave rectifier systems were fabricated in microstrip using EEsof® computer aided engineering (CAE) software to assist in their design. Radio frequency (RF) parameters of the rectifiers were measured on a vector network analyzer. RF-to-DC conversion efficiency was measured for several designs and with various circuit loads consisting of lumped elements and DC motors. A peak RF-to-DC conversion efficiency of 33 percent was achieved. MAV antenna designs were investigated by simulating 68 geometries using the GNEC® numerical electromagnetics computer program. Two prototype MAVs were assembled, each consisting of microwave rectifier, antenna and a miniature DC motor. It was demonstrated that a 1.8-Watt, 1.3-GHz microwave signal could power the DC motor at free space distance of 30 inches from transmitting antenna to prototype MAV. Greater operating distances are proposed by using higher transmitting power and antenna gain.

TABLE OF CONTENTS

I. INTRODUCTION.....	1
A. BACKGROUND.....	1
1. Wireless Power Transmission	1
2. MAV	3
B. PREVIOUS RESEARCH	5
C. OBJECTIVE.....	6
II. RECTIFIER CIRCUIT DESIGN	9
A. RECTIFIER CIRCUIT TOPOLOGY.....	10
B. MICROWAVE DIODE SELECTION	18
1. PN Junction Diode	19
2. Metal Semiconductor (MS) Diodes.....	20
C. PC BOARD CHARACTERIZATION	24
1. Microstrip Fabrication	24
2. Permittivity Determination Circuit (Circuit 3-1).....	25
3. Permittivity Verification Circuit (Circuit 4-1).....	30
D. DIODE CHARACTERIZATION	35
E. COMPUTER VERIFICATION OF SBD CHARACTERISTICS.....	39
F. IMPEDANCE MATCHING THE RECTIFIER CIRCUIT	42
1. Design of Shunt Stub Impedance Matching Circuit.....	43
2. Computer Simulations of Shunt Stub Matching Circuits.....	48
3. Fabrication of Shunt Stub Matching Circuits.....	51
4. VNA Measurement and Analysis for 1.0 GHz Rectifier Circuit (Ckt 6C2)	53
5. VNA Measurement and Analysis for 1.3 GHz Rectifier Circuit (Ckt7d-1 and Ckt 7d-5)	55

G. RECTIFIER CIRCUIT DESIGN - CONCLUSIONS.....	58
III. ANTENNA DESIGN	61
A. ANTENNA TYPE SELECTION	62
B. DIPOLE ANTENNA GEOMETRY.....	63
C. NUMERICAL ELECTROMAGNETIC CODE (NEC) MODELING OF MAV ANTENNA (FAT DIPOLE ANTENNA)	69
1. NEC - Method of Moments Solution Description	70
2. Modeling Rules.....	72
3. MAV Antenna GNEC [®] Input Data File Development.....	75
4. GNEC [®] Model Convergence.....	77
D. GNEC [®] SIMULATIONS TO DESIGN ANTENNA FEED	82
E. GNEC [®] ANTENNA RADIATION PATTERN EVALUATION.....	88
F. ANTENNA FABRICATION.....	90
G. ANTENNA INPUT IMPEDANCE MEASUREMENT.....	93
H. ANTENNA DEVELOPMENT CONCLUSIONS.....	99
IV. RECTIFIER CONVERSION EFFICIENCY MEASUREMENTS.....	101
A. INTRODUCTION.....	101
B. CONVERSION EFFICIENCY MEASUREMENT DESCRIPTION	103
1. Microwave Power Measurements	108
2. Rectified Output Average Power Measurements	110
C. CONVERSION EFFICIENCY MEASUREMENT RESULTS	112
D. SUMMARY OF CONVERSION EFFICIENCY RESULTS	119
1. Minimum Incident Power Requirement.....	119
2. Applied Microwave Power for Peak Rectifier Efficiency	119
3. Efficiency Decrease for Incident Power Above Peak Efficiency	119

4. Multiple SBDs in Parallel Increase the Rectifier's Power Rating	120
5. Circuit Loading Affects the Rectifier Efficiency	120
E. RECOMMENDATIONS TO INCREASE CONVERSION	
EFFICIENCY.....	122
1. Multiple SBDs in Parallel.....	122
2. Addition of a Load Capacitance	122
3. Impedance Match SBD Diodes at the Expected Microwave Power	122
V. OPERATIONAL DEMONSTRATION OF WIRELESS POWER TRANSFER	
THROUGH FREE SPACE.....	123
A. INTRODUCTION.....	123
B. DEMONSTRATION APPARATUS.....	123
1. 1.0 GHz CW Demonstration Apparatus.....	124
2. 1.3 GHz CW and Pulsed CW Demonstration Apparatus	129
3. RF/Microwave Radiation Exposure Limitations to Human	
Personnel.....	133
C. MICROWAVE LINK POWER BUDGET	135
D. FREE SPACE WPT DEMONSTRATION RESULTS	138
E. CONCLUSIONS AND RECOMMENDATIONS.....	139
VI. SUMMARY, CONCLUSIONS, AND RECOMMENDATIONS	141
A. SUMMARY	141
B. CONCLUSIONS	141
C. SUGGESTIONS FOR FURTHER RESEARCH.....	142
1. GaAs Schottky-barrier Diodes.....	143
2. Additional Rectifier Circuit Configurations	143
3. High Powered Sources.....	144
4. MAV Antenna Improvements	144

5. Improved MAV DC Motor.....	145
D. OTHER POTENTIAL INVESTIGATIONS.....	146
APPENDIX A. EESOF LIBRA [®] CIRCUIT MODEL TO DETERMINE PERMITTIVITY OF FR-4 PC BOARD.....	147
APPENDIX B. MICROSTRIP LINE WIDTH CALCULATIONS	149
APPENDIX C. EESOF LIBRA [®] CIRCUIT MODEL FOR MICROSTRIP THROUGH LINE	151
APPENDIX D. DIODE S-PARAMETER CALCULATIONS	153
APPENDIX E. SI-SBD MODEL FILE FOR LIBRA [®]	159
APPENDIX F. EESOF LIBRA [®] CIRCUIT MODEL FOR MICROSTRIP RECTIFIER CIRCUIT.....	161
APPENDIX G. WPT PROPAGATION CALCULATIONS	163
APPENDIX H. LISTING OF POTENTIAL CONDUCTIVE COATING OR THIN FILM SUPPLIERS.....	169
LIST OF REFERENCES	171
INITIAL DISTRIBUTION LIST	173

LIST OF FIGURES

Figure 1. Proposed Remotely Piloted Micro Air Vehicle (MAV).....	4
Figure 2. Proposed Deployment of Wireless Powered MAV.....	5
Figure 3. Assembled MAV, Cutaway to View Components Inside.....	9
Figure 4. Half-Wave Rectifier. (a) Input Signal and Rectified Output. (b) Schematic Diagram.....	12
Figure 5. Full-Wave Rectifier Diode Circuit. (a) Input Signal and Rectified Output. (b) Schematic Diagram.....	13
Figure 6. Full-Wave Bridge Rectifier Circuit. (a) Input Signal and Rectified Output. (b) Schematic Diagram.....	14
Figure 7. Half-Wave Rectifier with Filter Capacitor. (a) Input Signal and Rectified Output. (b) Schematic Diagram.....	15
Figure 8. Illustration of PN Junction Diode.....	19
Figure 9. Silicon Schottky-Barrier Diode (Si-SBD) Hewlett Packard Passivated Hybrid Type.....	21
Figure 10. Illustration of GaAs Schottky-barrier Diode.....	23
Figure 11. VNA Measured Return Loss for 50 ohm Microstrip Through Line (Circuit 3-1).....	27
Figure 12. Circuit 3-1 Return Loss Comparison of VNA Measurements to Libra [®] Calculations using $\epsilon_r = 2.0$	27
Figure 13. Circuit 3-1 Return Loss Comparison of VNA Measurements to Libra [®] Calculations using $\epsilon_r = 3.0$	28
Figure 14. Circuit 3-1 Return Loss Comparison of VNA Measurements to Libra [®] Calculations using $\epsilon_r = 3.5$	28
Figure 15. Circuit 3-1 Return Loss Comparison of VNA Measurements to Libra [®] Calculations using $\epsilon_r = 4.0$	29
Figure 16. Circuit 3-1 Return Loss Comparison of VNA Measurements to Libra [®] Calculations using $\epsilon_r = 5.0$	29

Figure 17. Return Loss (S_{11}) 50 ohm Microstrip through Line. (Circuit 4-1: 111 mil wide line on FR-4 PC Board). (a) Libra [®] Computer Simulation. (b) VNA Measurement.....	33
Figure 18. Impedance Smith Chart for 50 ohm Microstrip Line. (Circuit 4-1: 111 mils wide line on FR-4 PC Board). (a) Libra [®] Computer Simulation. (b) VNA Measurement.....	34
Figure 19. SMT-SBD Characterization Test Fixture (Circuit 4-2).....	35
Figure 20. Return and Insertion Loss for SBD Test Fixture (Circuit 4-2). (a) Libra [®] Computer Simulation. (b) VNA Measurement.	41
Figure 21. Shunt Stub Circuit Illustration.	43
Figure 22. Smith Chart for Shunt Stub Impedance Matching of SMT-SBD Rectifier at 1.0 GHz.	46
Figure 23. Smith Chart for Shunt Stub Impedance Matching of MAV Rectifier Circuit at 1.3 GHz.	47
Figure 24. Circuit 6x2 Return Loss for Libra [®] Model Variation (1.0 GHz Rectifier).	49
Figure 25. Circuit 7x1 Return Loss by Design Model Variation 1.3 GHz Rectifier Circuit.....	50
Figure 26. Circuit 6C2 Return Loss Measurement Setup (1.0 GHz Rectifier Circuit).....	51
Figure 27. Circuit 7d-1 Return Loss Measurement Setup (1.3 GHz Rectifier Circuit).	52
Figure 28. HP8510 Vector Network Analyzer (VNA) Return Loss Measurement Setup.....	52
Figure 29. VNA Measured Return Loss of Ckt 6C2 (1.0 GHz Rectifier Circuit).	53
Figure 30. Measured and Simulated Return Loss for Circuit 6C2 (1.0 GHz Rectifier Circuit).	54
Figure 31. Measured Return Loss and Insertion Loss for Circuit 7D-1 Circuit is Terminated in 50 ohms and 2-Port Calibration Set Used.....	55
Figure 32. Simulated and Measured Return Loss for Ckt 7d-1 Where Port 2 is Terminated in 50 ohms.	56

Figure 33. VNA Measured Return Loss for 1.3 GHz Rectifier Circuit (Ckt 7d-1) Without DC Motor Attached, Port 2 Configured with an Open Circuit and with 50 ohm Termination.	57
Figure 34. VNA Measured Return Loss for 1.3 GHz Rectifier (Ckt 7d-5) Port 2 Terminated with DC Motor and in 50 ohms.	58
Figure 35. Dimensions for MAV Dipole Antenna.	62
Figure 36. Dipole Antenna Radiation Resistance.	65
Figure 37. Calculated Radiation Resistance for a Thin Wire Dipole Antenna at Proposed WPT Frequencies.	65
Figure 38. Radiation Resistance of 10.2 cm long Dipole Antenna as Thickness Varies [Ref 15].	67
Figure 39. Reactance for a 10.2 cm long Dipole Antenna as Thickness Varies [Ref 15].	67
Figure 40. MAV Antenna Model for GNEC [®] Simulations. (a) Wire Frame Model. (b) Wedge Section.	76
Figure 41. MAV Antenna Impedance for GNEC [®] Models with 3, 5 and 9 Segments for the Source Wire Model.	78
Figure 42. Currents for the Detailed GNEC [®] model of a MAV Antenna.	80
Figure 43. Currents for the Simplified GNEC [®] Model of the MAV Antenna.	80
Figure 44. The Calculated Impedance of MAV Antenna for Detailed and Simplified GNEC [®] Models.	81
Figure 45. MAV Antenna Resistance verses Feed Gap Size and Location Computed using GNEC [®] . (a) 1.0 GHz. (b) 1.3 GHz.	83
Figure 46. MAV Antenna Reactance verses Feed Gap Size and Location Computed using GNEC [®] . (a) 1.0 GHz. (b) 1.3 GHz.	84
Figure 47. MAV Antenna Impedance verses Feed Gap Size and Location Computed using GNEC [®] . (a) 1.0 GHz. (b) 1.3 GHz.	85
Figure 48. GNEC Calculated Radiation Pattern for MAV-2 Antenna.	89
Figure 49. Radiation Pattern for a Thin Dipole of Same Length as MAV Antenna.	89

Figure 50. Photographs of Copper Pipe MAV Antenna Disassembled to Show Interior Connections.	90
Figure 51. MAV Antennas, Fabricated from 4.4 cm Diameter Copper Pipe. (a) 1.0 GHz Version (MAV-1). (b) 1.3 GHz Version (MAV-2).	92
Figure 52. VNA Measurements on MAV Antenna.	93
Figure 53. HP8510 VNA Measurement of Return Loss for MAV Antennas. (a) 1.0 GHz Version; Length 13 cm (MAV-1). (b) 1.3 GHz Version; Length 10.2 cm (MAV-2).	94
Figure 54. HP8510 VNA Measurement of VSWR for MAV Antennas. (a) 1.0 GHz Version, Length 13 cm (MAV-1). (b) 1.3 GHz Version, Length 10.2 cm (MAV-2).	95
Figure 55. HP8510 VNA Measurement of MAV Antenna Impedance. (a) 1.0 GHz Version (MAV-1). (b) 1.3 GHz Version (MAV-2).	96
Figure 56. Comparison of VSWR Calculated by GNEC and that Measured by VNA for the 1.3 GHz MAV Antenna (MAV-2). (a) GNEC Calculation. (b) VNA Measurement.	98
Figure 57. Block Diagram of RF-to-DC Conversion Efficiency Measurement CW Input Signal and Chip Resistor Loading.	103
Figure 58. Block Diagram of RF-to-DC Conversion Efficiency Measurement, Pulsed CW Input Signal and Chip Resistor Loading.	106
Figure 59. Block Diagram of RF-to-DC Conversion Efficiency Measurement, Pulsed CW Input Signal and DC Motor Loading.	107
Figure 60. Block Diagram of Microwave Power Measurement System using the Hewlett Packard HP8481A Thermocouple Sensor and HP438A Power Meter [Ref 20].	109
Figure 61. MAV Rectifier Efficiency Measurements for Two Parallel Si-SBD Microstrip Rectifier Circuit (Circuit M3-2) with External Double Short Circuit Stub Impedance Matching Tuner. (a) 1.0 GHz CW Input Signal with Miniature DC Motor as Load. (b) 1.0 GHz CW Input Signal with Miniature DC Motor as Load. (c) 1.0 GHz CW Input Signal with 10 ohm Lumped Element Resistor as Load.	114

Figure 62. MAV Rectifier Efficiency Measurements for two Parallel Si-SBD Microstrip Rectifier Circuit (Circuit m4-2) with External Impedance Matching Tuner. (a) 1.0 GHz CW Input Signal with Miniature DC Motor as Load. (b) 1.0 GHz CW Input Signal with Miniature DC Motor as Load (Second Data Set).	115
Figure 63. MAV Rectifier Efficiency Measurements (Circuit m7d-9) Single Si-SBD Microstrip Rectifier Circuit with Shunt Stub Impedance Matching.	116
Figure 64. MAV Rectifier Efficiency Measurements (Circuit m7d-8) Two Parallel Si-SBD Microstrip Rectifier Circuit with Shunt Stub Impedance Matching.	117
Figure 65. MAV Rectifier Efficiency Measurements – Expanded (Circuit m7d-8) Two Parallel Diode Rectifier Circuit with Shunt Stub Impedance Matching Expanded Scale showing Only Pulsed CW Input Signal Results.....	118
Figure 66. MAV-1 (1 GHz CW) Wireless Power Transfer Demonstration Aparatus.	126
Figure 67. Wireless Power Transfer Demonstration 1.0 GHz CW Transmission Signal to Power MAV-1.....	127
Figure 68. MAV-1 at the Face of the Transmitting Horn Aperature.	127
Figure 69. MAV-1 Model for 1.0 GHz WPT Demonstration. (a) MAV-1 Antenna and Rectifier Disassembled with Antenna Dimensions. (b) MAV-1 Microstrip Rectifier Circuit Dimensions.	128
Figure 70. Block Diagram of Wireless Power Transfer Demonstration Apparatus 1.3 GHz CW and Pulsed CW Transmit Signals.....	130
Figure 71. Wireless Power Transfer Demonstration 1.3 GHz CW and Pulsed CW Transmission to MAV-2.....	131
Figure 72. Wireless Power Transfer Demonstration 1.3 GHz CW Transmission Operating DC Motor to MAV-2.....	131
Figure 73. MAV-2 Model for 1.3 GHz WPT Demonstration. (a) MAV-2 Antenna and Rectifier Disassembled with Antenna Dimensions Indicated. (b) MAV- 2 Microstrip Rectifier Circuit Dimensions (Circuit 7d-5).....	132
Figure 74. Maximum Permissible Exposure to RF/Microwave Radiation [Ref 22]. (a) Controlled Environment Specifications. (b) Uncontrolled Environment Specifications.....	134

Figure 75. WPT Transmitter Power Levels for Far Field Operation of MAV. Transmit Antenna is 15 dB Pyramidal Horn, Required Power by MAV is 15 dBm.....	137
Figure 76. MAV-2 Required Transmitter Power verses Distance From Source Antenna and Available AN/SPS-58 Radar Transmitter Power. MAV_2_ave_watts is the MAV-2 Required Transmitter Power, P58A_ave is the available AN/SPS-58 Radar Transmitter Power.....	140
Figure 77. EEsoft Libra [®] Circuit File for Sample Microstrip (Circuit 3-1).....	147
Figure 78. Microstrip Width Calculations.....	149
Figure 79. EEsoft Libra [®] Circuit Model for FR-4 Microstrip Through Line.....	151
Figure 80. Calculations of SMT-SBD Package S parameters.	153
Figure 81. EEsof Libra [®] Model for HP HSMS-2825 Si-SBD.....	159
Figure 82. EEsoft Libra [®] Circuit File, Microstrip Rectifier Circuit (Circuit 4-2).	161

LIST OF TABLES

Table 1. Diode Characteristics for Hewlett Packard HSMS-2825, RF Silicon Schottky-barrier Diode.	22
Table 2. Microstrip Design Constants.	45
Table 3. Smith Chart Determined Lengths and Positions for Shunt Stub.....	45
Table 4. Design Variation Simulations for the Shunt Stub Impedance Matching Circuit.....	48
Table 5. GNEC [®] Model Parameter Guidelines.....	74
Table 6. Acceptable Ranges for GNEC [®] /NEC 4.1 MAV Geometry Definitions.	75
Table 7. GNEC [®] Model Wire Segment Definition.....	76
Table 8. GNEC [®] Calculated Reactance and Impedance for 10.2 cm MAV Antenna Operating at 1.0 GHz. (a) Reactance. (b) Impedance Magnitude.....	86
Table 9. GNEC [®] Calculated Reactance and Impedance for 10.2 cm MAV Antenna Operating at 1.3 GHz. (a) Reactance. (b) Impedance Magnitude.....	87
Table 10. Summary of Feed Gap Parameters for Optimized 10.2 cm MAV Antenna.....	88
Table 11. Summary of Rectifier Efficiency Measurements.....	112
Table 12. Far Field Operation Specifications for WPT of MAV Demonstrators.....	136
Table 13. MAV WPT Demonstration Summary.....	138
Table 14. AN/SPS-58 Air Search Radar Transmitter Specifications.....	139
Table 15. Conductive Coating Suppliers for Carbon Fiber MAV Body.	169

ACKNOWLEDGMENT

I would like to extend my sincere gratitude to my thesis advisor, Professor David Jenn, for the opportunity to learn new engineering skills and the chance to apply them on a truly unique project, a project that obtained high visibility if not much funding. Professor Jenn's guidance and especially his patience were appreciated as completion of this thesis was delayed several times due to workload levels in the Microwave Lab.

I also extend a special thanks to Professor Jeffery Knorr, who as my faculty supervisor, has been one of my chief mentors since I arrived at the Naval Postgraduate School. Professor Knorr and my direct supervisor, the ECE Lab Manager, Mr. Bob McDonnell have been very supportive of my efforts to achieve a Masters degree from this institution. Many supervisors would not be as supportive and I sincerely thank them both.

I also thank Eric Conner from the Physics department for his assistance in etching the microstrip boards and Dr. Jovan Lebaric for suggestions made towards the rectifier circuit design. A sincere thanks is extended to the engineering students in the classes that I have assisted. The drive and commitment displayed by these students inspired me to continue with this work. I learned as much from them as they did from me.

Lastly and foremost, I extend my sincerest gratitude to my wife, Dr. Theresa Repasky. Her love, support and understanding while I spent long hours working on this project and preceding coursework were especially appreciated.

I. INTRODUCTION

A. BACKGROUND

1. Wireless Power Transmission

Wireless Power Transmission (WPT) refers to the point to point transfer of electrical power in space without the use of transmission lines. All radio applications presently do this; however, they only transfer very small amounts of power. WPT seeks to transfer significant amounts of energy, which would be used to power remote systems. Such systems include remote sensors and even the propulsion of vehicles. This thesis investigates the possibility of using WPT to power a tiny remotely piloted micro air vehicle (MAV).

Wireless power transmission for remote powering of aerospace vehicles has its origin in research conducted by Brown in 1963 [Ref 1]. This research was an outgrowth of a Defense Advanced Research Projects Agency (DARPA) project to develop high power microwave tubes. At that time, Brown was able to develop microwave to DC conversion using closed spaced thermionic diodes in a flat array that provided 50% RF-to-DC conversion efficiency and produced over 900 watts of DC power [Ref 2]. The work culminated with a demonstration of a tethered wireless powered helicopter in 1964. Although this demonstration was impressive, the application of WPT to an airborne vehicle was ahead of its time. Technology in the mid 1960s did not allow sensors small enough to be carried by the helicopter and, in addition, the diode array antenna required for operation was many times larger than the helicopter itself. Although Brown's initial research was

funded by DARPA, much of the follow on research was funded internally by Raytheon Corporation or was conducted at his own expense.

Since the initial research, much of the subsequent work on wireless power transfer has concentrated on space based applications. These applications include the NASA solar power satellite, which has the objective of collecting solar energy in space for use on Earth. Energy collected in space would be transmitted to Earth ground stations via a high power microwave signal, then rectified and used in the power grid. Other WPT space projects included electrical power transmission from remote nuclear powered satellites (generators) to a space station, remote power sources for spacecraft propulsion systems (ion thrusters), and the powering or recharging of miniature satellites from Earth [Ref 3]. The last application has recently shown to have promising practical use. Providing Earth based electrical power to an orbiting space satellite would greatly reduce the size and, more importantly, the launch weight of a satellite, thereby vastly reducing the cost to build and launch the satellite.

Recently, three separate university research groups have been working on the application of WPT to power remotely operated air vehicles. The Kobe University (Japan) has successfully demonstrated WPT to an airship using large flat panel arrays (Project ETHER) [Ref 4]. The University of Alaska at Fairbanks is in the process of developing a model helicopter powered via WPT (Project SABER) [Ref 5]. Project SABER re-uses a diode array originally built by Brown. Finally, the Naval Postgraduate School has participated in the development of a remotely powered micro air vehicle (MAV) in

cooperation with the Lutronix Corporation [Ref 6]. WPT techniques to support remote powering or remote recharging of a miniature rotorcraft are the subject of this thesis.

2. MAV

The micro air vehicle (MAV) is intended to be a miniature (maximum size of several inches) airborne remotely piloted rotorcraft. MAV missions generally fall into two categories. The first is indoors, where the ranges may be short but mission duration long (perhaps days). The second is outdoors, where the operational ranges are longer and the aerodynamic environment more severe. Typical outdoor MAV missions include the ability to fly out to ranges of several kilometers, conduct surveillance or possibly detonate a charge to destroy a target in a suicide mission.

One important indoor application is the video surveillance of building interiors, where people are not allowed or physically cannot go. Examples include buildings that are controlled by unfriendly personnel (such as terrorists), areas or situations that are environmentally dangerous (such as inside a nuclear reactor) or perhaps where it is more economical to use robotic surveillance. Because of its small size and quietness due to electrical propulsion (i.e. covertness), the MAV is thought to have greater success flying against interior building targets rather than flying outside, where wind forces tend to favor the aerodynamics of a larger air vehicle.

A micro air vehicle under development by Lutronics Corporation is shown in Figure 1. This MAV is presently electrically powered via a tether cable. However, to become practical for most applications, it will need to carry an energy source or receive electrical power via WPT. MAV operations using WPT could eliminate a large percentage

of the vehicle's weight, namely the fuel and its tank or the battery. Weight and space savings would permit the MAV to operate on extended missions and be better equipped since additional space and weight are available for sensors, flight control systems and weapons. Even if WPT only supplied battery recharge power, the battery could be made smaller and lighter without adversely affecting mission endurance because the vehicle could be recharged intermittently in-flight.

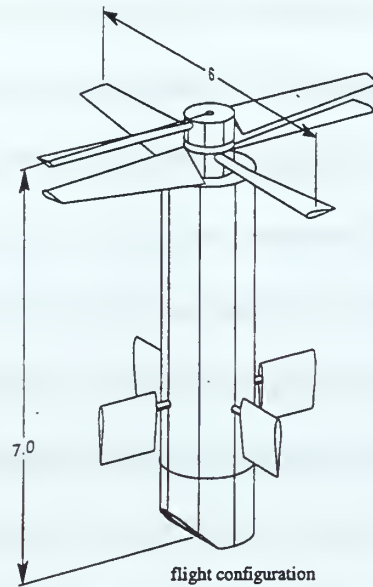


Figure 1. Proposed Remotely Piloted Micro Air Vehicle (MAV)

B. PREVIOUS RESEARCH

The tradeoffs involved in the design of a remotely piloted vehicle have been discussed in several publications [Ref 7, 8]. One possible approach is to use several ground stations that are synchronized to provide a coherent “spot” at the MAV as illustrated in Figure 2. This multiple ground station approach allows a deployment that is more flexible and is more robust in the presence of propagation obstructions than a single ground station.

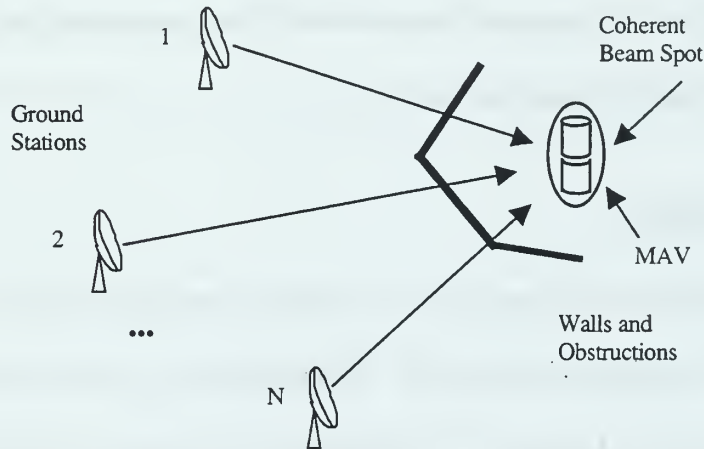


Figure 2. Proposed Deployment of Wireless Powered MAV

Previously, Gibson [Ref 9] conducted investigations with regard to propagation losses due to building walls and evaluated several antenna approaches. Propagation measurements and computer simulations were conducted for frequencies from 2 to 6 GHz. In particular, the signal attenuation through building walls was modeled and verified by measurement. Data showed a trend of improved microwave signal propagation through buildings as the frequency decreased.

The selection of frequency is a critical issue. Although lower frequencies have a better capability to penetrate buildings, the antenna size for the required gain becomes prohibitively large. Therefore, it appears that 1 GHz is about the limit at the lower end.

A transmission frequency of 2.45 GHz was suggested by Gibson; however, it will be shown in Chapter III that a dipole antenna the size of the MAV would have a very large radiation resistance and makes impedance matching of the rectifier circuit to antenna difficult. The frequency chosen for this research was 1 GHz, which for the MAV body size provides a radiation resistance value close to the characteristic impedance of the interfacing transmission line. Subsequent research increased the WPT frequency to 1.3 GHz in order to use the high transmit power of the AN/SPS-65 air search radar located in the Naval Postgraduate School's Radar Laboratory.

C. OBJECTIVE

The objective of this research is to develop a prototype of a MAV that is powered by WPT from an off-board energy source. The dimensions of the model are the same as the flying model built by Lutronix. There were two major tasks. The first was to design an antenna with the proper coverage and input impedance, with little or no weight penalty. The second task was to design an efficient rectifying circuit that would provide sufficient current to a DC motor.

This thesis consists of six chapters. Chapter II discusses the design and fabrication of the microstrip rectifier circuit, including the computer simulations conducted using EEsof Libra[®]. Verification of the circuit design is accomplished using measurements from the Hewlett Packard HP 8510C Vector Network Analyzer System. Chapter III covers the development of the mockup MAV body that serves as the receiving antenna for WPT. Chapter III includes computer modeling of the antenna using the method of moments, Numerical Electromagnetics Code (NEC 4.1), verification measurements on the vector

network analyzer system, and also describes how the various MAV antenna designs were fabricated. Chapter IV presents the efficiency testing that was conducted on several microstrip rectifier designs and explains the techniques used to measure RF-to-DC conversion efficiency. Efficiencies were measured for continuous wave (CW) signals and for a simulated radar waveform (pulse modulated CW). Chapter V presents test results of the entire MAV WPT system using CW and pulse modulated CW signals that simulated the Naval Postgraduate School's AN/SPS-65 air search radar. Finally, Chapter VI presents conclusions of the effort along with some suggestions for possible future research.

II. RECTIFIER CIRCUIT DESIGN

The wireless power transfer system on the MAV consists of two basic parts: the receiving antenna and the microwave rectification circuitry. Independent development of the rectifier and antenna was possible by impedance matching each of these elements to a short piece of 50 ohm RG-141 semi-rigid coaxial cable. This short (1.2 inches) semi-rigid cable served as the feed from the antenna to the rectifier circuit and also provided a rigid mount for the circuit and motor inside of the top half of the MAV. An illustration of the assembled MAV is shown in Figure 3, where the microwave rectifier circuit is located inside the top half of the MAV dipole antenna. This chapter discusses the design, development and verification testing of the microwave rectification circuit and the unique aspects of its design for efficient operation at microwave frequencies.

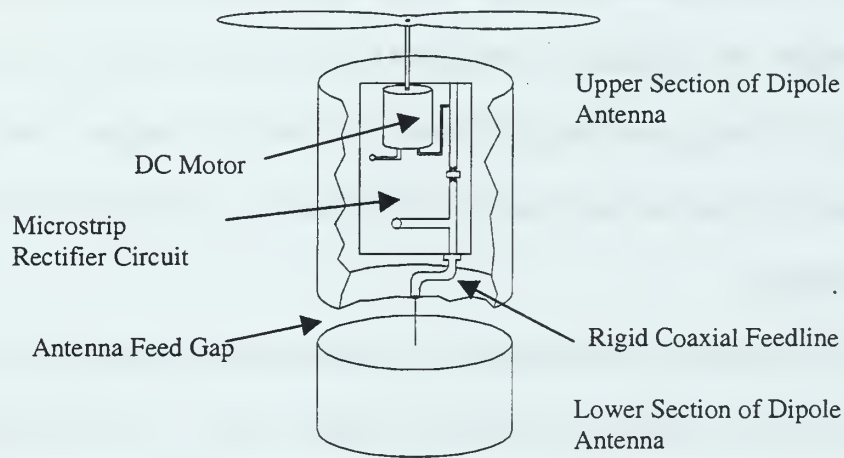


Figure 3. Assembled MAV, Cutaway to View Components Inside.

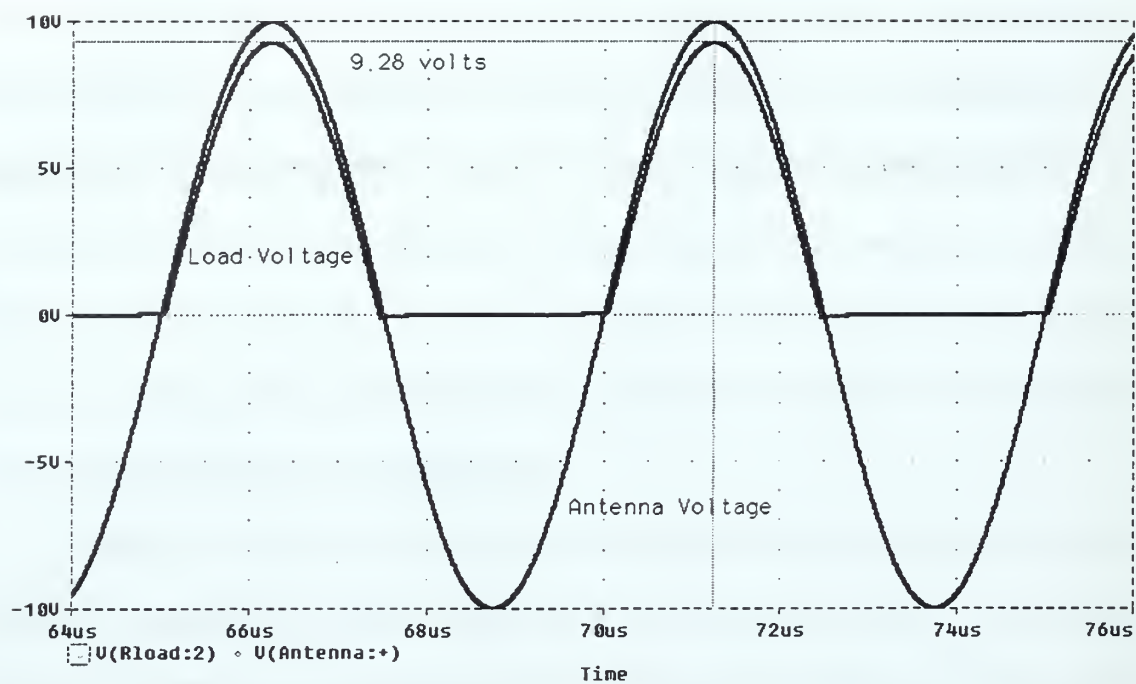
A. RECTIFIER CIRCUIT TOPOLOGY

The MAV body serves as the antenna, receiving a zero average voltage sinusoidal signal, continuous wave, at microwave frequencies. The received microwave radiation is converted using a microstrip rectifier circuit to a signal with an average DC voltage. This DC voltage is used to drive a miniature DC motor, which spins the helicopter rotor blade. The goal of the rectifier circuit is to provide the largest average DC power for a given input microwave signal power. This section discusses the types of rectifier circuits investigated and how a circuit selection was accomplished.

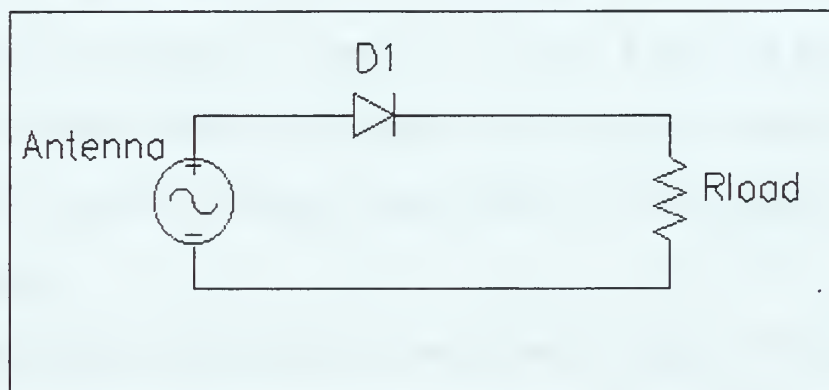
Rectification of microwave power has unique design challenges relative to the more commonly encountered problem of rectification of 60 Hz power signal. The unique challenges include: (1) requirements for quick switching, (0.1 ns), to keep up with the signal frequency; (2) compensation for parasitic reactance, resistance and circuit topologies (such as lead lengths and transmission structures) that are not a factor for lower frequency operation; (3) effective blocking of the reverse current on the negative half cycle; and (4) high frequency impedance matching to avoid reflection of the received CW power at the antenna terminals.

Three rectifier circuit topologies are typically used for passive diode rectifiers. They are: (1) half-wave rectifier, (2) full-wave rectifier, and (3) full-wave bridge rectifier. Figure 4, Figure 5 and Figure 6 illustrate these three circuits and their computer simulated rectified output voltages using for a sinusoidal input signal. Computer simulations were conducted using Pspice. Upon inspection of the simulated output voltage, it is noted that none of these circuits provides a true DC voltage. Rather, the rectifier circuits convert a zero average sinusoidal voltage signal to a non-zero average voltage time varying signal.

A rectifier's efficiency, or ability to provide a larger average output voltage, can be increased by placing an appropriately sized capacitor across the rectifier output in parallel with the load. This is illustrated for a half-wave rectifier in Figure 7. This "filter" capacitor serves to reduce voltage variations in between positive voltage swings at the rectifier output.

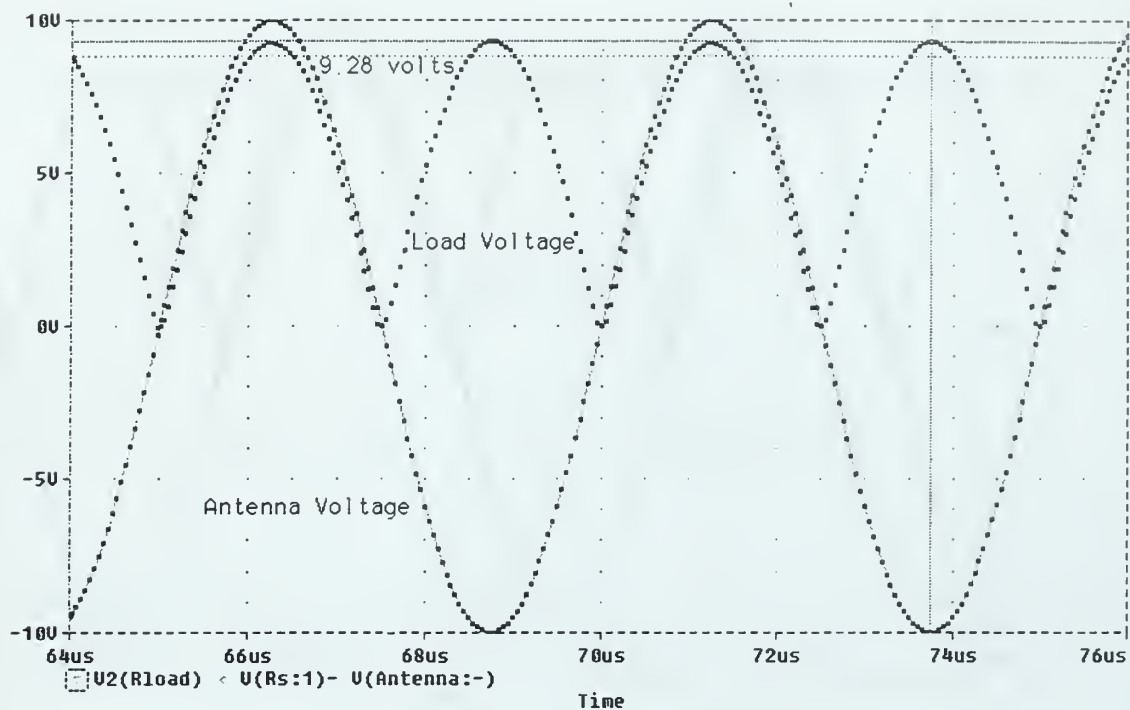


(a)

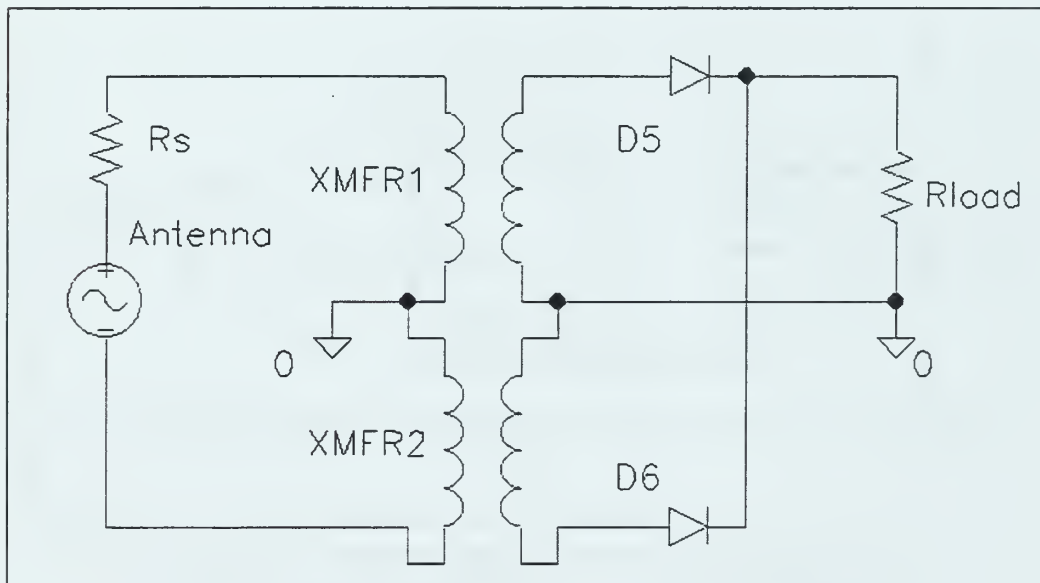


(b)

Figure 4. Half-Wave Rectifier.
(a) Input Signal and Rectified Output. (b) Schematic Diagram.

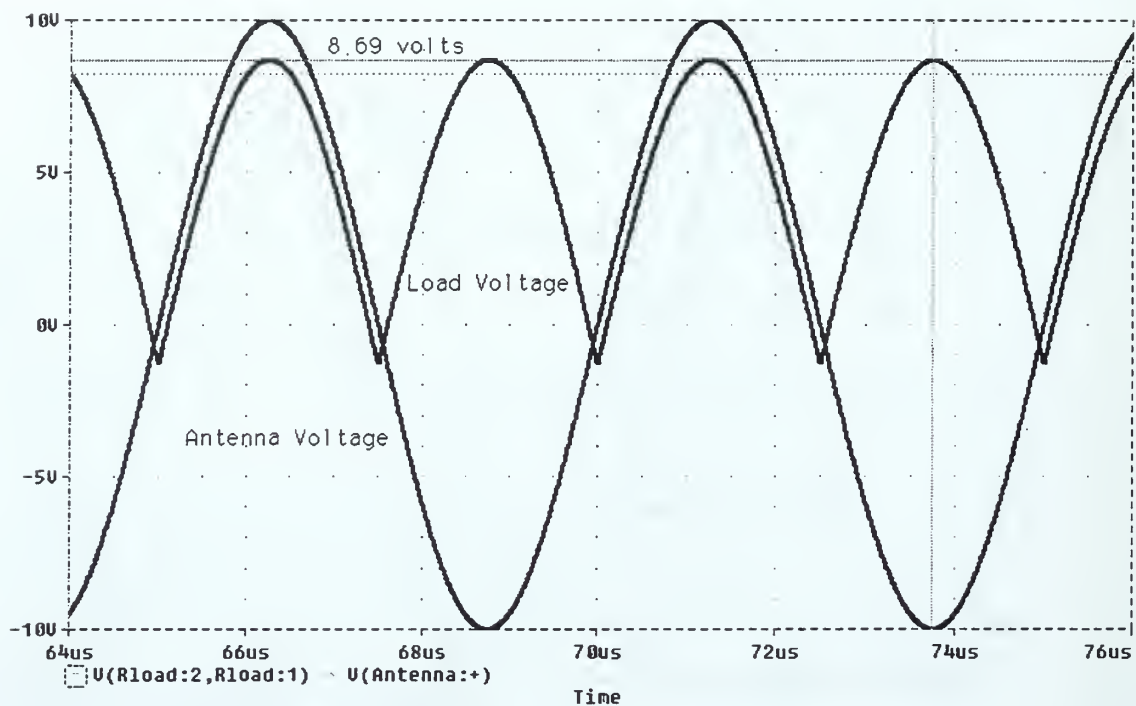


(a)

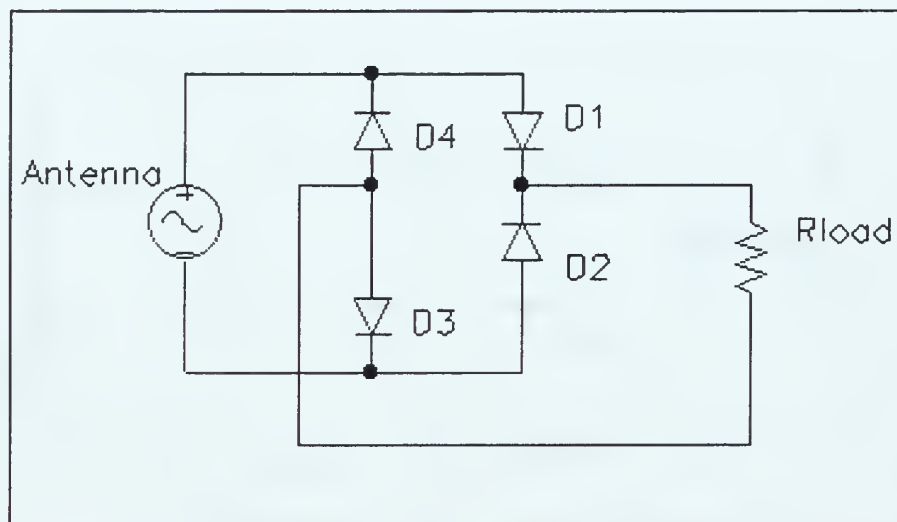


(b)

Figure 5. Full-Wave Rectifier Diode Circuit.
(a) Input Signal and Rectified Output. (b) Schematic Diagram.

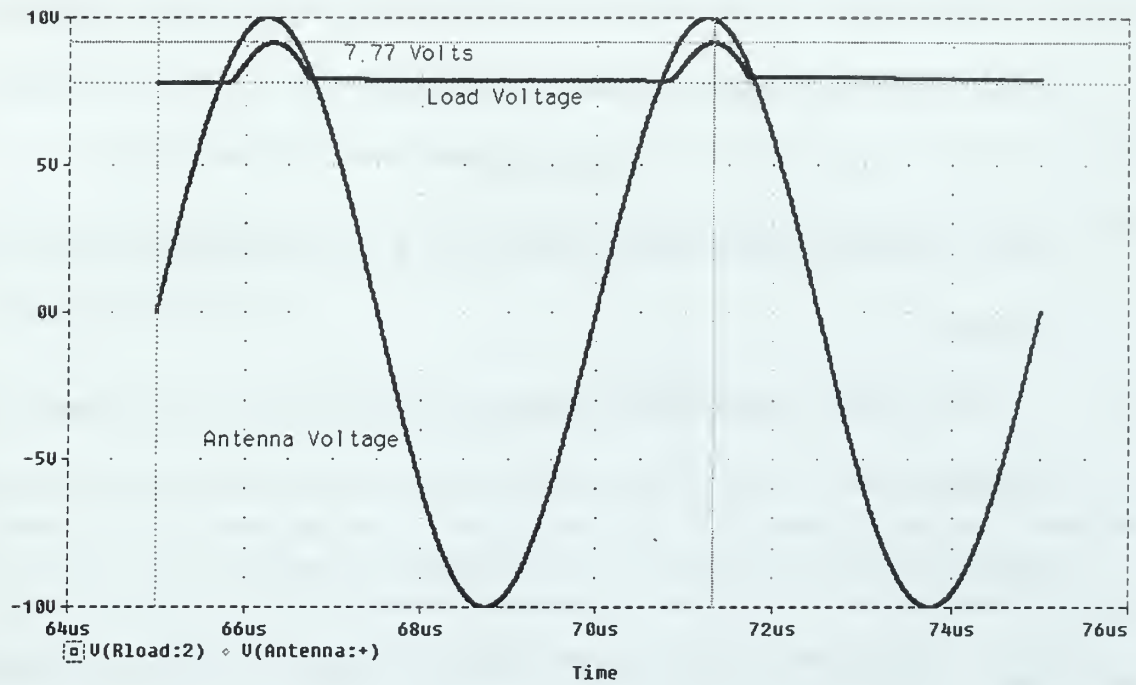


(a)

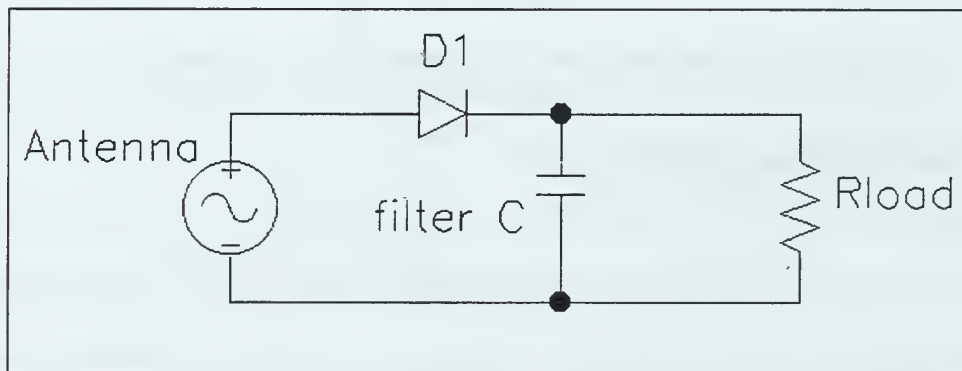


(b)

Figure 6. Full-Wave Bridge Rectifier Circuit.
(a) Input Signal and Rectified Output. (b) Schematic Diagram.



(a)



(b)

Figure 7. Half-Wave Rectifier with Filter Capacitor.
(a) Input Signal and Rectified Output. (b) Schematic Diagram.

The output voltage when the diode is not conducting is compensated for by the discharge of the filter capacitor. It can be expressed as

$$v_o(t) = V_p e^{-t/RC}, \quad (1)$$

where V_p is the peak voltage of the rectified signal, R is the load resistance and C the filter capacitance.

The output voltage deviation (ripple) from the peak voltage can be derived by taking the discharge time (t) to be a full period (T) of the input sinusoid and equating this voltage ripple to the difference between peak (V_p) and minimum ripple voltage (V_r) [Ref 10]. For $RC \gg T$, the exponential can be approximated by the series $\left(1 - \frac{T}{RC}\right)$ and the minimum output voltage can be expressed as

$$V_{0\min} = V_p \left(1 - \frac{T}{RC}\right). \quad (2)$$

The output DC voltage is approximated by the average voltage between the peak (V_p) and voltage minimum ($V_{0\min}$)

$$V_{0(HWR)} = V_p \left(1 - \frac{1}{2f RC}\right). \quad (3)$$

Equation (3) was developed for the half-wave rectifier. The same method can be applied to the full-wave rectifier using $T/2$ for the discharge time. The resulting expression for the output voltage becomes

$$V_{0(FWR)} = V_p \left(1 - \frac{1}{4f RC}\right). \quad (4)$$

Equations (3) and (4) show that the larger average voltage of the full-wave rectifier can be approached by the half-wave rectifier with the filter capacitor doubled.

The filter capacitor does, however, increase the forward diode conduction current. This current, in addition to the normal load current, is required to recharge the filter capacitor and is given by

$$I_{D \text{ forward}} = I_L \left(1 + \pi \sqrt{\frac{2RC}{T}} \right) \quad (5)$$

where I_L is the load current and the second term of equation (5) is due to the filter capacitance [Ref 10]. The increased conduction current occurs when the diode is forward biased and provides the upper limit of the filter capacitance. Generally it is desired that $RC \gg T$ to increase output voltage. However if RC is made too large, the conduction current will exceed the current rating of the diode. For example, if $RC = 10T$, the forward conduction current through the diode becomes 15 times the normal load current (I_L).

The half-wave rectifier has several advantages over the full-wave rectifier and full-wave bridge circuits for microwave signal rectification. The greatest advantage is the simplicity of circuit layout and ease of fabrication as a microstrip structure. All components reside on one side of the microstrip media with a minimum number of via holes (conductive paths from the top microstrip plane to the lower ground plane). This is important since via hole positioning and via hole reactance introduce errors into the impedance matching process. Also, the half-wave rectifier has a forward voltage drop across only one diode (V_d) whereas for the full-wave bridge rectifier, the forward voltage drop occurs across two

diodes in series and is, therefore, doubled ($2V_d$). For these reasons the half-wave rectifier circuit of Figure 4 was chosen for the microwave rectification circuit.

B. MICROWAVE DIODE SELECTION

Microwave signal rectification has unique performance requirements that are largely dependent upon the characteristics of the diodes being used. Chief among these are the switching speed and amounts of charge the diode stores in the junction. Therefore, it is primarily the microwave diode input-output characteristic that determines the behavior of the rectifier circuit and is crucial in obtaining efficient rectification.

Early research by George [Ref 11] showed microwave rectifier diode efficiency to be largely dependent upon the following characteristics:

- (1) recovery time of the diode (T_r),
- (2) forward resistance of the diode (R_f),
- (3) reverse resistance characteristic of the barrier layer, and
- (4) barrier capacitance and how it varies with DC back voltage.

George determined experimentally that the diode recovery time for microwave rectification should be less than a quarter-cycle of the frequency to be rectified ($T_r < T/4$). Also, the forward resistance and barrier capacitance should be minimized and the reverse resistance or, equivalently, peak inverse voltage (PIV) maximized.

The principal diodes used in rectifier design are the p-n junction diode (PN), point contact diode (PCD) and the Schottky-barrier diode (SBD). The operating characteristics of each type were investigated to determine the best selection.

1. PN Junction Diode

The PN diode is commonly used for low frequency detection and rectification. A diagram of the PN diode is shown in Figure 8. The forward biased p-n junction will typically have two types of forward bias capacitance: depletion layer capacitance (C_j) and diffusion capacitance (C_d). C_d is due to majority charge carriers crossing the p-n junction and becoming minority carriers in the other semiconductor material. These minority carriers do not recombine immediately and if the bias reverses before recombination occurs, then these carriers return across the junction as a current pulse. This effect is called the junction storage capacitance and is a problem for operation at high frequencies since the signal is not effectively rectified due to the reverse current from the junction storage capacitance. Therefore the PN diode does not operate well as a rectifier at microwave frequencies.

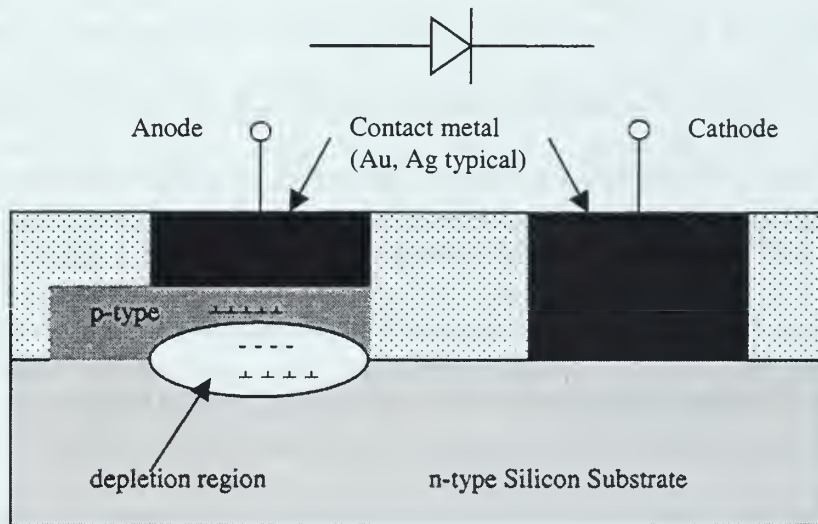


Figure 8. Illustration of PN Junction Diode.

2. Metal Semiconductor (MS) Diodes

The point contact diode (PCD) and Schottky-barrier diode (SBD) are metal-semiconductor (MS) diodes. This terminology refers to a type of device physics where the rectifying junction is metal to semiconductor rather than semiconductor to semiconductor (such as the PN diode). The difference between the PCD and SBD is in their construction. In the case of the SBD, Schottky-barrier metal is deposited onto the semiconductor as part of the chip fabrication process, whereas in the PCD, the barrier metal is at the pointed end of a whisker, which is mechanically wedged against the semiconductor chip during final assembly. The prudent choice for the MAV rectifier is the SBD. Mechanical vibrations and shock are likely to be typical in this operating environment and the mechanical PCD whisker contact may not be reliable for this application.

Since the PCD and SBD are MS diodes, they operate on similar electronic principals. Therefore discussing the electronic operation of the SBD applies as well to the PCD and helps to demonstrate an inherent advantage of a SBD microwave rectifier circuit. The SBD consists of a metal semiconductor junction where the Schottky-barrier metal is different than the metal used to make the contacts and forms the anode of the diode. A diagram of a Hewlett Packard passivated hybrid SBD is shown in Figure 9.

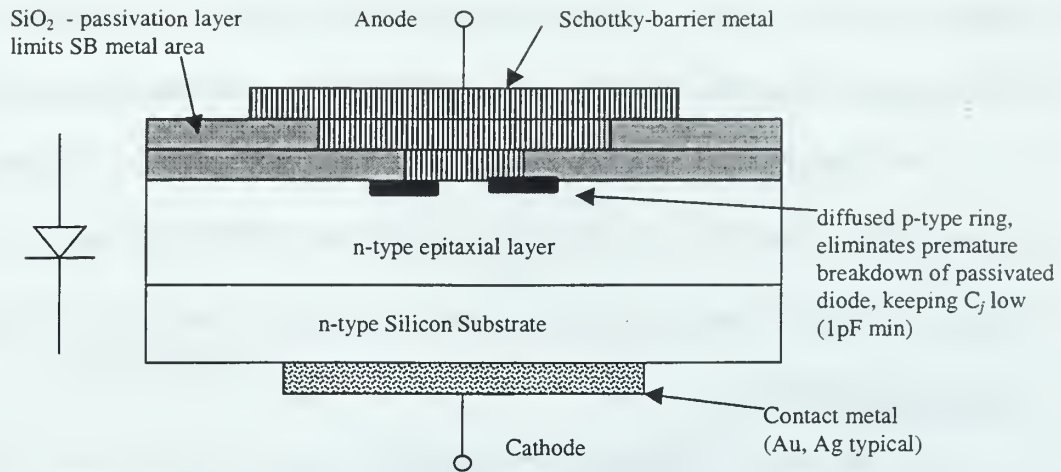


Figure 9. Silicon Schottky-Barrier Diode (Si-SBD)
Hewlett Packard Passivated Hybrid Type.

A metal-semiconductor diode involves majority carriers only; minority carriers are non-existent due to the lack of oppositely doped semiconductor. Forward conduction current consists of the majority carriers flowing into the Schottky-barrier metal (anode) from the semiconductor (cathode). Unlike the p-n type semiconductor junction, the Schottky-barrier does not have minority charge storage and the resultant diffusion capacitance (C_d). This makes the SBD well suited for high frequency operation because the SBD has only one capacitive effect: depletion-layer capacitance (C_j) [Ref 10].

The SBD selected for use in the MAV rectifier circuit is the Hewlett Packard HSMS-2825, which has a single housing that contains a pair of SBDs with silicon substrate and is packaged as a surface mount technology (SMT) device. The HSMS-2825 SMT-SBD pair are arranged unconnected, in parallel and in the same direction. This arrangement simplified assembly onto the microstrip structure and provided the option of using multiple diodes in parallel to increase the current carrying capability of the rectifier. The SMT package provided a compact design that minimizes lead length, which is helpful for

impedance matching. SMT devices are difficult to hand solder, requiring a microscope, tweezers and a steady hand, but their size advantage make up for their assembly difficulties.

Individual SBDs in this package have the characteristics shown in Table 1. If the recovery time is defined as the RC time constant, the HSMS-2825 has a T_r of 10ps. George's T_r specification for a 1.3 GHz microwave signal is 190 ps, which is compatible with the HSMS-2825 SBD.

Name	Characteristic	Value
V_{BR}	PIV- peak inverse voltage (minimum diode breakdown voltage)	8 V
V_F	maximum forward voltage	340 mV
I_R	reverse leakage current	100 mA
C_T	maximum capacitance	1.0 pF
R_D	typical dynamic resistance	10 ohms

Table 1. Diode Characteristics for Hewlett Packard HSMS-2825, RF Silicon Schottky-barrier Diode.

Although the SBD chosen has a silicon substrate, SBDs are often fabricated with gallium arsenide (GaAs) as the substrate material. A diagram of a GaAs SBD is shown in Figure 10.

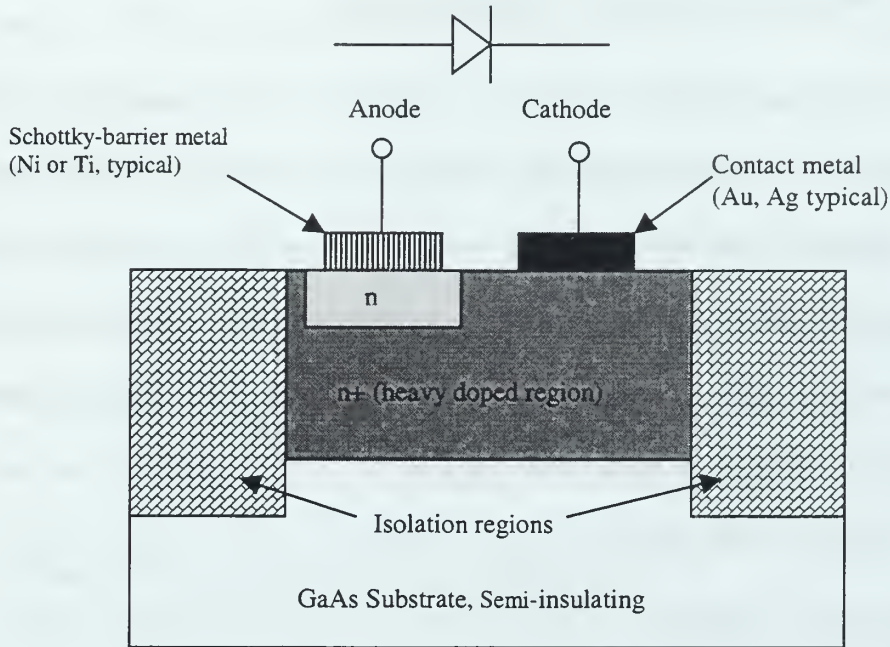


Figure 10. Illustration of GaAs Schottky-barrier Diode.

The major advantage of GaAs is that electron velocity is greater in n-type GaAs than in silicon. Therefore larger output currents are obtained for the same input voltages, which enables faster charging and discharging of circuit and parasitic capacitances. Undoped GaAs has very low conductivity acting as a semi-insulator, thereby providing good isolation from other devices on the same substrate. This property results in smaller parasitic capacitance between the devices and circuit ground. A heavily doped n-type GaAs (n+ region) is used between the semiconductor (n region) and the cathode metal contact to lower parasitic series resistance. All of these characteristics increase the operating speed of a GaAs SBD over a Silicon SBD enabling rectification for higher frequencies as per George's [Ref 11] research. Although this higher speed is essential for rectifiers operating at

millimeter wavelengths [Ref 12], it is not critical for the frequencies used in this research (1.0, 1.3 GHz). Therefore the speed of GaAs was not considered necessary.

C. PC BOARD CHARACTERIZATION

Microstrip transmission line was chosen to be the transmission medium for the rectifier circuit because design and fabrication were more efficient as opposed to other types of transmission structures such as stripline. Microstrip structures can be fabricated using printed circuit board etching methods, whereas other appropriate guiding structures (such as stripline) require precision machining of dielectric materials and fixtures and would have incurred greater costs to fabricate.

Design of the microstrip circuit pattern required accurate knowledge of the relative permittivity (ϵ_r) of the FR-4 dielectric substrate. Since this particular PCB is typically used for low frequency applications, accurate information for ϵ_r was not available and its value was experimentally determined. Experiments consisted of fabricating an unbroken through transmission line on a sample PCB (Circuit 3-1), measuring its scattering parameters on a vector network analyzer, and then using computer simulations to adjust ϵ_r so that the measured and simulated scattering parameters matched. A 50 ohm through microstrip line (Circuit 4-1) was then designed, fabricated and tested to verify the validity of the ϵ_r determined previously.

1. Microstrip Fabrication

The printed circuit board (PCB) material was purchased pre-coated with photo-resist. This PCB material was 1/16 inch thick fiberglass epoxy with 1 ounce copper plating

on both sides, commonly referred to as FR-4 PCB. Fabrication of the rectifier microstrip traces was done by photodeveloping and ferric chloride etching. This process exposes the PCB to high intensity ultraviolet (UV) light filtered through a pattern of the microstrip (circuit mask). The UV light burns off photo-resist in the areas where the copper is to be removed. A developer solution is applied to the board, which adheres to the photo-resist, coating desired areas of copper (traces). The board is emerged into a bath of ferric chloride to dissolve copper plating from regions unprotected by the developer coating. The ferric chloride bath is heated and agitated to increase effectiveness and shorten etching time. The etched board is removed from the bath, rinsed with water and the developer removed from the copper traces by hand using a non-metallic abrasive pad.

2. Permittivity Determination Circuit (Circuit 3-1)

A microstrip through line circuit of width 160 mils (0.001 inch) and length 4775 mils was fabricated using FR-4 PCB material. This microstrip circuit was labeled Circuit 3-1. A Hewlett Packard HP8510C Microwave Vector Network Analyzer System (VNA) was used to measure input impedance (Z_{in}), return loss (S_{11}) and insertion loss (S_{21}) of the through microstrip line (Circuit 3-1). A copy of the return loss as measured by the VNA is shown in Figure 11.

A computer model of this microstrip transmission line was developed using EEsof Libra[®] high frequency circuit simulation software. This model is attached as Appendix A. The computer model had the same geometry and dimensions as the fabricated microstrip line, complete with the SMA connectors on both ends. Simulations using the Libra[®] model were conducted and the relative permittivity (ϵ_r) of the substrate adjusted until the return

loss (S_{11}) of the simulations agreed with the VNA measurements of S_{11} . Libra[®] calculated and VNA measurements of S_{11} were considered to agree when the number and frequency separation between S_{11} minimums (or nulls) matched and the overall return loss magnitudes were nearly the same. A frequency offset between the Libra[®] calculated and measured return loss plots was expected. This offset is due to uncertainties in the location of the VNA calibration plane reference which resulted from using the VNA calibration set (open, short, load) without entering the calibration set characterization data into the VNA computer memory.

An early evaluation of the Libra[®] model computation verses the VNA measurements determined a value for ϵ_r of 4.8 for the FR-4 PC board substrate. This value ($\epsilon_r = 4.8$) was then used in later designs of the microstrip rectifier.

Further review after the rectifier circuits were fabricated and tested uncovered an error in the determination of the value used for relativity permittivity ($\epsilon_r = 4.8$). Libra[®] calculations of return loss for Circuit 3-1 using values of 2.0, 3.0, 3.5, 4.0 and 5.0 for ϵ_r were redone and plotted alongside the VNA measurements. These plots are shown in Figures 12 to 16. Comparisons of these figures show that the agreement occurs for when the Libra[®] calculation uses an ϵ_r of 3.5, which is shown in Figure 14. Although this error does affect the subsequent rectifier circuit design, the initial circuit performance was acceptable so that a circuit redesign and fabrication was not required. The use of a high quality microwave substrate would eliminate the potential for this error, since the material characteristics would be known and controlled.

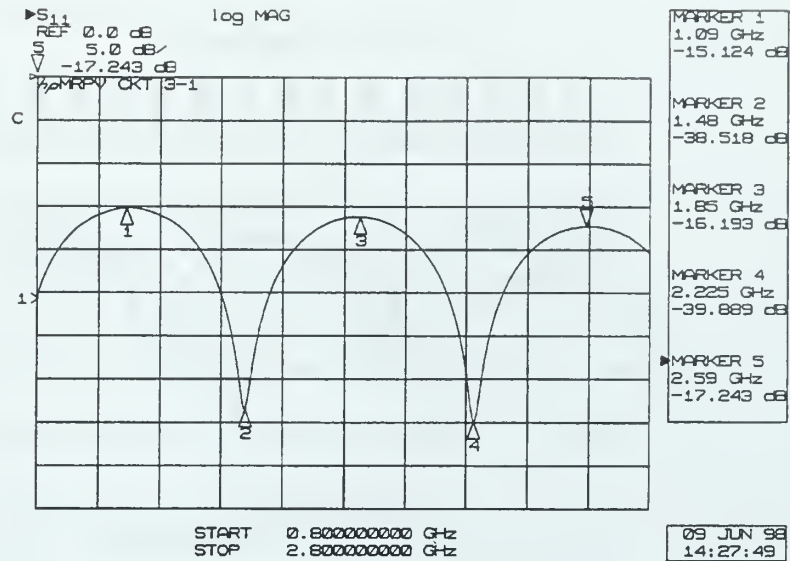


Figure 11. VNA Measured Return Loss for 50 ohm Microstrip Through Line (Circuit 3-1).

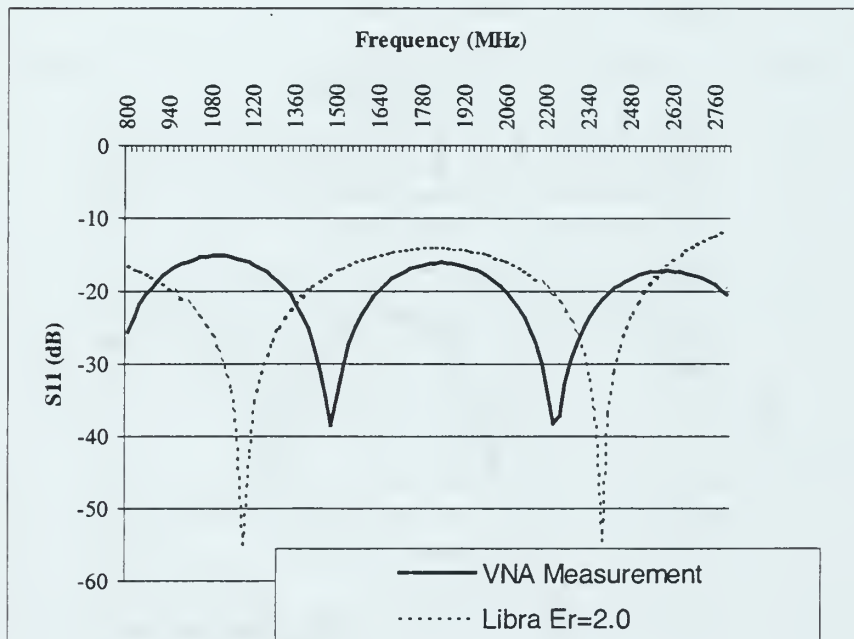


Figure 12. Circuit 3-1 Return Loss Comparison of VNA Measurements to Libra® Calculations using $\epsilon_r = 2.0$.

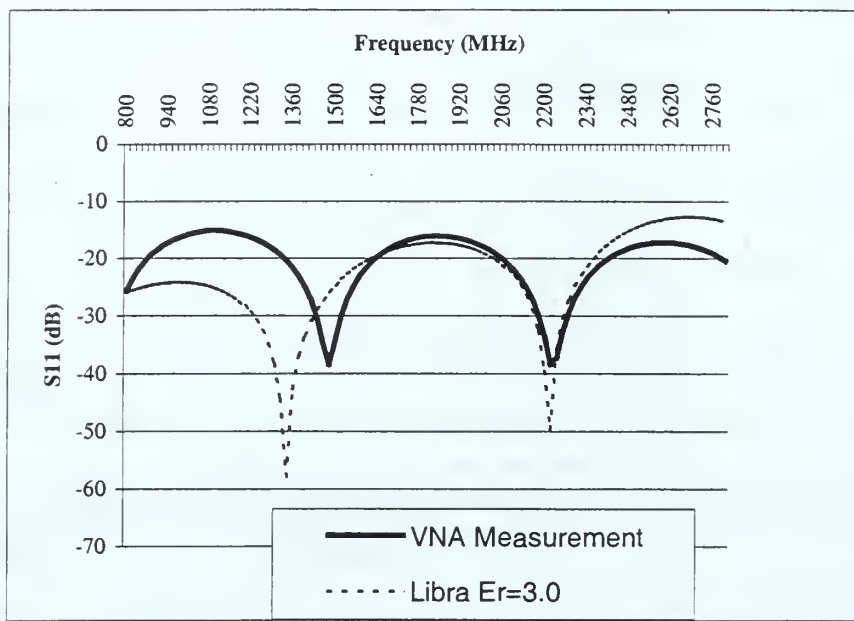


Figure 13. Circuit 3-1 Return Loss Comparison of VNA Measurements to Libra® Calculations using $\epsilon_r = 3.0$.

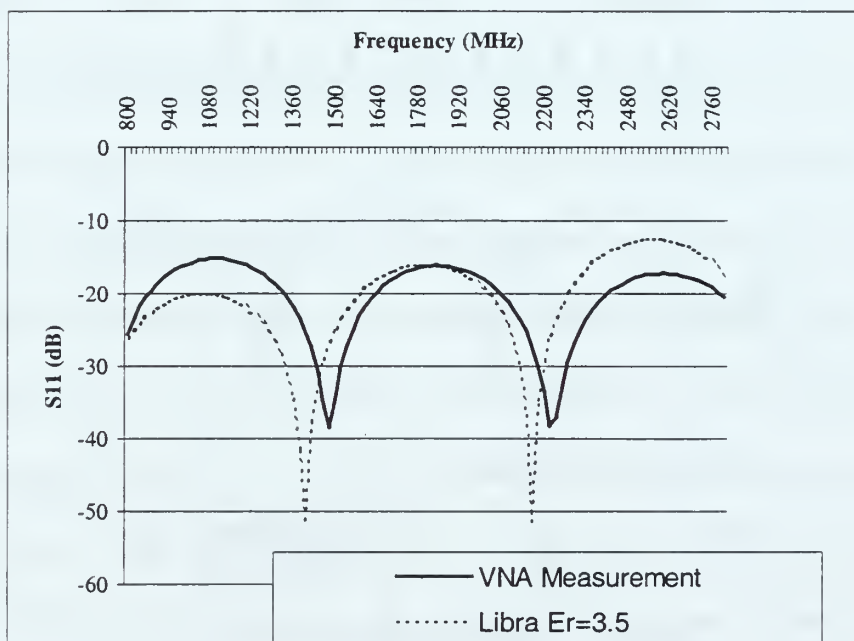


Figure 14. Circuit 3-1 Return Loss Comparison of VNA Measurements to Libra® Calculations using $\epsilon_r = 3.5$.

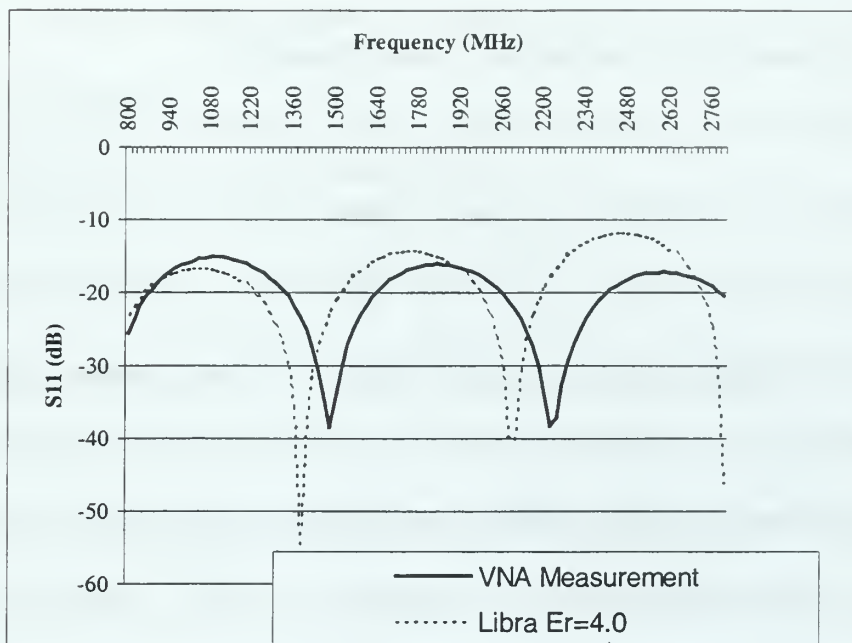


Figure 15. Circuit 3-1 Return Loss Comparison of VNA Measurements to Libra® Calculations using $\epsilon_r = 4.0$.

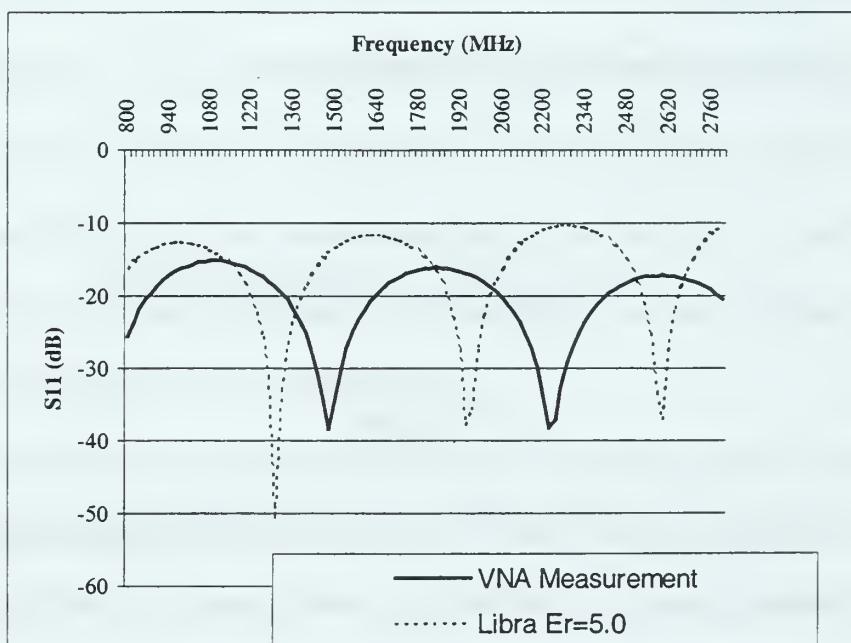


Figure 16. Circuit 3-1 Return Loss Comparison of VNA Measurements to Libra® Calculations using $\epsilon_r = 5.0$.

3. Permittivity Verification Circuit (Circuit 4-1)

The FR-4 PCB material substrate relative permittivity (ϵ_r) determined from the early Circuit 3-1 experiments was used to design a FR-4 microstrip transmission line with characteristic impedance (Z_0) of 50 ohms. This circuit was labeled Circuit 4-1 and served to test the estimated value of the permittivity of the FR-4 substrate material. The design parameters for a microstrip transmission line are: (1) microstrip line width (w), (2) dielectric substrate thickness (d), and (3) relative permittivity or relative dielectric constant (ϵ_r) of the substrate. These parameters can be adjusted to achieve a desired transmission line impedance (Z_0) using the following formulas [Ref 13]:

$$\frac{w}{d} = \frac{8e^A}{e^{2A} - 2} \quad \text{for } \frac{w}{d} < 2 \quad (6)$$

$$\frac{w}{d} = \frac{2}{\pi} \left[B - 1 - \ln(2B - 1) + \frac{\epsilon_r - 1}{2\epsilon_r} \left(\ln(B - 1) + 0.39 - \frac{0.61}{\epsilon_r} \right) \right] \quad \text{for } \frac{w}{d} > 2 \quad (7)$$

where

$$A = \frac{Z_0}{60} \sqrt{\frac{\epsilon_r + 1}{2}} + \frac{\epsilon_r - 1}{\epsilon_r + 1} \left(0.23 + \frac{0.11}{\epsilon_r} \right), \quad (8)$$

$$B = \frac{377\pi}{2Z_0\sqrt{\epsilon_r}} \quad (9)$$

A 50 ohm microstrip through line was designed and fabricated to verify the value of ϵ_r and the design equations. This structure, labeled Circuit 4-1, used FR-4 PCB material with a thickness of 62.5 mils (1 mil = 1/1000 inch) and was designed using (6) for an

assumed ϵ_r of 4.8. Calculations yielded a microstrip width of 111 mils. These calculations are attached as Appendix B.

A check on these calculations used [Ref 13]

$$Z_0 = \frac{60}{\epsilon_e} \ln \left(\frac{8d}{w} + \frac{w}{4d} \right) \quad (10)$$

where ϵ_e is the effective permittivity of the microstrip structure, given by

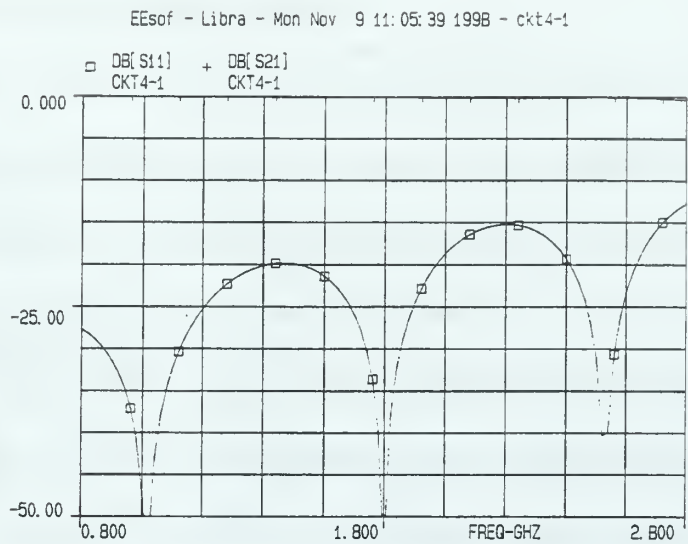
$$\epsilon_e = \epsilon_{effective} = \frac{\epsilon_r + 1}{2} + \frac{\epsilon_r - 1}{2} \left(\frac{1}{\sqrt{1 + i2 \frac{d}{w}}} \right). \quad (11)$$

The impedance calculated using (10) and (11) was 50.4 ohms which is 0.8% error from the design impedance of 50 ohms.

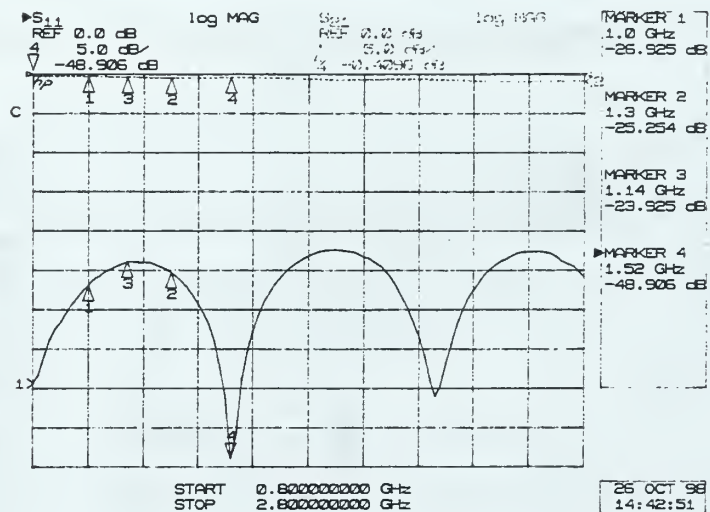
Return loss (S_{11}) and input impedance for Circuit 4-1 was measured using the HP8510 VNA. Circuit 4-1 was also modeled and simulated using EEsof Libra[®]. This model is attached as Appendix C. Comparison of return loss (S_{11}) between the Libra[®] computer simulations and VNA measurements are shown in Figure 17a and Figure 17b. Smith Chart plots of input impedance for Circuit 4-1 are shown by Figure 18a (Libra[®] Simulation) and Figure 18b (VNA Measurement).

The envelope of the simulated and measured return losses generally agree over the frequency band investigated (0.8 to 2.5 GHz). However, the locations of the minima and maxima were shifted in frequency. The disagreement of return loss maxima and minima with respect to frequency can be attributed to measurement inaccuracies of line length and the load plane location error during VNA calibrations. This load plane error is the result of

using coaxial short, open, and wideband load (50 ohms) calibration as opposed to a through, reflect line calibration. The plot of input impedance for Circuit 4-1, as shown on the Smith Charts of Figure 18a and Figure 18b, indicates that microstrip through line of width 111 mils has an impedance very close to 50 ohms. The difference for Circuit 4-1 is likely due to manufacturing tolerances for a microstrip circuit where the permittivity of the substrate material (fiberglass epoxy) is not tightly controlled and may vary considerably between different boards.



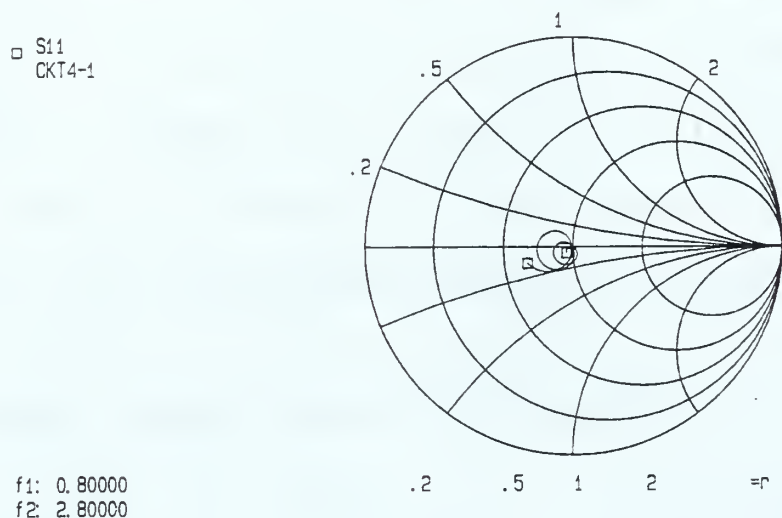
(a)



(b)

Figure 17. Return Loss (S_{11}) 50 ohm Microstrip through Line.
(Circuit 4-1: 111 mil wide line on FR-4 PC Board).

(a) Libra[®] Computer Simulation. (b) VNA Measurement.



(a)

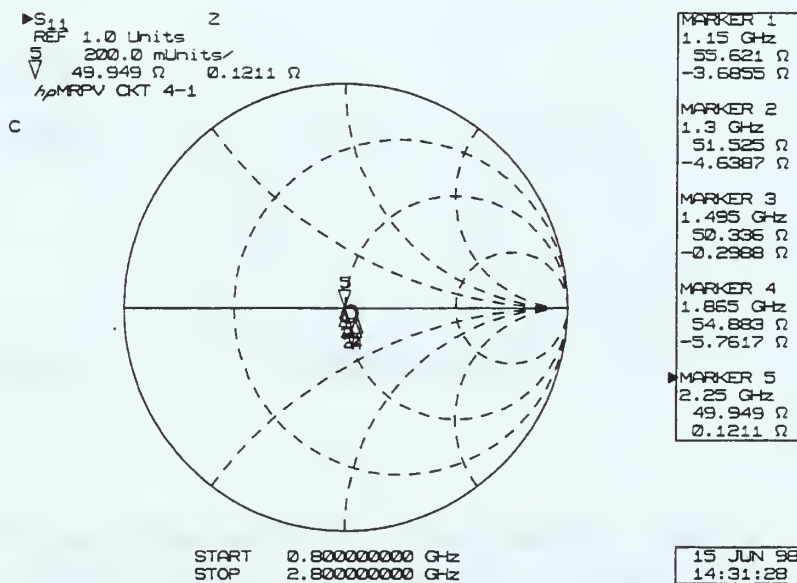


Figure 18. Impedance Smith Chart for 50 ohm Microstrip Line.
(Circuit 4-1: 111 mils wide line on FR-4 PC Board).
(a) Libra® Computer Simulation. (b) VNA Measurement.

D. DIODE CHARACTERIZATION

Design of the microstrip rectifier circuit required impedance matching the SMT-SBD to the 50 ohm semi-rigid coaxial line linking the MAV antenna. However, to design an impedance matching circuit, the impedance characteristics or scattering parameters of the Hewlett Packard SMT-SBD package must be determined.

A microstrip test fixture was designed and fabricated to help characterize the SMT-SBD package. This circuit was designated Circuit 4-2. This test fixture consisted of a 50 ohm microstrip line of width 111 mils with a gap large enough to mount the SMT-SBD as shown in Figure 19. The microstrip line width of 111 mils was calculated for a substrate relative permittivity of 4.8. This calculation is provided in Appendix B.

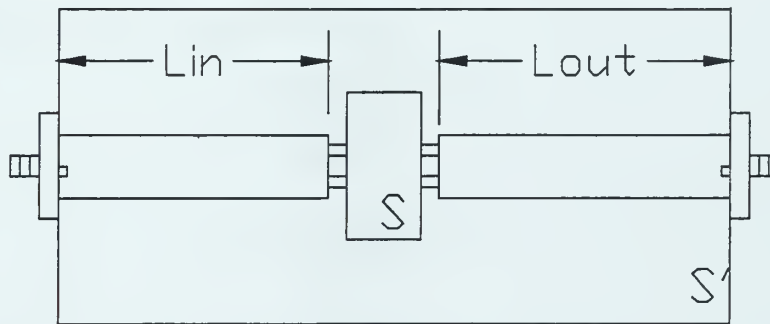


Figure 19. SMT-SBD Characterization Test Fixture (Circuit 4-2).

Scattering parameters for the SMT-SBD test fixture were measured using the HP8510C VNA over the frequency range of 0.8 to 2.8 GHz. Scattering parameters relate reflected and transmitted waves at the ports of a device to the incident waves [Ref 13]. Therefore scattering parameters provide a measure of the reflection and transmission coefficients at the ports of a device from which impedance can be determined. A two port device has four scattering parameters which can be written in matrix form as

$$S = \begin{bmatrix} S_{11} & S_{12} \\ S_{21} & S_{22} \end{bmatrix}, \quad (12)$$

where

$$S_{11} = \left. \frac{V_1^-}{V_1^+} \right|, V_2^+ = 0 \quad (13)$$

$$S_{12} = \left. \frac{V_1^-}{V_2^+} \right|, V_1^+ = 0 \quad (14)$$

$$S_{21} = \left. \frac{V_2^-}{V_1^+} \right|, V_2^+ = 0 \quad (15)$$

$$S_{22} = \left. \frac{V_2^-}{V_2^+} \right|, V_1^+ = 0. \quad (16)$$

Therefore S_{11} represents the reflection coefficient (Γ_1) at port 1 with no incident wave at port 2. Usually this is accomplished by terminating port 2 with its reference impedance.

When conducting measurements on the SMT-SBD, the output impedance of the SMT-SBD diode was not known, however, the test fixture used a 50 ohm microstrip line. Thus port 2 was terminated in a 50 ohm load and, in fact, the HP8510 VNA provides this termination automatically for a two port measurement.

The SMT-SBD scattering parameters $[S]$ were calculated from the measured scattering parameters of the entire SMT-SBD test fixture $[S']$ by shifting the reference planes of the test fixture VNA measurements. The test fixture scattering parameters have the same form as (12) - (16), except that primed quantities are used

$$[S'] = \begin{bmatrix} S'_{11} & S'_{12} \\ S'_{21} & S'_{22} \end{bmatrix} . \quad (17)$$

This shifting of the reference planes was accomplished by using

$$[S] = \begin{bmatrix} e^{j2\theta_{in}} S'_{11} & e^{j(\theta_{in} + \theta_{out})} S'_{12} \\ e^{j(\theta_{in} + \theta_{out})} S'_{21} & e^{j2\theta_{out}} S'_{22} \end{bmatrix} \quad (18)$$

where θ_{in} and θ_{out} are the electrical lengths of the input and output transmission lines of the diode test fixture (Circuit 4-2) and are given by

$$\theta_{in} = \frac{2\pi}{\sqrt{\lambda_e}} l_{in} \quad (19)$$

$$\theta_{out} = \frac{2\pi}{\sqrt{\lambda_e}} l_{out} . \quad (20)$$

These electrical lengths were determined by using the effective wavelength (λ_e) in the microstrip structure. An expression for λ_e is given by

$$\lambda_e = \frac{c}{\sqrt{\epsilon_e}} \frac{1}{f} \quad (21)$$

where c is the free space velocity, f is the frequency and ϵ_e is the effective relative permittivity of the microstrip line, which was defined earlier in (11).

The effective relative permittivity is an approximation that permits a simple transverse electromagnetic wave (TEM) model for propagation in a microstrip structure.

Since the microstrip has some of its field lines in the dielectric substrate and some in the air above the substrate, this structure does not support a pure TEM wave. The phase velocity of the TEM fields in the dielectric substrate region and in the air region above are not equal. The phase match at the substrate-air interface cannot be obtained by a TEM wave and the microstrip actually propagates a hybrid TM-TE (transverse magnetic – transverse electric) wave [Ref 13]. If the dielectric substrate is electrically thin ($d \ll \lambda_e$), the fields can be considered “quasi-TEM” and the phase velocity and propagation constants are accurately expressed as a function of an effective relative permittivity or effective relative dielectric constant. The microstrip is effectively modeled with substrate of ϵ_e both below and above the microstrip line.

The S-parameters for the Hewlett Packard HSMS-2825 surface mount silicon Schottky-barrier diode package are shown as an EEsof Libra[®] parameter file in Appendix C. The calculations demonstrating the method of shifting the reference planes are provided as a MathCAD[®] spreadsheet in Appendix E.

It is important to recognize that the reference plane translation is based on a 50 ohm system. The SMT-SBD rectifier circuit is not necessarily loaded by a 50 ohm device and therefore the scattering parameters obtained have some inherent uncertainty. A second means to measure $[S]$ of the SMT-SBD would have been with a load attached to second port. The load would be the MAV electrical motor, battery or an equivalent load. The rectifier circuit would then simplify to a one port network with measurements and calculations reduced to only S_{11} .

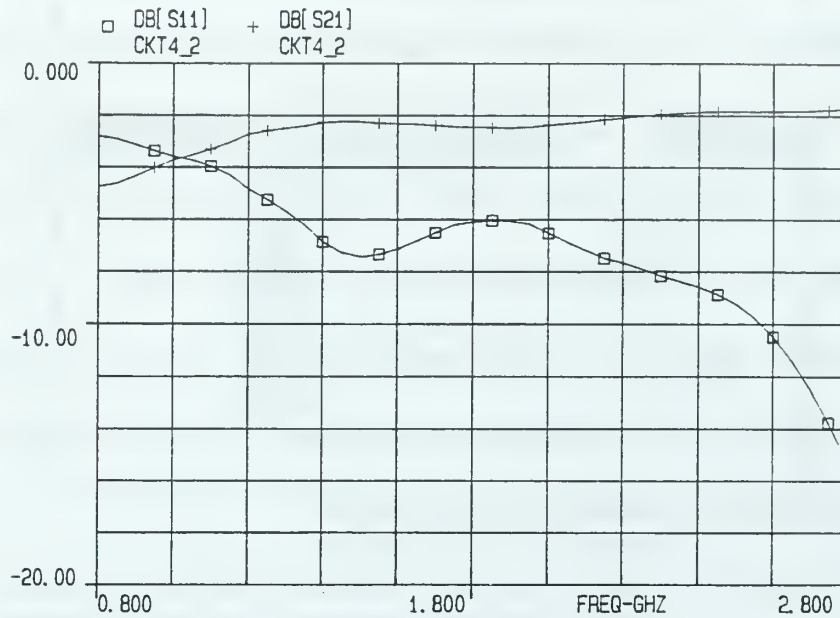
It is also important to recognize that the SMT-SBD was characterized at a single incident power level (10 dBm). Diodes are non-linear devices and their scattering parameters are a function of the incident power level. Ideally the scattering parameters should be measured at several incident power levels that fall within the rectifier range of operation. However, the maximum power of the HP8510 VNA is 25 dBm, and therefore higher incident power measurements would have to be conducted using a microwave power amplifier and slotted line techniques. The difficulty would then lie in designing an impedance matching circuit for a wide range of incident power levels.

E. COMPUTER VERIFICATION OF SBD CHARACTERISTICS

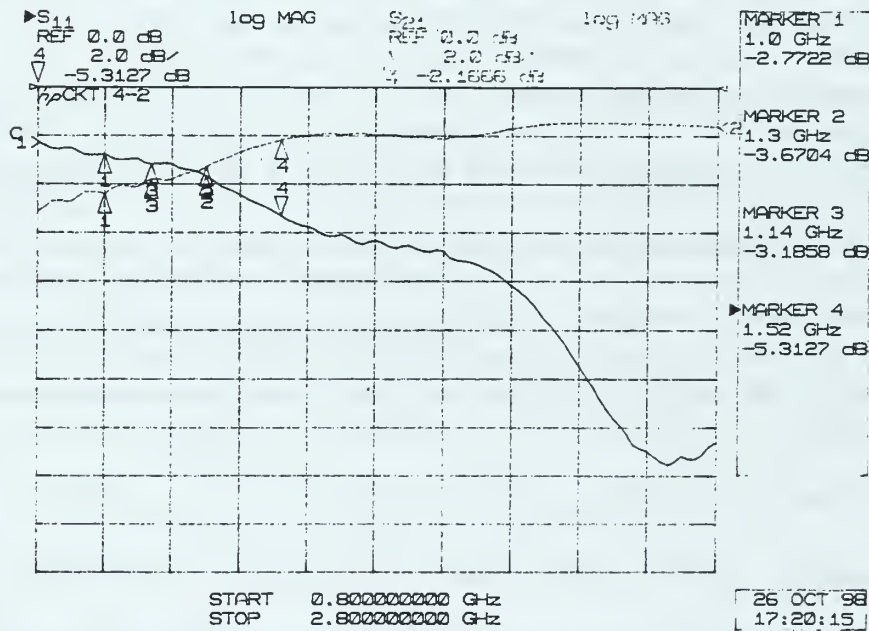
A Libra[®] model of the SMT-SBD test fixture (Circuit 4-2) was developed and simulated to verify the SMT-SBD scattering parameters obtained by reference plane translation of VNA measurements. The Libra[®] circuit file was developed using an S-parameter input file to model the SMT-SBD package. This input file (HP_diode.S2P) is the reference plane translation of VNA measurements on the diode test fixture (Circuit 4-2) and is attached as Appendix E. The Libra[®] circuit file for the SMT-SBD test fixture (Ckt4-2.ckt) is presented as Appendix F.

Simulation results for the Libra[®] model of Circuit 4-2 are shown in Figure 20a and the corresponding HP8510 VNA measurements in Figure 20b for comparison. It was found that the results vary significantly with termination type. The results shown for the simulation and measurements used 50 ohm terminations.

Simulated and measured results for return loss (S_{11}) and insertion loss (S_{21}) agree to within 2 dB at 1.0 and 1.3 GHz. The overall shape and values for both S_{11} and S_{21} tended to agree over the frequency band measured (0.8 –2.8 GHz). These results supported the validity of the shifted reference plane S-parameters for the SMT-SBD.



(a)



(b)

Figure 20. Return and Insertion Loss for SBD Test Fixture (Circuit 4-2).

(a) Libra[®] Computer Simulation. (b) VNA Measurement.

F. IMPEDANCE MATCHING THE RECTIFIER CIRCUIT

Return loss (S_{11}) measured on the 50 ohm test fixture (Circuit 4-2) demonstrated that the SMT-SBD has a poor impedance match to a 50 ohm transmission line at the desired operating frequencies of 1.0 and 1.3 GHz. Measured return loss was -6 dB which indicates that nearly 25% of the incident power is being reflected. Ideally, S_{11} is desired to be less than -20 dB. Because of the poor impedance match between SMT-SBD and 50 ohm transmission line, much of the power incident at the SMT-SBD would be reflected back towards the receiving antenna rather than rectified.

To prevent incident power from being reflected and re-radiated from the MAV antenna, three impedance matching circuits were considered to match the SMT-SBD to the 50 ohm semi-rigid coaxial line linking the antenna to the rectifier circuit. These included: (1) a design using lumped surface mounted components such as chip capacitors and chip resistors, (2) a microstrip open circuit stub, and (3) a microstrip shunt stub. Of the three designs investigated, only the shunt stub provided a closed DC loop, and therefore only this design was pursued. A diagram of the shunt stub (or shorted stub) microstrip circuit is shown in Figure 21. The design of this shunt stub circuit is described in the following paragraphs.

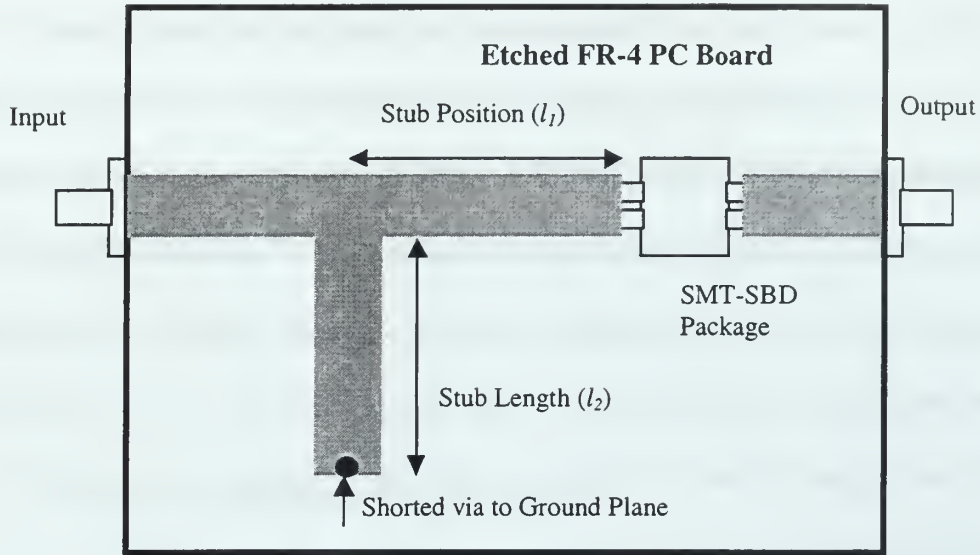


Figure 21. Shunt Stub Circuit Illustration.

1. Design of Shunt Stub Impedance Matching Circuit

The design of the shunt stub impedance matching circuit was based on the S-parameters of the SMT-SBD, determined through the reference plane shift on measurements of the diode test fixture (Circuit 4-2). Pozar describes a graphical procedure using the Smith Chart to design either an open or short circuit stub for impedance matching [Ref 13]. This procedure combines, in parallel, a length of short or open circuit microstrip transmission line with the unmatched circuit (SMT-SBD in this case) to form a circuit with a combined impedance having the desired value (50 ohms). This design method is frequency specific and therefore separate circuits are required for different operating frequencies. A summary of this procedure follows with annotated Smith Charts providing graphical insight. Figure 22 shows the Smith Chart annotation for the design of the 1.0 GHz rectifying circuit and Figure 23 for the 1.3 GHz rectifier circuit design. The steps involved in designing the matching circuits are described briefly in subsections *a* through *c* and the designs summarized in subsection *d*.

a. Locate the Device Input Admittance on the Smith Chart

The shifted reference plane S-parameters of the diode test fixture (Circuit 4-2) were modeled in Libra[®] and simulated to obtain a listing of equivalent input impedances. The equivalent input impedance obtained from the Libra[®] model simulation is provided in Appendix E. The device input impedance at the desired frequency was normalized to 50 ohms and plotted on the Smith Chart. This point is shown as Point A in Figure 22 (for 1.0 GHz) and Figure 23 (for 1.3 GHz). The resulting admittance was located at the mirrored location at Point B.

b. Determine the Location of Shunt Stub

A circle was drawn about the center of the Smith Chart with a radius that intersected the admittance and impedance points of the rectifier circuit. This is the constant VSWR circle for the SMT-SBD. A clockwise rotation (towards generator) around the constant VSWR circle from the admittance point (Point B) is made until the circle intersects the $G = 1$ offset circle (Point C). The arc distance provides the electrical distance (l_1) at which to place a stub tuner in front of the rectifier so that the real part of the input admittance (conductance) equals the normalized value. This distance is read off the outer portion of the Smith Chart and is in effective wavelengths (λ_e) for microstrip. A physical length is obtained by multiplying by the effective wavelength given by (21).

c. Determine the Shunt Stub Length

The shunt stub length (l_2) cancels the imaginary part of the combined input admittance (susceptance) at l_1 to zero. An open circuit stub or a shorted (shunt) stub could be employed, however an open circuit stub would not provide a closed path for DC. The

shunt stub length (l_2) was determined by following normalized susceptance curve from the point (l_1) in front of the SMT-SBD (Point C) to the edge of the Smith Chart (Point D). The arc from Point D to the short circuit admittance (Point E) is read off the outer portion of the Smith Chart. This angular distance is the required length of the shunt stub (l_2) in effective wavelengths and is converted to a physical length by multiplying the value for λ_e , provided in (21).

d. Calculate the Shunt Stub Length

The procedure described above was followed to design impedance matching circuits at 1.0 and 1.3 GHz for the shifted impedance of the SMT-SBD. The microstrip design constants are shown in Table 2 and the shunt stub design in Table 3.

ϵ_r	W (0.001 in or mils)	d (0.001 in or mils)	ϵ_e
4.8	105	70	3.53

Table 2. Microstrip Design Constants.

Frequency	λ_e		l_1 location of shunt		l_2 shunt length	
(GHz)	(meters)	0.001 in (mils)	from Smith Chart (λ_e)	Physical distance 0.001 in (mils)	from Smith Chart (λ_e)	Physical distance 0.001 in (mils)
1.0 GHz	0.1597	6286	0.152	955	0.071	446
1.3 GHz	0.1228	4835	0.146	706	0.089	430

Table 3. Smith Chart Determined Lengths and Positions for Shunt Stub.

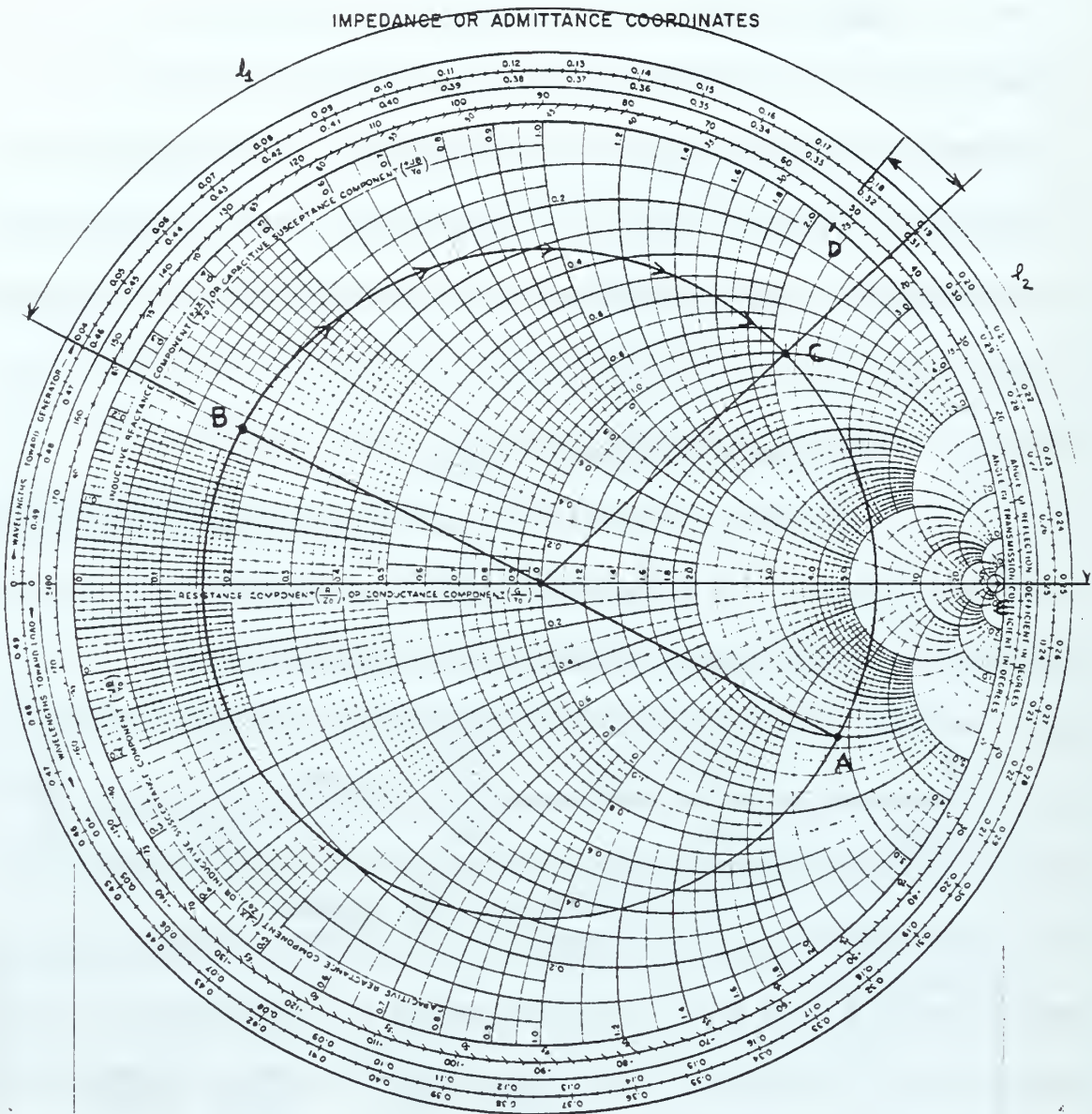


Figure 22. Smith Chart for Shunt Stub Impedance Matching of SMT-SBD Rectifier at 1.0 GHz.

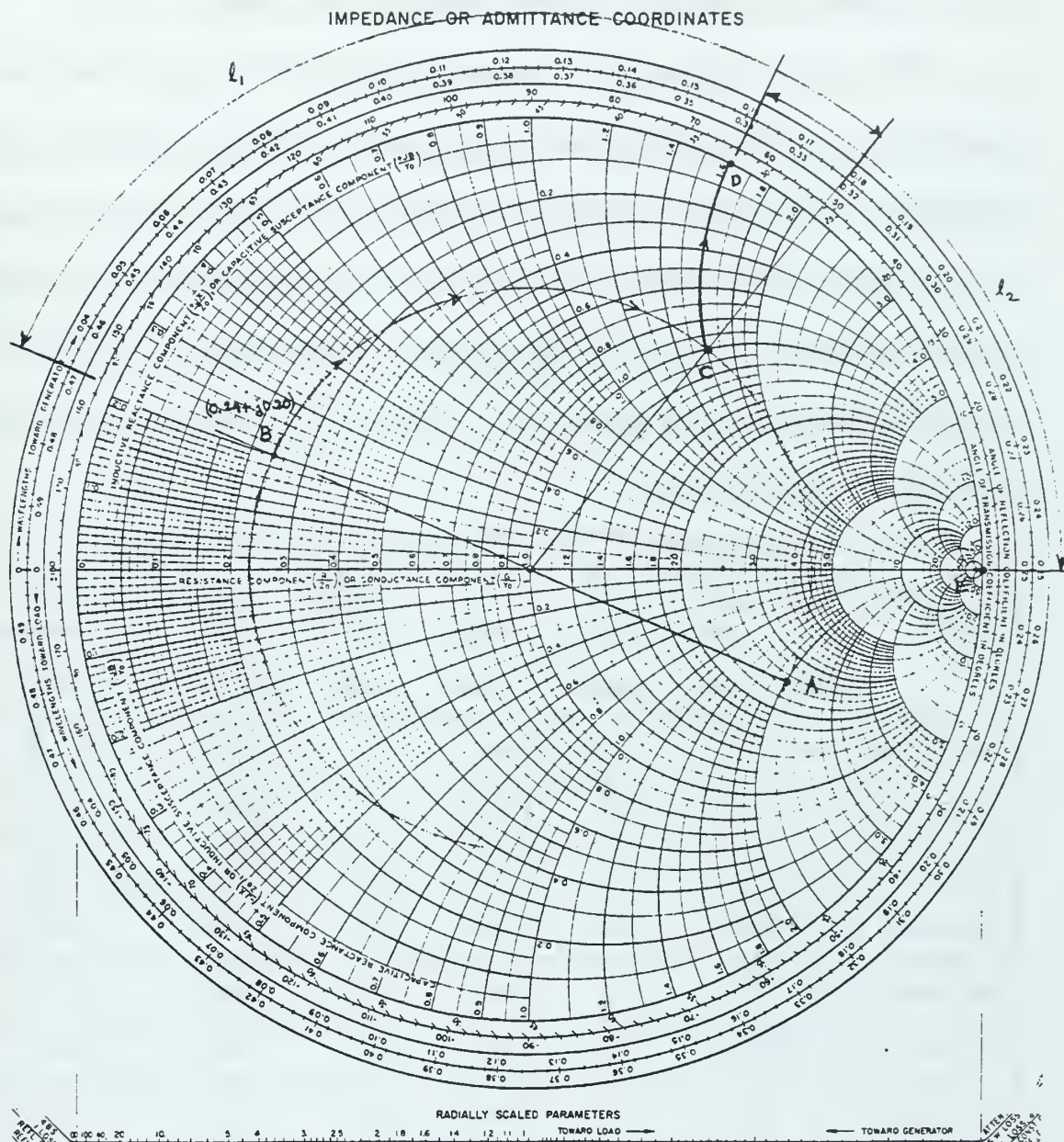


Figure 23. Smith Chart for Shunt Stub Impedance Matching of MAV Rectifier Circuit at 1.3 GHz.

2. Computer Simulations of Shunt Stub Matching Circuits

EEsof Libra[®] computer simulation circuit files (models) were developed using the S-parameters of the SMT-SBD and the shunt stub designs obtained graphically using the Smith Chart. Libra[®] circuit models were developed to simulate and evaluate changes to the design parameters. Models were labeled with the convention Circuit 6xx for the 1.0 GHz operation and Circuit 7xx for the 1.3 GHz operation. The xx designation is a placeholder representing the version of the circuit. Table 4 provides a summary of these models with their particular design parameters.

Libra [®] Circuit Model	Design Freq (GHz)	50 ohm Line width (mils)	Input Line Length (mils)	Output Line Length (mils)	Shunt Stub Position (l_1) (mils)	Shunt Stub Length (l_2) (mils)	S_{11} at Design Frequency (dB)
Ckt_6b2.ckt	1.0	111	275	260	445	955	-29.1
Ckt_6c2.ckt	1.0	111	275	260	475	900	-21.1
Ckt_6e2.ckt	1.0	111	275	260	445	900	-18.6
Ckt_6f2.ckt	1.0	111	275	260	475	955	-20.3
Ckt_7d1.ckt	1.3	111	275	260	710	440	-28.7
Ckt_7e1.ckt	1.3	111	275	260	660	440	-19.0
Ckt_7f1.ckt	1.3	111	275	760	710	440	-18.4
Ckt_7g1.ckt	1.3	111	275	260	710	390	-17.2
Ckt_7h1.ckt	1.3	111	275	260	710	490	-24.2

Table 4. Design Variation Simulations for the Shunt Stub Impedance Matching Circuit.

The circuit 6x2 model was changed by varying the stub length by 55 mils and stub position by 30 miles. Figure 24 displays the effect on the return loss (S_{11}) for these changes in circuit configuration. These models used short input and output microstrip lines to the rectifier circuit to permit the entire circuit to fit within the projected size of the upper half of the MAV vehicle body.

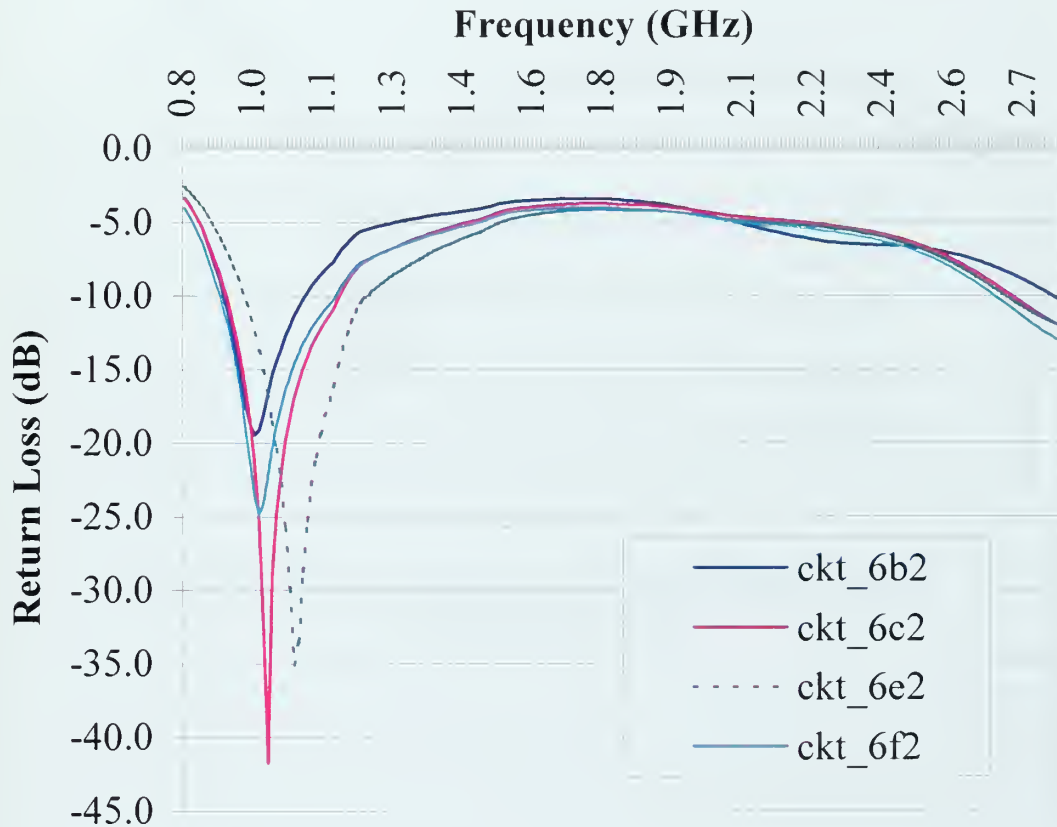


Figure 24. Circuit 6x2 Return Loss for Libra® Model Variation (1.0 GHz Rectifier).

The circuit 7x1 model was changed by varying the stub length by 50 mils and stub position by 50 mils. Figure 25 displays the effect as simulated by EEsof Libra[®] on return loss (S_{11}) using these variations.

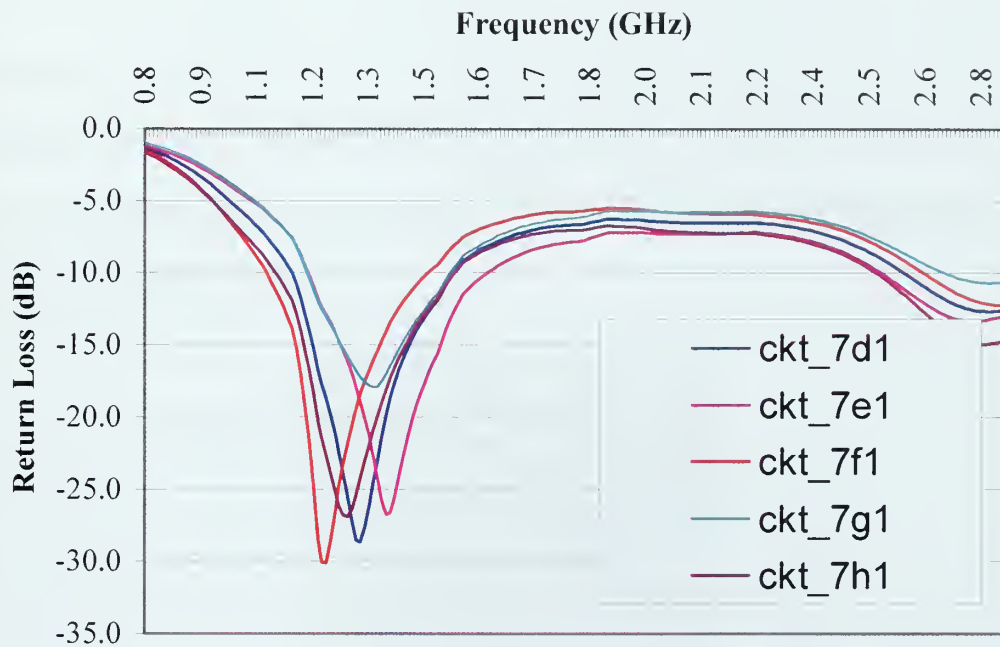


Figure 25. Circuit 7x1 Return Loss by Design Model Variation
1.3 GHz Rectifier Circuit.

3. Fabrication of Shunt Stub Matching Circuits

Shunt Stub Circuits 6c2 and 7d2 were fabricated. These fabricated circuits were labeled Ckt 6C2 for the 1.0 GHz rectifier and Ckt 7d-1 for the 1.3 GHz rectifier design. Only one version of Ckt 6C2 was fabricated with the intent to use it to demonstrate MAV wireless power transfer. For this demonstration, Ckt 6C2 included a miniature DC motor connected as a load via 18 gage wire. This microstrip rectifier circuit did not include an output connector and thus was considered a 1 port network. A photo of Ckt 6C2 connected to the VNA for testing is shown in Figure 2.19.

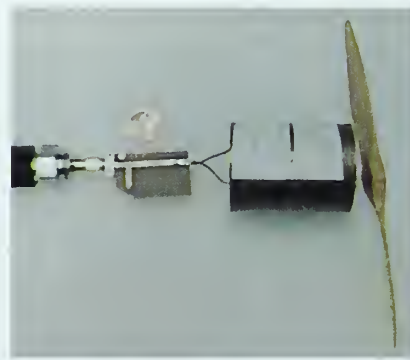


Figure 26. Circuit 6C2 Return Loss Measurement Setup
(1.0 GHz Rectifier Circuit).

The 1.3 GHz rectifier circuit (Ckt 7d-1) was fabricated after considerable experience with Ckt 6C2 measurements. Some of the lessons learned from the Ckt 6C2 experience included fabricating multiple copies and including a connector on the output line of the rectifier to simplify VNA and rectification efficiency measurements. Two principal versions of Ckt 7d-1 were produced: Ckt 7d-1 identical to that described by the Libra[®] simulation model, and Ckt 7d-5 which included a miniature DC motor connected to Port 2 as a load via short 18 gage wire. Both versions had SMA connectors on the output side of the rectifier to allow easier measurements. A photo of Ckt 7d-1 undergoing measurement

by the VNA is shown in Figure 27. The complete test setup showing the HP8510 Vector Network Analyzer is shown in Figure 28.

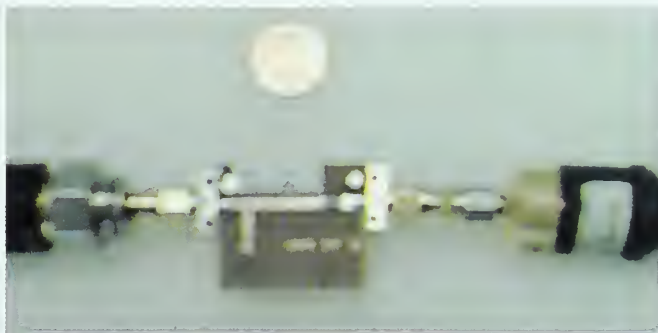


Figure 27. Circuit 7d-1 Return Loss Measurement Setup (1.3 GHz Rectifier Circuit).



Figure 28. HP8510 Vector Network Analyzer (VNA) Return Loss Measurement Setup.

4. VNA Measurement and Analysis for 1.0 GHz Rectifier Circuit (Ckt 6C2)

The return loss (S_{11}) of the 1.0 GHz rectifier circuit (Ckt 6C2) was measured using the HP8510C VNA. Data from the VNA measurements are shown in Figure 29.

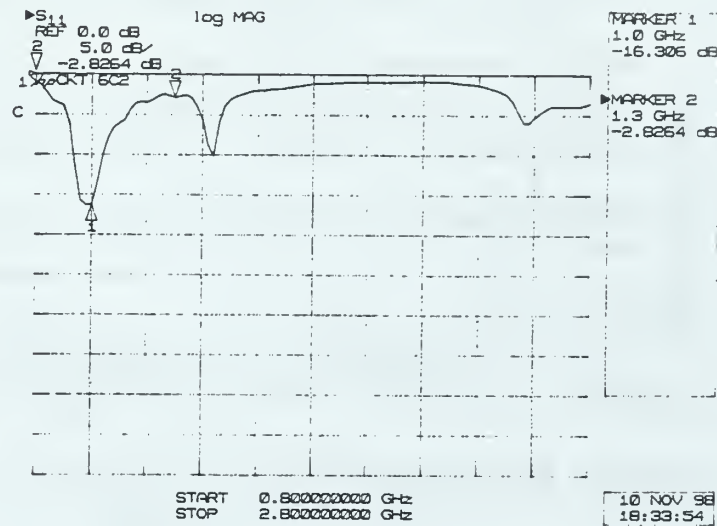


Figure 29. VNA Measured Return Loss of Ckt 6C2 (1.0 GHz Rectifier Circuit).

Comparison between return loss calculated from the Libra[®] computer simulation and that measured via the HP8510 VNA is shown in Figure 30. This comparison shows that the VNA return loss measurements follow the predicted return loss from the Libra[®] computer simulation. Some discrepancy is noted in the overall level of return loss at the frequency selected for matching (1.0 GHz). Where the Libra[®] model predicted a return loss of -25 dB, the VNA measured value produced -16 dB. The difference could be attributed to manufacturing tolerances, however, it is noted however that the physical Ckt 6C2 was not completely identical to the Libra[®] model. The Libra[®] computer model was terminated at

both the input and output lines in 50 ohms, whereas the output port for Ckt 6C2 was connected to the miniature DC motor via short wire leads.

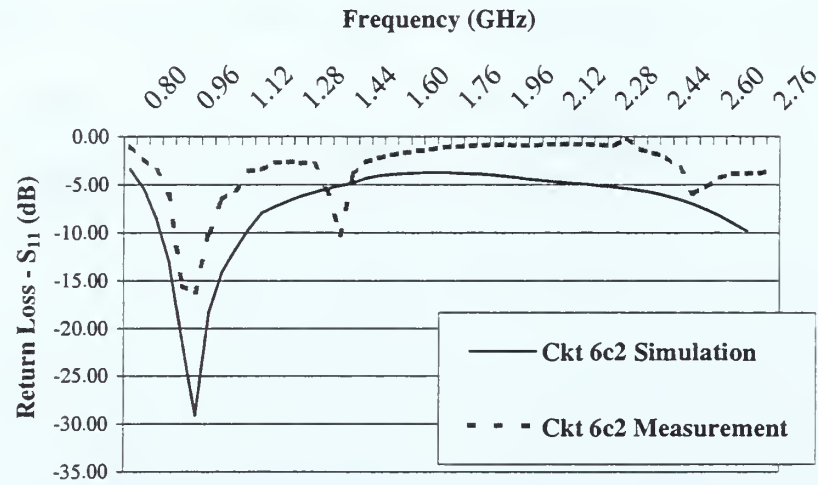


Figure 30. Measured and Simulated Return Loss for Circuit 6C2 (1.0 GHz Rectifier Circuit).

5. VNA Measurement and Analysis for 1.3 GHz Rectifier Circuit (Ckt7d-1 and Ckt 7d-5)

The return loss (S_{11}) of the 1.3 GHz rectifier circuit was measured using the HP8510C VNA with several loaded configurations. Plots of sample VNA measurements of return loss and insertion loss (S_{21}) for Ckt 7d-1 are shown in Figure 31. The measurement configuration had Port 2 of Ckt 7d-1 terminated in 50 ohms. The VNA used a 2 Port 3.5 mm calibration set, which gives a load condition equivalent to the Libra computer model.

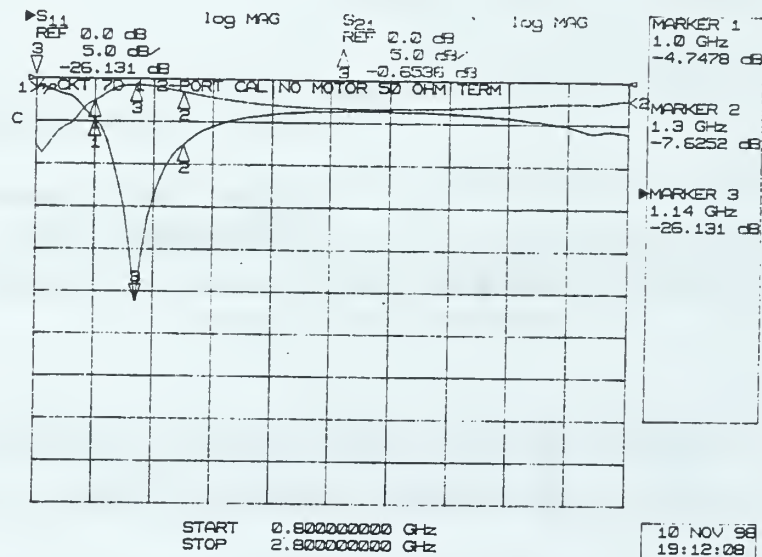


Figure 31. Measured Return Loss and Insertion Loss for Circuit 7D-1
Circuit is Terminated in 50 ohms and 2-Port Calibration Set Used.

Comparison between return loss calculated from the Libra[®] computer simulation and that measured with the VNA is shown in Figure 32 for Ckt 7d-1. As shown in Figure 32, the return loss measurements of Ckt 7d-1 do not fully match those obtained from the simulation of the Libra[®] model. The shape of the return loss curve over the frequency band is very similar, however, the minimum point of reflected power (smallest S_{11}) does not

occur at the same frequency. This difference is likely due to an inaccuracy in the fabrication of the shunt stub trace and possible differences in the dielectric constant of the FR-4 PC board material.

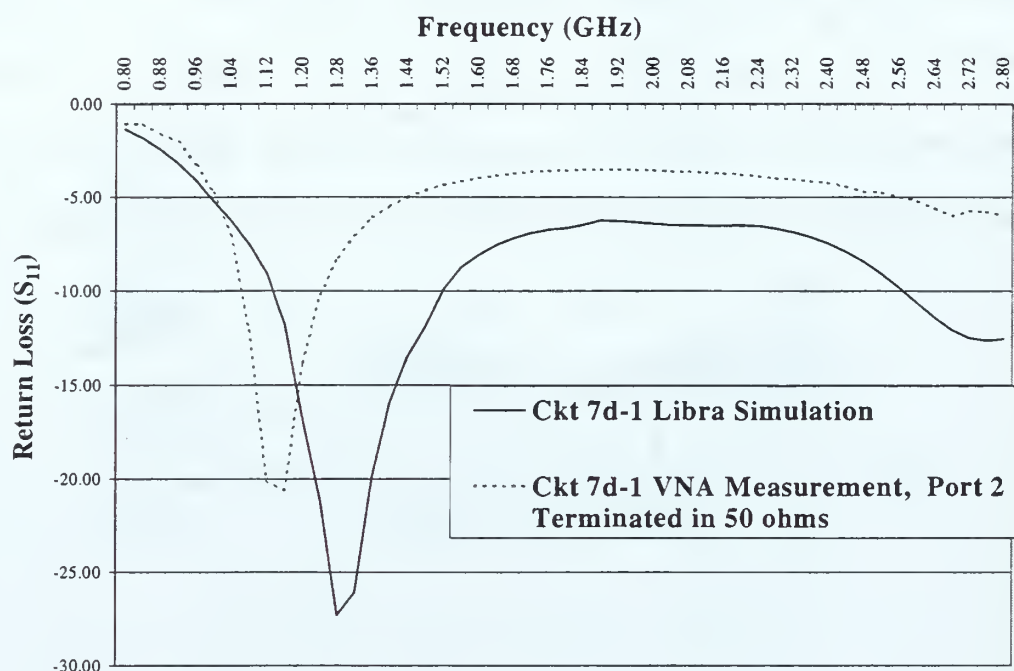


Figure 32. Simulated and Measured Return Loss for Ckt 7d-1 Where Port 2 is Terminated in 50 ohms.

To understand how output port loading affects the rectifier circuit, return loss for Ckt 7d-1 was first measured with Port 2 open circuited and then with Port 2 terminated in 50 ohms. The results of these measurements are shown in Figure 33. The data clearly show a need for a termination or some type of load on the circuit in order to achieve an acceptable return loss.

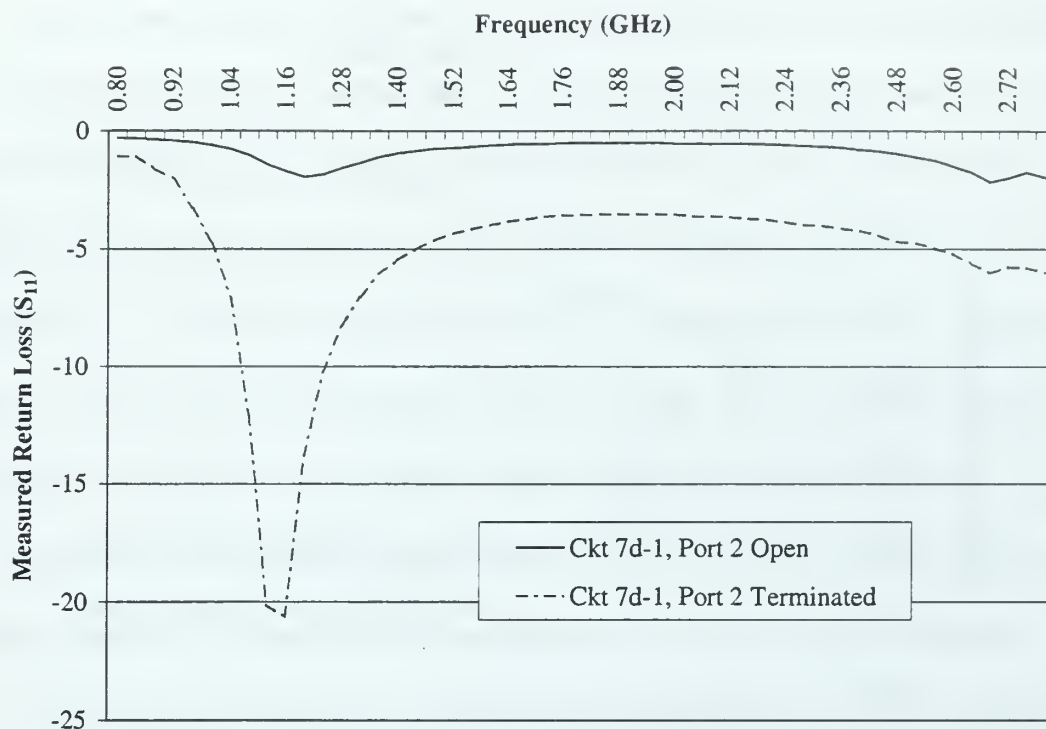


Figure 33. VNA Measured Return Loss for 1.3 GHz Rectifier Circuit (Ckt 7d-1) Without DC Motor Attached, Port 2 Configured with an Open Circuit and with 50 ohm Termination.

A second version of the 1.3 GHz rectifier circuit was fabricated and assembled with a miniature DC motor as a load on Port 2 (Ckt 7d-5). Figure 34 displays the return loss measurements for the two conditions of Port 2: (a) connected to a miniature DC motor and (b) terminated in 50 ohms. Comparison of data for the motor loaded rectifier shows that the motor on Port 2 provides a better return loss than when Port 2 is terminated in 50 ohms. Thus the rectifier circuit terminated with the motor seems to provide a better means to match the input of the rectifier than when a 50 ohm termination is placed on Port 2.

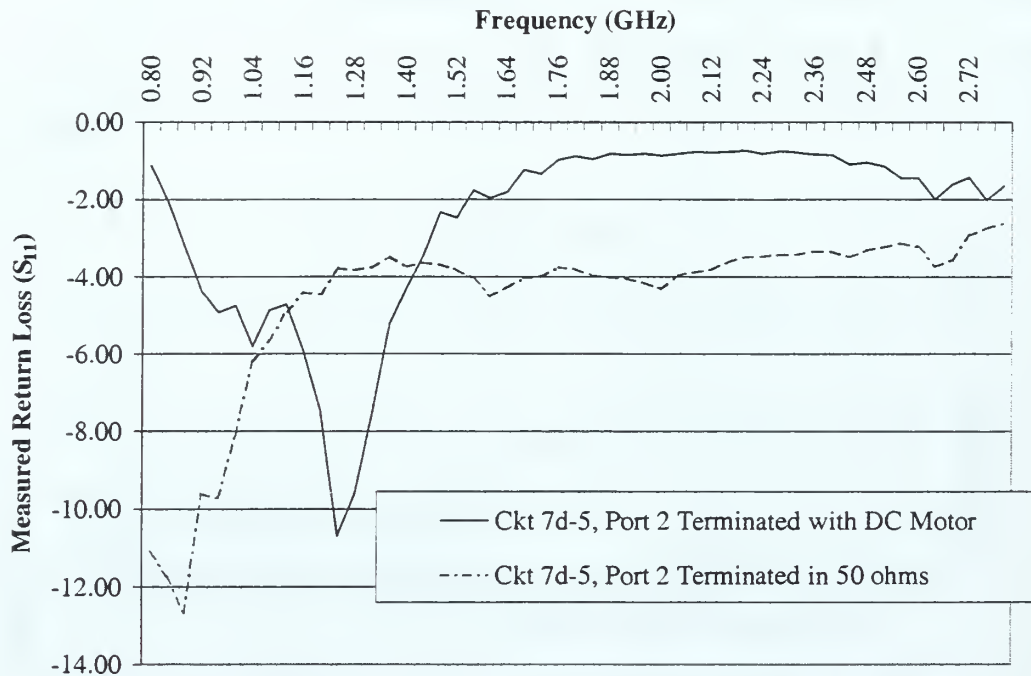


Figure 34. VNA Measured Return Loss for 1.3 GHz Rectifier (Ckt 7d-5)
Port 2 Terminated with DC Motor and in 50 ohms.

G. RECTIFIER CIRCUIT DESIGN - CONCLUSIONS

This chapter dealt with the design of the microstrip rectifier with a primary goal to provide an impedance match to a 50 ohm coaxial transmission line input from the MAV antenna. Further design to improve rectification efficiency is explored in Chapter V, where rectification efficiency measurements are described. However overall efficiency is affected by how much energy is passed through the rectifier rather than reflected from it. Therefore providing a good impedance match from the antenna to the rectifier becomes important.

Design of the microstrip circuit required an accurate knowledge of the electrical properties of the material being used. Properties such as dielectric constant of the substrate and conductivity of the conductors influence the design of the microwave circuitry. Use of

the FR-4 PC board material was a serious impediment towards developing a good design and maintaining circuit fabrications with low return loss. The relative permittivity of the dielectric substrate was estimated from measurements on sample circuits that were compared to the computer (Libra[®]) simulation results. However, it is shown that an error in using an ϵ_r of 4.8 verses may have resulted in a 37 percent error for the relative dielectric constant used in designing the microstrip circuit. This error resulted in the microstrip width that was approximately 32 mils thinner (111 mils verses 147 mils) than should an ϵ_r of 3.5 had been used in the design calculations. This error also effects the determination of the scattering parameters for the SMT-SBD package, thereby compounding the problem.

One major improvement in the design of this circuit would be to use a high quality substrate. Use of a substrate with tightly regulated substrate parameters would provide allow a more accurate design of the impedance matching circuit for the SMT-SBD package. An example of a tightly controlled permittivity would be RO4350 high frequency woven glass reinforced ceramic filled laminate, produced by Rogers Corporation of Chandler, Arizona, USA. The RO4350 material has $\epsilon_r = 3.48 \pm 0.05$ and can be fabricated into microstrip circuits using the same etching or routing methods used on FR-4 PC Board material.

Another improvement may be to use a high quality substrate with a high permittivity. High quality substrates with a high permittivity would shrink the size of the microstrip rectifier circuit, thereby providing an easier fit within the MAV structure. A substrate material with high permittivity is RT/duroid 6010LM ceramic filled laminate also produced by Rogers Corporation. RT/duroid 6010LM has $\epsilon_r = 10.2 \pm 0.25$. However,

fabrication methods for RT/duroid 6010LM are more complex as the substrate is ceramic and typical FR-4 PC board etching methods are not reliable. Another high permittivity substrate material is Epsilam-10 produced by the Electronic Products Division of the 3M Corporation. Epsilam-10 has $\epsilon_r = 10.2 \pm 0.25$ and uses a ceramic filled Teflon compound for the substrate and can be processed like conventional printed circuit board material (such as FR-4).

A second area of concern for rectifier circuit design is how to handle loading of the rectifier. It is evident that the rectifier circuit must be loaded in order to avoid large return losses. As shown in Figure 34, this load could be the miniature DC motor of the MAV. However, the impedance discontinuity between the leads of the DC motor and the output microstrip structure of the rectifier circuit increases the return loss, as shown in the differences between Figure 33 and Figure 34. VNA measurements of return loss were unstable when there was appreciable DC motor lead length. Minimization of these lead lengths was determined to be essential in order to achieve repeatable results.

III. ANTENNA DESIGN

Previous researchers in wireless power transfer concentrated on developing antenna systems that provided the greatest RF-to-DC conversion efficiency and could transfer large amounts of power. Size and weight did not play a crucial role in determining antenna type and usually these designs tended to be large flat array antennas. These antennas were fastened to the bottom of the vehicle and provided WPT for a single orientation between the transmitter and receiver. These configurations were acceptable for a stationary vehicle or for a system that could retain a certain relative position and orientation between transmitting and receiving antenna.

The operation of this vehicle (MAV) requires that wireless power transfer be independent of rotation or position. Therefore the MAV receiving antenna must be able to receive power from nearly any direction. In addition the antenna must not add appreciably to the size nor to the weight of the vehicle. The receiving antenna must be an efficient receiver of microwave energy and be able to transfer this energy to the rectifying circuit with minimal signal loss or reflection.

This chapter describes the design and fabrication of the second basic part of the MAV WPT receiving system: the antenna. This antenna must meet the operational requirements described previously and fit within the physical parameters of the Lutronix vehicle: a cylinder with diameter of 4.4 cm and length of 10.2 cm. This chapter describes the antenna configuration, computer modeling and simulations conducted for antenna design, fabrication of the antenna, and measurements.

A. ANTENNA TYPE SELECTION

One MAV requirement is to make the vehicle as lightweight as possible. With this in mind, the vehicle body was chosen to become the antenna for WPT. Therefore, the MAV body serves two purposes, as an antenna for wireless power transfer and as the physical structure and aerodynamic shape for the MAV.

Two antenna types that could be chosen to meet the physical shape of the Lutronix MAV are the conformal array antenna and the fat dipole antenna. A conformal array antenna would require a complex feeding structure to interface the array to the rectifier. This structure would add weight and require space on the vehicle.

The fat dipole antenna readily conforms to the size and shape of the Lutronix's MAV which is shown in Figure 35. A single coaxial feed can be used to minimize weight and space requirements. The MAV's dimensional constraints required the dipole to be approximately 10.2 cm in length and 4.4 cm in diameter. Design parameters not constrained by the vehicle geometry include the feedpoint location, and size of gap about the feedpoint.

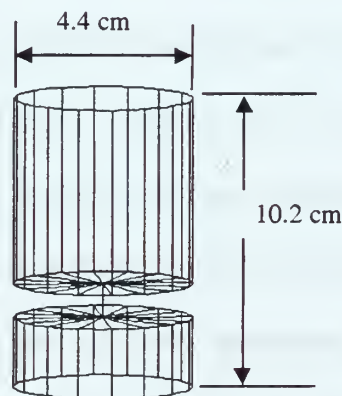


Figure 35. Dimensions for MAV Dipole Antenna.

B. DIPOLE ANTENNA GEOMETRY

Antenna design principally involved selecting the following parameters of the dipole antenna: (1) overall physical length, (2) feed point location, and (3) feedpoint gap size. The antenna design should maximize received power and provide a driving point impedance that matches that of the interface to the rectifier circuit. This interface is a 50 ohm semi-rigid coaxial cable which is used as the feed. The rigid coaxial cable also provides the mechanical structure holding the microstrip rectifier circuit within the upper section of the MAV antenna.

The maximum overall antenna length was determined by the size of the Lutronix vehicle, however, it is worthwhile to understand how length affects the impedance characteristics of the MAV antenna. MAV requirements coupled with technology improvements will likely drive future MAVs towards a smaller size. Should a smaller vehicle be considered, the impedance characteristics of the smaller antenna may require a new operating frequency for WPT or changing system impedance to match the new driving point impedance.

The radiation resistance is largely dependent upon overall length. Dipole antenna radiation resistance for a thin dipole has been shown to be frequency dependent and can be calculated by [Ref 14]

$$\begin{aligned} R_{rad} = & \frac{\eta}{2\pi} \left\{ C + \ln(kl) - C_i(kl) + \frac{1}{2} \sin(kl) \right. \\ & \times [S_i(2kl) - 2S_i(kl)] + \frac{1}{2} \cos(kl) \\ & \left. \times [C + \ln(kl/2) + C_i(2kl) - 2C_i(kl)] \right\} \end{aligned} \quad (22)$$

where η is the free space impedance (377 ohms), l is the overall length of the dipole, k is the free space wave number which is written as

$$k = \frac{2\pi}{\lambda}, \quad (23)$$

and λ is the wavelength in free space. The sine integral, $S_i(kl)$, and cosine integral, $C_i(kl)$, are defined as

$$S_i(x) = \int_0^x \frac{\sin(y)}{y} dy \quad (24)$$

$$C_i(x) = \int_{\infty}^x \frac{\cos(y)}{y} dy . \quad (25)$$

Figure 36 provides a plot of calculated radiation resistance vs. dipole length in terms of wavelength for a thin dipole. Calculated radiation resistance verses thin dipole antenna sizes for frequencies of interest (1.0 GHz, 1.3 GHz, and 2.45 GHz) are shown in Figure 37. These plots demonstrate that higher transmit frequencies tend to increase the radiation resistance for an antenna size on the order of the Lutronix MAV (10.2 cm in length). Figure 37 also shows that a 10.2 cm long, thin dipole antenna would have a theoretical radiation resistance close to 25 ohms at 1.0 GHz, 200 ohms at 2.45 GHz, and at 1.3 GHz the radiation resistance is approximately 50 ohms, which is desired for impedance matching to the rectifier circuit.

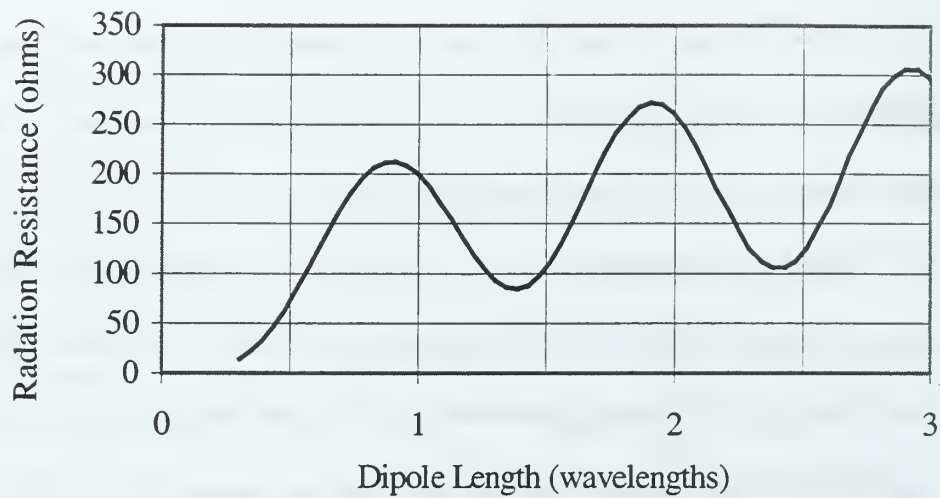


Figure 36. Dipole Antenna Radiation Resistance.

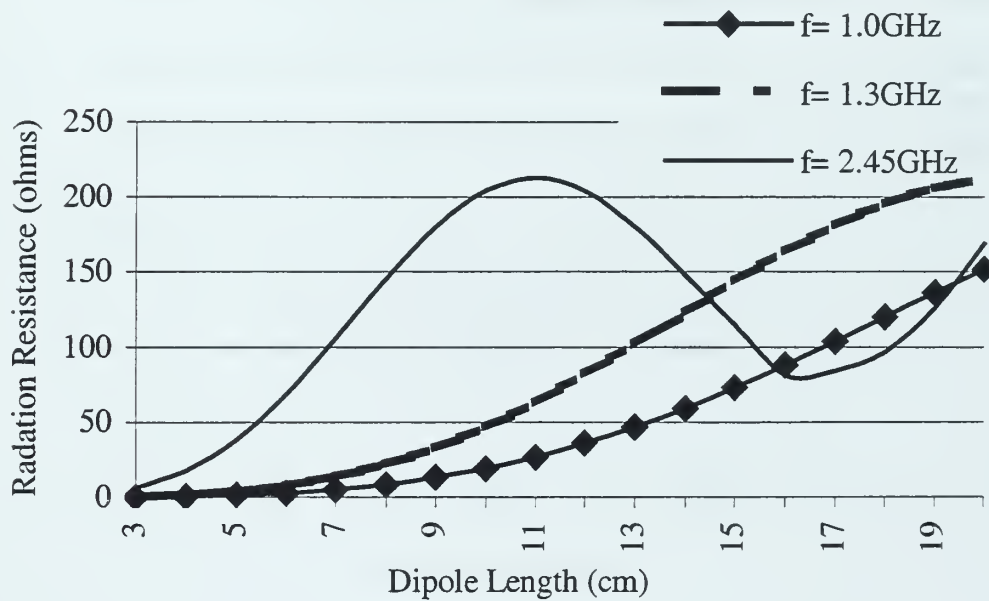


Figure 37. Calculated Radiation Resistance for a Thin Wire Dipole Antenna at Proposed WPT Frequencies.

The radiation resistances shown in Figure 36 and Figure 37 are based on a sinusoidal current distribution over a thin wire dipole. A thick dipole may be expected to differ significantly in radiation resistance and to have a significant reactance. Collin provides radiation resistance and input reactance graphs for dipole antennas of varying wire thickness [Ref 15]. Data for these graphs come from hundreds of impedance measurements made by Brown and Woodward [Ref 16]. For thicker dipole antennas, the radiation resistance and input reactance tend to have smaller variations over a wide range of frequencies. Selected data points for a dipole antenna of length similar to the proposed MAV (10.2 cm) is shown in Figure 38 for resistance and Figure 39 for reactance over the various frequencies of interest (1.0 GHz, 1.3 GHz and 2.45 GHz).

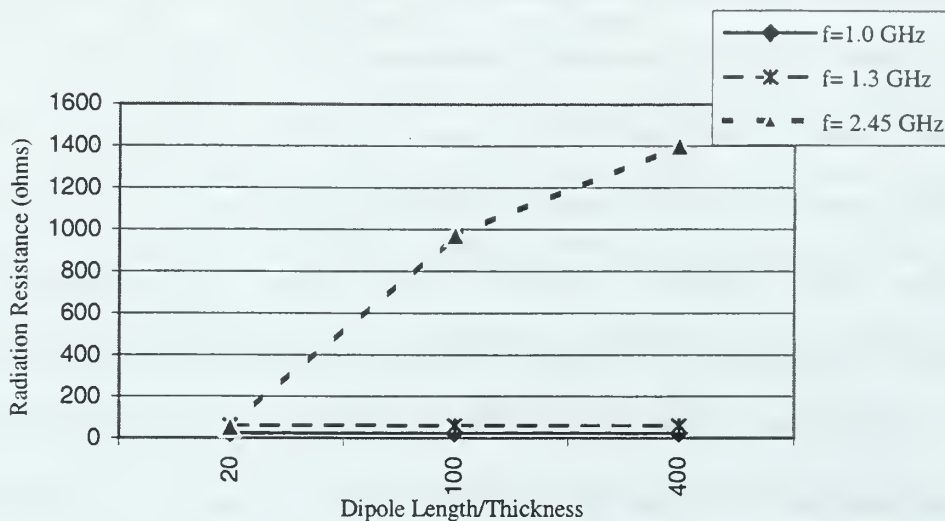


Figure 38. Radiation Resistance of 10.2 cm long Dipole Antenna as Thickness Varies [Ref 15].

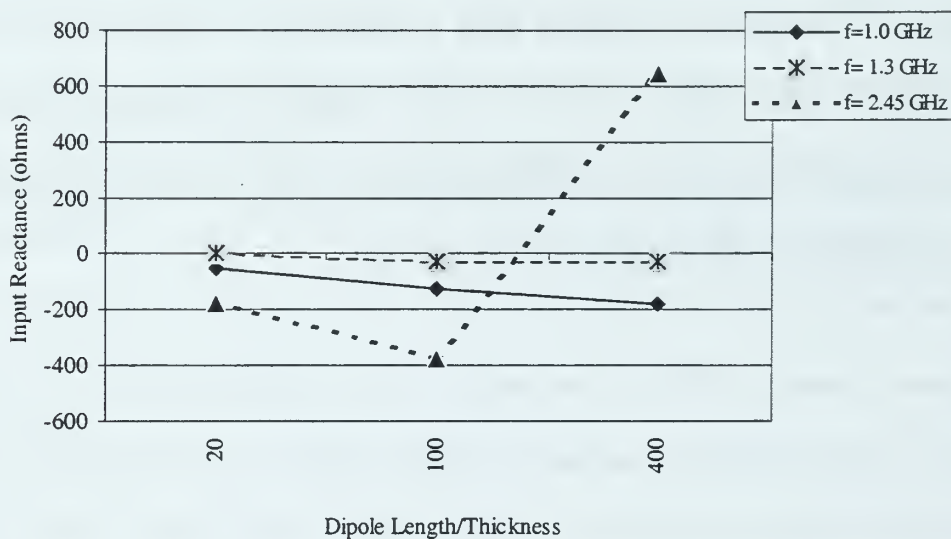


Figure 39. Reactance for a 10.2 cm long Dipole Antenna as Thickness Varies [Ref 15].

The fat dipole MAV antenna can be assumed to have complex impedance, similar to that shown by Collin and not readily obtainable through analytical expressions. However several numerical simulation methods exist to estimate the complex impedance of any radiating structure. Use of numerical simulation methods allows the variation of multiple antenna design parameters such as diameter, feedpoint position and feedgap size. By varying one parameter while keeping others constant, impedance trends can be established.

One numerical method is called the Method of Moments (MoM), which was applied to electromagnetics by Harrington [Ref 17]. MoM was used in computer simulations to develop impedance trends for the MAV antenna while varying geometry parameters. Numerical electromagnetic modeling for MoM calculations is discussed in Section C. Results of computer simulations using a commercially available MoM computer code (GNEC[®]) is discussed in Section D. MoM numerical simulations using GNEC[®] were conducted to design an antenna feedpoint geometry that would have an impedance match to the 50 ohm rigid coax cable feeding the antenna.

C. NUMERICAL ELECTROMAGNETIC CODE (NEC) MODELING OF MAV ANTENNA (FAT DIPOLE ANTENNA)

Computer modeling and simulation of the fat dipole MAV antenna used an adaptation of the Numerical Electromagnetic Code Version 4.1 (NEC 4.1) called Government NEC (GNEC[®]). GNEC[®] is a Microsoft Windows 95/NT compatible computer program produced by Nittany Scientific of Hollister, California [Ref 19]. GNEC[®] performs electromagnetic calculations by using a modified form of NEC 4.1 FORTRAN computer program which is owned by the US Government and developed at the Lawrence Livermore National Laboratory [Ref 19]. NEC 4.1 and GNEC[®] are US Government controlled computer codes and have distribution limitations. Other less accurate versions of NEC (NEC 2 and NEC 3) are available for export to other countries and are used world-wide.

The output of the NEC codes includes the antenna radiation pattern and current distribution on the antenna structure at a single frequency. Antenna input impedance and voltage standing wave ratio (VSWR) can be computed over a range of frequencies. The NEC computer codes rely on text based input and output files. There are no tools for visualization of the input geometry or the output data. GNEC[®], however, provides a graphical user interface (GUI) to NEC and allows visualization of input geometry files and output data files in graphical form. Graphical output includes displays of wire frame models, and at a single frequency, current distributions on the wires of the structure and radiation patterns in both two-dimensional sections and three-dimensional volumetric plots. Graphs of input impedance and VSWR over a frequency range can also be produced readily by GNEC[®].

The computational methods used for NEC and MoM codes require some knowledge of how they operate in order to develop models that achieve accurate simulation results. The following sections briefly describe the theory behind MoM type codes, (in particular NEC 4.1 and GNEC[®]), discuss the antenna modeling requirements of these programs, and, provide a description of how the MAV antenna GNEC[®] model was developed.

1. NEC - Method of Moments Solution Description

The NEC computer programs analyze the electromagnetic response of antennas and scatters by a numerical solution of an integral equation using the Method of Moments (MoM) described by Harrington [Ref 17]. Thin wire segments model antenna structures, where inter-connected wire mesh grids approximate solid surfaces. When the structure is a closed volumetric surface, then surface patches can be used to model the geometry. The electric field integral equation (EFIE) is solved for wire frame models and the magnetic field integral equation (MFIE) is solved when patches are used. A hybrid EFIE-MFIE is solved when both wires and patches are used.

The integral equations (IE) reduce to a set of linear simultaneous equations that are solved using matrix methods. The first step is to assume a basis function for the current on individual thin wire segments. MoM computer codes have used many different types of basis functions for the current on a segment, however the most popular are the pulse and sinusoidal functions. To calculate the current on the wire segment j , GNEC[®] and NEC 4.1 use the three term sinusoidal expansion basis function,

$$I_j(s) = A_j + B_j \sin k_s(s - s_j) + C_j [\cos k_s(s - s_j) - 1] \quad (26)$$

where s is the location on the wire segment for the current to be calculated, s_j is the center location of the wire segment, k_s is the wave number in the medium containing the wire, and A_j, B_j, C_j are constants.

The three constants (A_j, B_j, C_j) in (26) are solved for by applying the boundary conditions at the ends of wire segments and on the surface of the wires. The boundary conditions at the ends of wire segments require conformity to Kirchoff's Current Law (conservation of current between segments). At the wire surface, Gauss' Law must be satisfied where the tangential electric field is zero at the surface of a perfect electrical conductor. Solutions for the three constants of the current basis function provide the current on a single segment. The currents on all segments are solved for simultaneously by GNEC[®] and NEC 4.1 using linear algebra techniques.

The NEC and MoM computer simulations start with a segmented wire frame model of the structure (antenna) and a voltage specified at the feedpoint of the antenna. Values for charges on wire segments and currents between wire segments of the model are then computed. Circumferential variation of charge over each wire segment is neglected by assuming the wire diameter to be thin (such as a filament). Thus current is only directed along the wire axis and the circumferential component is zero. The voltage and computed current at the feedpoint segment determine the complex driving point impedance or input impedance of the MAV antenna.

Individual wires of the surface model are broken into smaller segments. The entire model consists of segments of wires, some of which are connected to their nearest neighbor on the same wire, and others connected to the segments of other wires. The proper selection

of length, thickness and interconnection between wire segments determines whether the solution is converged and the simulation produces accurate results.

2. Modeling Rules

Wire frame models for NEC modeling of a structure must be developed with care in order to provide accurate simulations. Parameters that are important and can vary with frequency are wire segment length and diameter. Also important are how wire segments are interconnected and the spacing of meshed wire segments when modeling a surface area. The following paragraphs provide information on how these rules are determined. Table 5 provides a summary of these modeling rules for GNEC[®].

a. Wire Segment Length (Δ)

GNEC[®] provides greater accuracy as shorter and more numerous thin wire segments are used to model the structure. However, complexity and computation time greatly increase with the number of segments, and therefore, guidelines have been developed that provide solution convergence with the minimum number of segments. The fundamental guideline for wire segment length is that

$$\Delta < 0.1\lambda , \quad (27)$$

where λ is the wavelength of the simulated electromagnetic source. When impedance information is required or when modeling critical areas of the antenna, a shorter wire segment used is used to increase the rate of solution convergence

$$\Delta < 0.05\lambda . \quad (28)$$

Shorter segment lengths may not produce greater accuracy if the length to radius ratio becomes too small. Therefore, lengths should not be any shorter than 2.5 times the wire

radius (a) in order for the segment to be considered a thin wire with negligible circumferential current variation.

b. Wire Segment Radius (a)

Wire segment radius (a) selection is dependent upon three factors: (1) thin wire approximation, (2) segment length to radius ratio $\left(\frac{\Delta}{a}\right)$, and (3) the equal area rule for modeling surface area. Circumferential variation of charge over each segment is neglected by assuming that the wire radius is thin relative to wavelength of the electromagnetic signal and much smaller than the segment length. A guideline provided by Burke [Ref 19] for wire segment radius is

$$\frac{2\pi a}{\lambda} \ll 1 \quad . \quad (29)$$

As noted earlier, segment lengths should be greater than 2.5 times the wire radius to neglect the circumferential variation of currents on the wire segment. Therefore the guideline for segment length to radius ratio is

$$\frac{\Delta}{a} \geq 2.5 \quad . \quad (30)$$

The equal area rule for wire segment radius is used when wires are representing a solid surface area. A surface area is modeled with a wire mesh where segment radius and length are chosen such that the wire surface area equals the area to be represented by the wire or equivalently,

$$Area = \sum_{i=1}^n \Delta_i \pi a_i \quad . \quad (31)$$

Since many of the wires in a mesh model will typically represent a metal surface area, the choice of segment radius requires careful consideration of neighboring wires and geometry of the structure. Some mesh formations use converging wires such as spokes in a wheel arrangement. When wires do converge, a tapered wire segment can be used to achieve a better model. Burke [Ref 19] suggests a mesh size smaller than 0.1λ on a side with wire separation of at least 3 times the wire diameter.

c. Interconnection between Surface Mesh Wires

The GNEC[®] program will recognize that wires are connected only when the segment ends coincide. If segment ends do not coincide within 0.001 times the shortest segment length, then GNEC[®] will compute currents on the wire segments as though they are not connected. Therefore, one must use caution to ensure that segments in the wire mesh align at the wire segment ends.

Model Rule	Parameter	Guideline	Comment
1	Segment Length (Δ)	$2.5a < \Delta \leq 0.05\lambda$	Longer lengths reduce computation time
2	Segment Radius (a)	$a \leq \frac{0.1\lambda}{2\pi}$	GNEC [®] uses an approximation that neglects circumferential currents on wire segments. This assumption becomes invalid for larger radius.
3a 3b	Surface Area Modeling	$Area = \sum_{i=1}^n \pi a_i \Delta_i$ or $2\pi a = d$	First equation is most accurate, however, the second equation has proven to be sufficient for surface areas away from discontinuities.
4	Wire Grid Spacing (d)	$6a < d < 0.1\lambda$	Grid spacing should be tighter near antenna feed and discontinuities
5	Wire Interconnections	Segment Ends must coincide within 0.001Δ	When possible identical coordinates for endpoints should be used.

Table 5. GNEC[®] Model Parameter Guidelines.

3. MAV Antenna GNEC[®] Input Data File Development

GNEC[®] input data files describing the geometry of proposed MAV antennas were developed using the guidelines previously described. Table 6 lists the range of values for segment length and radius to meet the NEC modeling requirements listed in Table 5. Table 6 values assume a 1.3 GHz as the source operating frequency, which requires tighter modeling specifications than the 1.0 GHz signal.

Geometry Variable	Value	Model Rule (from Table 5)
Grid Spacing	$d \leq 11 \text{ mm}$	4
Segment Length	$\Delta \leq 11 \text{ mm}$	1
Segment Radius for Surface Modeling (equal area rule)	$a = 1.7 \text{ mm}$ for $d = 11 \text{ mm}$	3b
Segment Radius for Non-Surface Modeling	$a \leq 1.7 \text{ mm}$	2

Table 6. Acceptable Ranges for GNEC[®]/NEC 4.1 MAV Geometry Definitions.

A baseline GNEC[®] model of the MAV antenna was generated and then adjustments were made to the position and size of the feed gap to optimize VSWR. Since the model is symmetrical about the vertical centerline, the model was sectioned into wedges which allows for a simplified GNEC[®] file description. The GNEC[®] input file includes a statement (GM card) to copy and rotate the defined section about the vertical centerline. A sample wire frame model with the wedge section is shown in Figure 40. Each wedge of the simplified GNEC[®] model consists of wires defined to meet the modeling ranges specified in Table 6. Some wires are defined as straight lines and others as arcs. Table 7 lists the model's segment length and radius for the wires in the wedge.

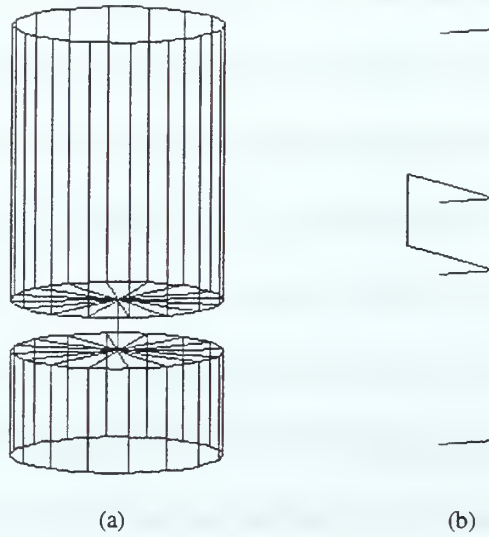


Figure 40. MAV Antenna Model for GNEC[®] Simulations.
(a) Wire Frame Model. (b) Wedge Section.

Wedge Wire	Wire Representation Description	Segment Length (mm)	Segment Radius (mm)
1	Top Gap Plate	7.3	0.01
2	Top Cylinder Wall	4.2	0.1375
3	Top Cylinder Arc	8.4	0.1375
4	Top Gap Arc	8.4	0.1375
6	Bottom Gap Plate	7.3	0.01
7	Bottom Cylinder Wall	8.4	0.1375
8	Bottom Cylinder Arc	8.4	0.1375
9	Bottom Gap Arc	8.4	0.1375
10	Feed/Source	5.0	0.01

Table 7. GNEC[®] Model Wire Segment Definition.

4. GNEC[®] Model Convergence

GNEC[®] impedance calculations were conducted using a single MAV antenna geometry to determine impedance solution convergence of the GNEC[®] model. These calculations were conducted to verify that sufficient detail was present in the GEC[®] model to produce a stable impedance solution. The MAV antenna geometry used had a feed gap of 1.5 cm located at 42 percent from the lower end of the antenna.

Several GNEC[®] models were produced for this antenna geometry with the level of detail adjusted and the calculated impedance observed. If the calculated impedance change between models with increasing levels of detail was small (less than 5 percent), then the level of detail in the model was considered sufficient. Two principal areas of detail for the MAV antenna model are discussed, (1): the applied voltage source area modeling, and (2): circumferential wires for upper and lower surface sections.

a. Applied Voltage Source Area Modeling

According to Burke [Ref 18 and 19], the most critical area of the GNEC[®] antenna model is the modeling of the voltage source, which means the positioning and modeling of the immediate area around the source for the antenna. The GNEC[®] modeling source used was an applied voltage source located at the midpoint of the wire joining the upper and lower sections of the MAV antenna (wire 10 of Table 7). Because a three term basis function (26) is used in the current solution, a minimum of three wire segments are required to be adjacent, in line, and without additional wire junctions. As displayed in Figure 41, the calculated impedance for this wire using 3, 5, and 9 segments has almost negligible change (less than 2 percent). Since calculated impedance changed little for increased number of segments, GNEC[®] models can use a 3 segment wire

between the upper and lower sections with the voltage source applied to the center segments and obtain impedance solution convergence at 1.0 and 1.3 GHz.

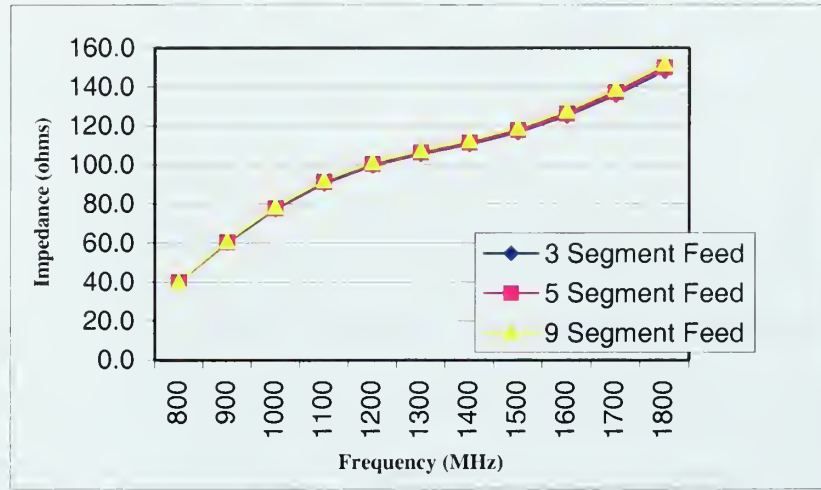


Figure 41. MAV Antenna Impedance for GNEC® Models with 3, 5 and 9 Segments for the Source Wire Model.

b. Circumferential Wires for Upper and Lower Surface Sections

GNEC® modeling requirements for a surface structure require a mesh grid according to the rules presented in Table 5. A GNEC® model with a complete surface mesh is shown in Figure 42. It was suspected that the circumferential wires on the upper and lower surface sections may be removed from the model without effecting impedance calculations if there is no current on them.. Removal of these circumferential wires would greatly reduce the number of segments in the GNEC® model thereby allowing faster computation of antenna impedance. GNEC® models with and without circumferential wires were developed. These models are shown in Figure 42 and Figure 43 with the currents superimposed. As shown, the circumferential currents are observed in Figure 42 to be nearly zero. Also Figure 42 and Figure 43 show that the currents for the simplified model with circumferential wires removed are roughly of the same



magnitude as that of the detailed model. A plot of the 'GNEC[®] calculated input impedance for the detailed and simplified models is shown in Figure 44. These results demonstrate that the calculated impedance does not change much between these models. Therefore, removal of the circumferential wires from the model can be done without effecting the calculated antenna impedance solution.

As shown in Figure 42 and Figure 43, the model of the MAV antenna is shown symmetric about a vertical centerline. Fabrication of a physical MAV antenna with absolute symmetry about the vertical centerline is highly unlikely. An offset of the source wire from the centerline will likely result in an increase in currents in the circumferential direction. Therefore, some caution should be observed when interpreting between the measured and calculated impedance for the MAV antenna.

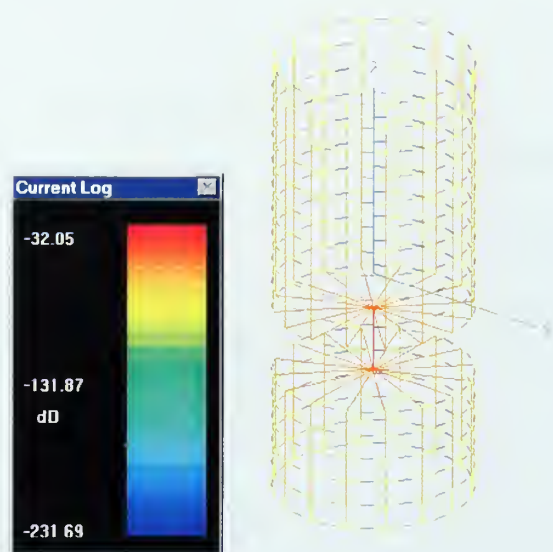


Figure 42. Currents for the Detailed GNEC[®] model of a MAV Antenna.

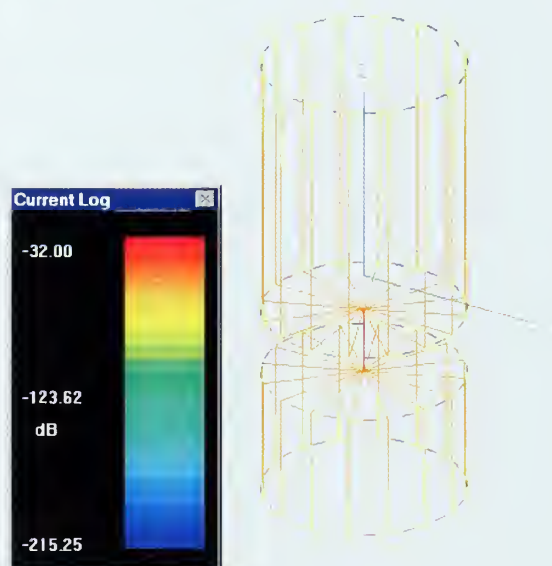


Figure 43. Currents for the Simplified GNEC[®] Model of the MAV Antenna.

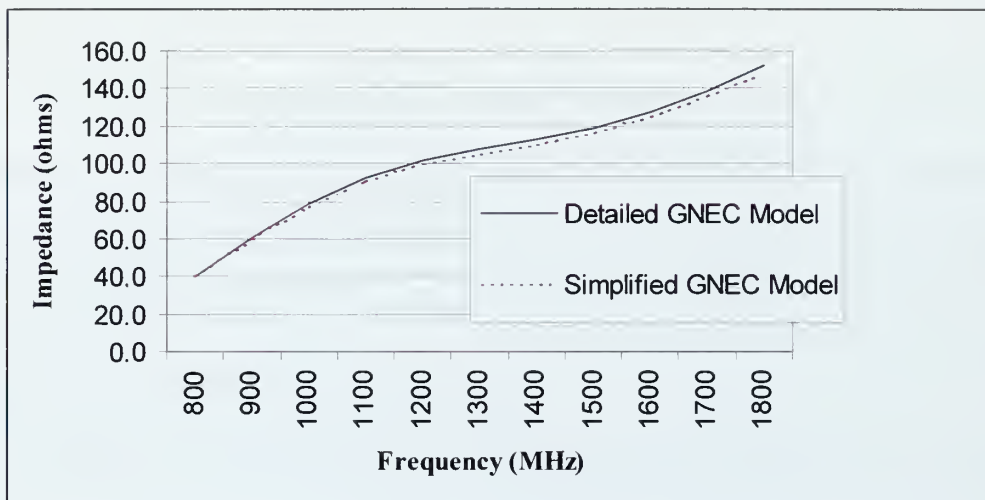


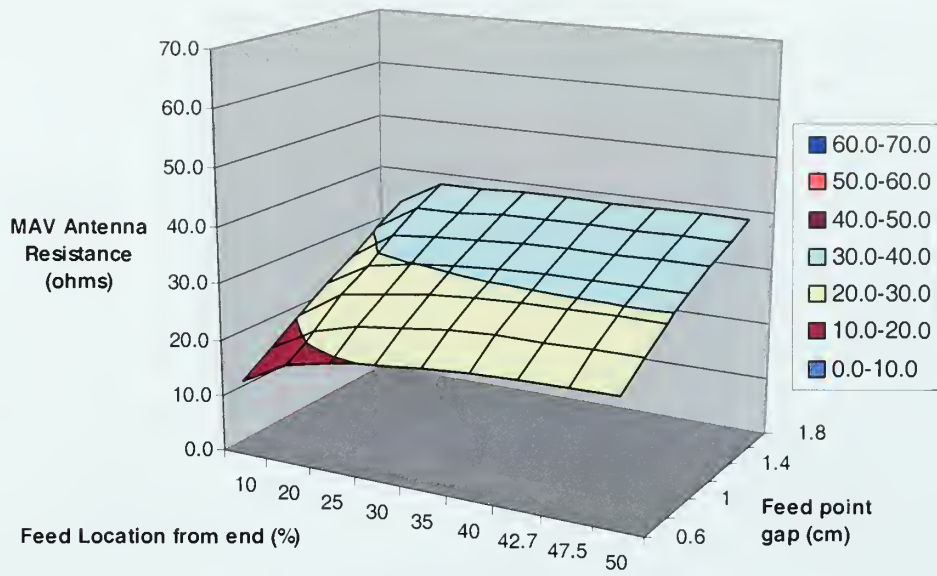
Figure 44. The Calculated Impedance of MAV Antenna for Detailed and Simplified GNEC[®] Models.

D. GNEC[®] SIMULATIONS TO DESIGN ANTENNA FEED

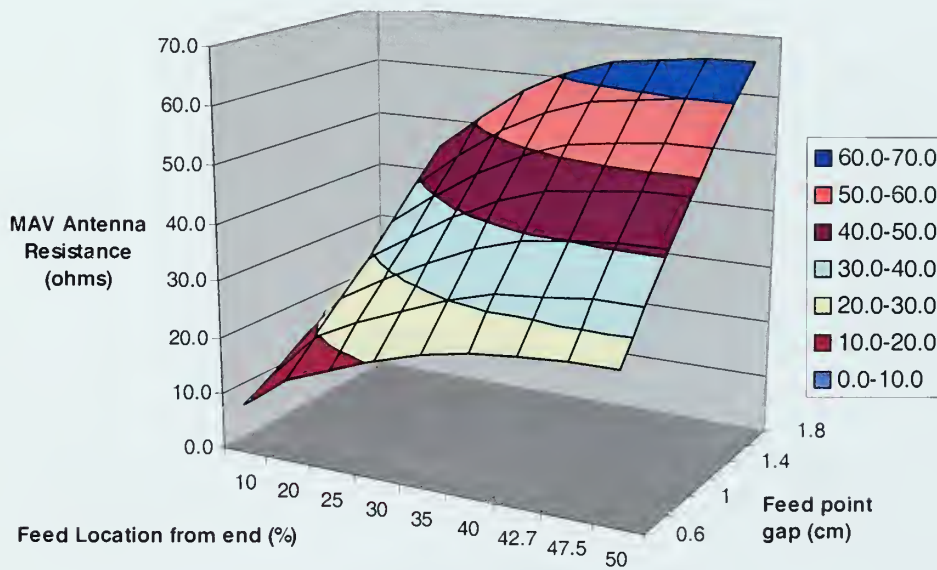
The objective of the GNEC[®] computer simulations was to obtain an antenna configuration with a driving point impedance close to that of the 50 ohm transmission line. Since the overall length, thickness and shape had to match the Lutronix vehicle, the parameters that could be adjusted were the position of the feed and size of the gap between upper and lower sections of the dipole antenna.

GNEC[®] computer simulations of 58 separate antenna designs were conducted to determine the best feed point positioning and gap size in order to provide an antenna with close to a 50 ohm driving point impedance. These designs used the Lutronix MAV size and then adjusted the feedpoint position from 50% from one end (i.e., center fed) to 10% from one end. At each location, the feed gap was varied from 0.6 cm to 1.8 cm and input impedance calculated.

Simulation results yield the complex input impedance of the MRPV antenna for the two principal frequencies of interest (1.0 GHz and 1.3 GHz). Surface plots were made of antenna input resistance, reactance and impedance as a function of feed location and feed gap size. Figure 45 displays the GNEC[®] calculated resistance values, Figure 46 the calculated reactance values and Figure 47 the GNEC[®] calculated impedance magnitude values. Each figure has separate plots for the 1.0 GHz and 1.3 GHz test frequencies. Table 8 and Table 9 provide the reactance and impedance magnitude in tabular form. A 50 ohm impedance is desired with minimum reactance, therefore an impedance tolerance of 45 to 55 ohms was selected and the smallest reactance determined. The optimum feed gap designs are shown shaded in Table 8 and Table 9. The recommended antenna design is then provided in Table 10.

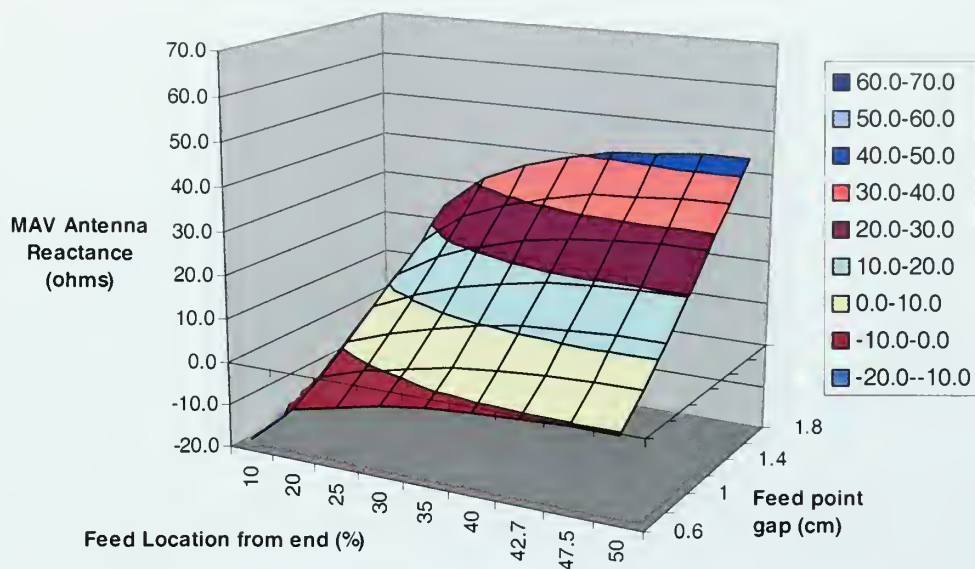


(a) $f = 1.0$ GHz

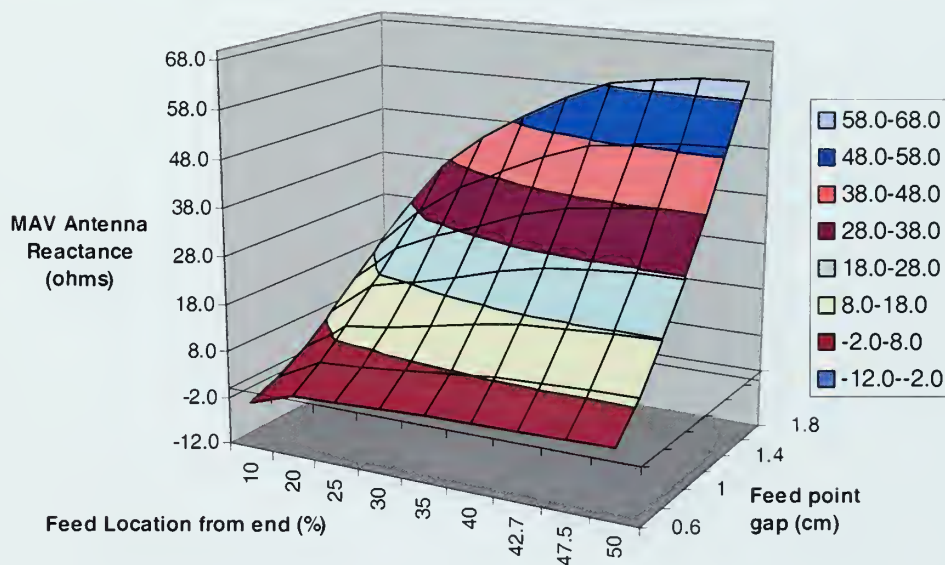


(b) $f = 1.3$ GHz

Figure 45. MAV Antenna Resistance versus Feed Gap Size and Location
Computed using GNEC[®]. (a) 1.0 GHz. (b) 1.3 GHz.

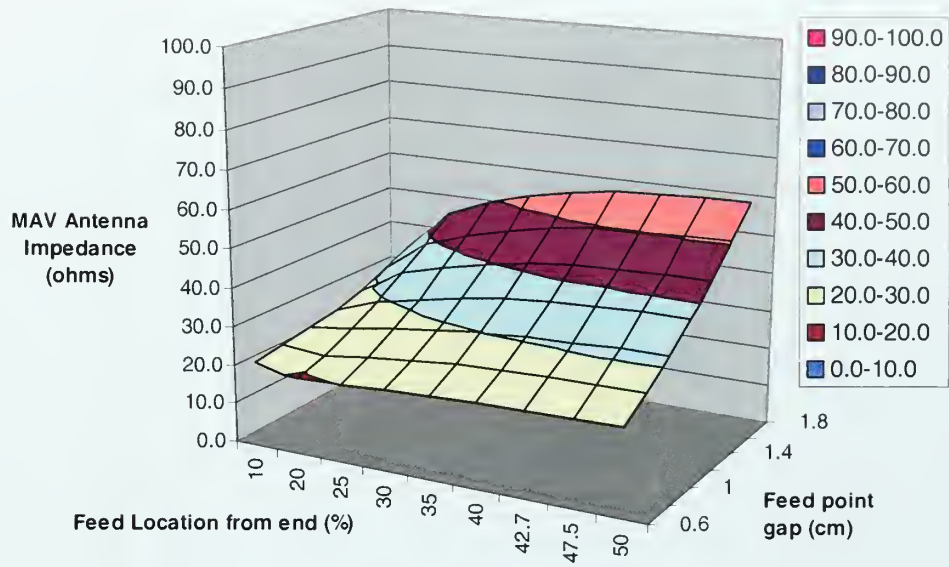


(a) $f=1.0$ GHz

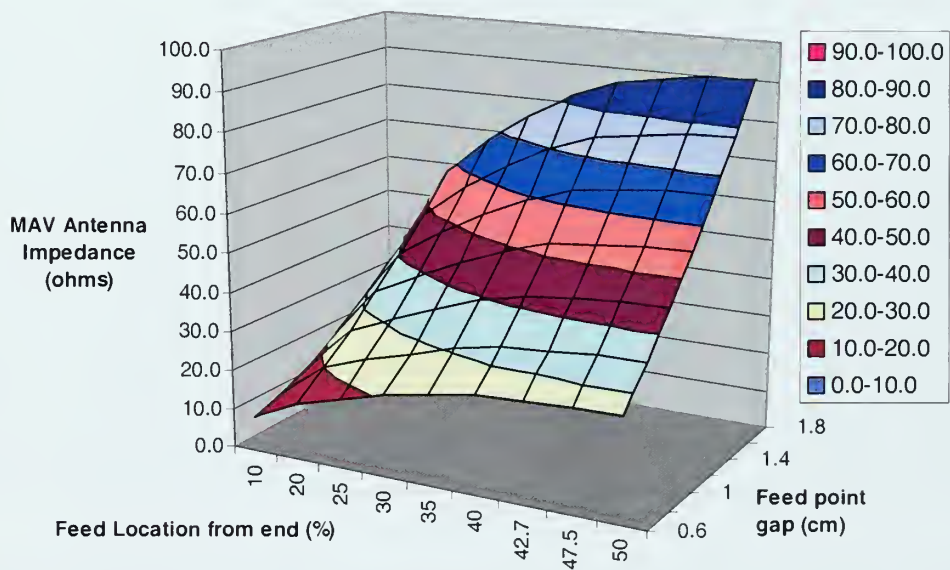


(b) $f=1.3$ GHz

Figure 46. MAV Antenna Reactance versus Feed Gap Size and Location Computed using GNEC[®]. (a) 1.0 GHz. (b) 1.3 GHz.



(a) $f = 1.0$ GHz



(b) $f = 1.3$ GHz

Figure 47. MAV Antenna Impedance versus Feed Gap Size and Location
Computed using GNEC[®]. (a) 1.0 GHz. (b) 1.3 GHz.

1.0 GHz Input Reactance (ohms)

Gap Position (%)	Gap Size (cm)						
	0.6	0.8	1.0	1.2	1.4	1.6	1.8
10	-16.9	-15.5	-12.7	-8.3	-4.5	0.1	4.1
20	-8.3	-4.1	0.8	6.3	11.5	16.7	23.5
25	-5.9	-1.0	0.3	10.0	17.2	24.2	31.4
30	-3.9	1.1	7.3	14.0	21.0	28.3	35.8
35	-2.4	3.2	9.6	16.6	23.8	31.4	39.1
40	-1.3	4.5	11.2	18.0	25.8	33.5	41.4
42.7	-0.9	5.0	11.8	19.0	26.5	34.3	42.2
47.5	-0.5	5.5	12.4	19.7	27.3	35.1	43.1
50	-0.4	5.6	12.5	19.8	27.4	35.2	43.2

(a)

1.0 GHz Impedance Magnitude (ohms)

Gap Position (%)	Gap Size (cm)						
	0.6	0.8	1.0	1.2	1.4	1.6	1.8
10	21.5	22.9	24.1	25.3	27.5	30.6	33.8
20	19.4	21.5	25.3	29.3	34.0	38.9	44.6
25	20.1	23.4	27.1	31.7	37.0	42.9	49.3
30	20.8	24.4	28.7	33.7	39.5	45.7	52.5
35	21.4	25.3	29.9	35.3	41.3	47.9	54.8
40	21.8	26.0	30.9	36.4	42.6	49.3	56.4
42.7	22.0	26.2	31.2	36.9	43.1	49.9	57.1
47.5	22.2	26.5	31.7	37.4	43.7	50.6	57.8
50	22.3	26.6	31.7	37.4	43.8	50.6	57.8

(b)

Table 8. GNEC[®] Calculated Reactance and Impedance for 10.2 cm MAV Antenna Operating at 1.0 GHz. (a) Reactance. (b) Impedance Magnitude.

1.3 GHz Input Reactance (ohms)

Gap Position (%)	Gap Size (cm)						
	0.6	0.8	1.0	1.2	1.4	1.6	1.8
10	-2.2	0.3	3.9	9.1	13.9	19.4	24.6
25	0.8	5.0	10.0	16.1	21.9	28.1	36.2
25	1.1	5.0	11.4	18.3	26.1	34.7	43.9
35	1.4	6.4	13.1	20.9	29.6	39.2	49.4
35	1.9	7.6	14.9	23.5	33.1	43.4	54.4
40	2.3	8.5	15.4	25.7	35.9	46.6	58.5
42.7	2.5	8.8	17.1	26.6	37.0	48.2	60.0
47.5	2.6	9.2	17.6	27.3	38.0	49.4	61.4
50	2.6	9.2	17.7	27.4	38.1	49.5	61.6

(a)

1.3 GHz Impedance Magnitude (ohms)

Gap Position (%)	Gap Size (cm)						
	0.6	0.8	1.0	1.2	1.4	1.6	1.8
10	9.0	11.6	15.4	20.3	25.6	31.8	37.9
25	14.5	20.1	26.1	33.2	40.6	48.4	57.5
25	17.7	24.3	31.0	38.9	47.7	57.2	67.4
35	20.7	27.5	35.5	44.3	53.9	64.2	75.2
35	23.1	30.4	39.4	38.9	59.1	70.1	81.7
40	24.9	33.2	42.3	52.3	63.0	74.4	86.4
42.7	25.6	34.1	43.5	53.6	64.5	76.0	88.2
47.5	26.3	35.0	44.6	54.9	65.9	77.6	89.9
50	26.3	35.1	44.7	55.0	66.1	77.8	90.1

(b)

Table 9. GNEC[®] Calculated Reactance and Impedance for 10.2 cm MAV Antenna Operating at 1.3 GHz. (a) Reactance. (b) Impedance Magnitude.

Operating Frequency (GHz)	Feed Gap Position (% from end)	Feed Gap Size (cm)	GNEC [®] Calculated Impedance (ohms)	GNEC [®] Calculated Reactance (ohms)
1.0	25	1.8	49.3	31.4
1.3	35	1.2	48.9	23.5

Table 10. Summary of Feed Gap Parameters for Optimized 10.2 cm MAV Antenna.

E. GNEC[®] ANTENNA RADIATION PATTERN EVALUATION

The GNEC[®] calculated radiation pattern was evaluated for a MAV antenna with overall length of 10.2 cm, the feed point located at 42 percent from bottom, and a feed gap size of 1.5 cm. A vertical slice of the far field radiation pattern is displayed in Figure 48. The GNEC far field radiation pattern for a thin wire dipole of the same overall length is presented in Figure 49 for comparison.

The maximum gain of the MAV antenna does not change much from a thin dipole, as the difference between the two models is only 0.05 dB. The principal difference between the radiation patterns is the location of the maximum gain. The MAV antenna with offset feed has a maximum gain at 77 degrees whereas the thin center fed dipole has maximum gain at 90 degrees. This difference is due to the offset feed of the MAV antenna.

The conclusion is that the MAV antenna radiation pattern will likely be nearly the same as a thin wire dipole. The maximum gain position is slightly offset from horizontal due to the offset feed. The half-power beam-width, although 2 degrees less than the thin wire center fed dipole, is still large enough (80 degrees) to permit the MAV to receive power from many directions.

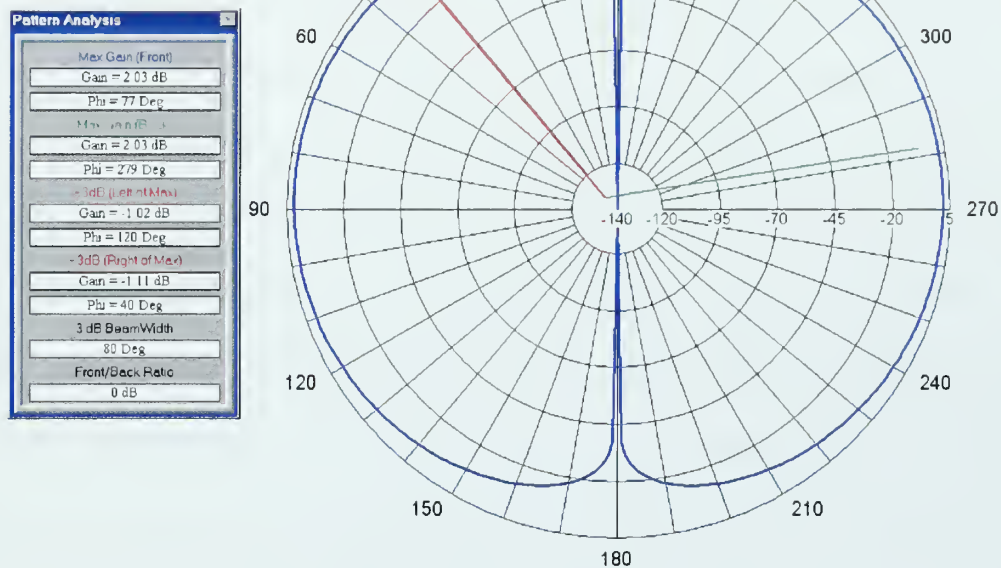


Figure 48. GNEC Calculated Radiation Pattern for MAV-2 Antenna.

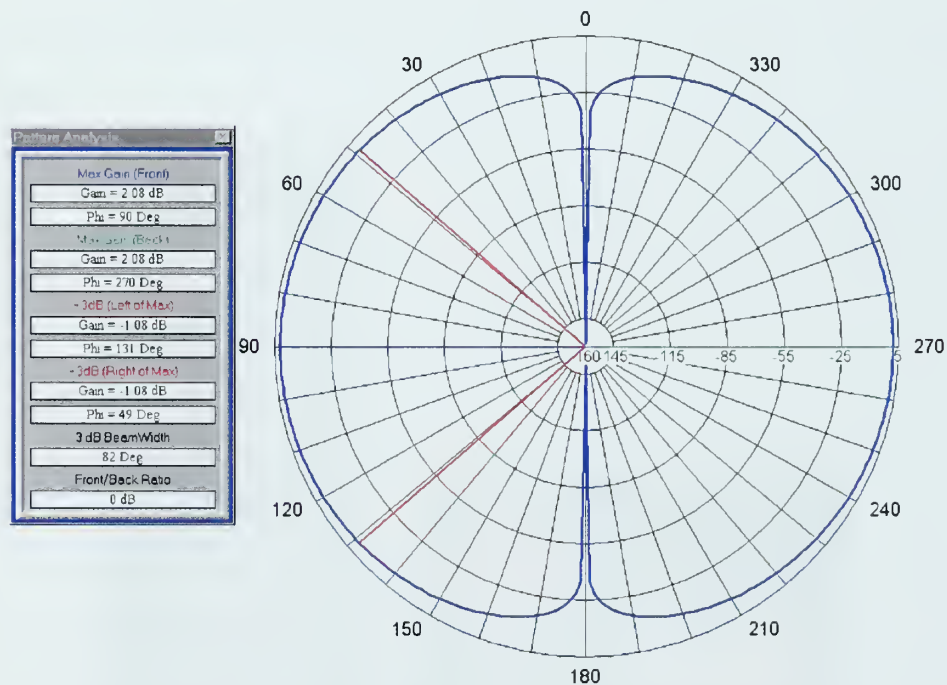


Figure 49. Radiation Pattern for a Thin Dipole of Same Length as MAV Antenna.

F. ANTENNA FABRICATION

This antenna was intended to only demonstrate remote power transmission, and as such would be a non-flying model. Thus model weight was not considered a factor in the choice of materials. An early fabrication attempt used copper foil wrapped about an insulator. This technique proved unreliable and tended to leave conductive gaps along the seams. An improved fabrication technique was devised by using 4.4 cm diameter copper plumbing pipe cut to the desired length on a lathe. Copper endcaps were used as the center feed gap area of the MAV dipole antenna. A slightly smaller diameter pipe section attached the copper pipe (upper section of the antenna) to the upper endcap (upper feedgap). A thick section of mylar was used to hold the upper and lower sections of the MAV antenna together. Figure 50 displays a sample MAV antenna disassembled to illustrate the assembly concept used.



Figure 50. Photographs of Copper Pipe MAV Antenna Disassembled to Show Interior Connections.

This assembly allowed easy access to the interior of the antenna to install circuits. A metal surface discontinuity existed on the upper antenna section between the copper endcap serving as the upper feed gap and the copper pipe serving as the upper section of the antenna. It was thought that this discontinuity would not appreciably effect the antenna's electrical properties since it is very small and is likely to show little resistance at the operating frequencies. The metal surface discontinuity could be eliminated by filling this indentation with an electrically conductive paint or with solder, however, this was not done since access to the interior circuitry was required for troubleshooting and evaluation.

The antenna feed consisted of a 50 ohm semi-rigid coaxial line that served to connect the antenna to the rectifier circuit. The outer shield of the semi-rigid line was soldered to the upper copper endcap and the center conductor was extended across the gap and soldered to the lower copper endcap. The distance between these points is the feed gap and is spanned by the center conductor and dielectric core of the semi-rigid coaxial cable. The semi-rigid coaxial cable was fitted with a male SMA connector, prior to soldering to the copper endcaps. The connector provided a convenient structural and electrical interface for the microstrip rectifier circuit.

Assembly of the feed to the copper antenna required planning and prepositioning techniques. Due to the rapid thermal transfer properties of a large copper area, the copper endcaps required a great deal of heat to make an acceptable solder bond. Also applying the rigid coaxial line when the heat was too great caused the interior dielectric of the semi-rigid coax line to melt. Soldering the semi-rigid line to the endcaps required bringing the copper endcaps up to temperature by the simultaneous application of several soldering irons until solder would bond, then the rigid coaxial line was inserted through the drilled hole allowing

sufficient length to reach the opposite side of the feed. Solder was quickly applied on the interior side of this connection electrically fusing the outer conductor to the upper feedgap of the MAV antenna. The entire assembly was cooled immediately using de-ionized water. The rigid coaxial line across the feed gap was stripped of the outer conductor and cut to the length of the feed gap. The center conductor was attached to a connector pin, which was soldered to the lower copper endcap. The connector pin provided a strain relief to prevent the center conductor from breaking. These techniques were learned through trial and error.

Two antennas were fabricated, one each for the 1.0 GHz and 1.3 GHz operating frequencies. Photographs of these two antennas are shown in Figure 51 with dimensions annotated. The antennas were fabricated prior to completion of GNEC[®] simulations and therefore did not use the GNEC[®] recommended sizing for impedance matching. Rather, the MAV antennas were fabricated using estimated dimensions obtained through VNA measurements of VSWR while varying the feedgap between the upper and lower endcaps of the antenna.

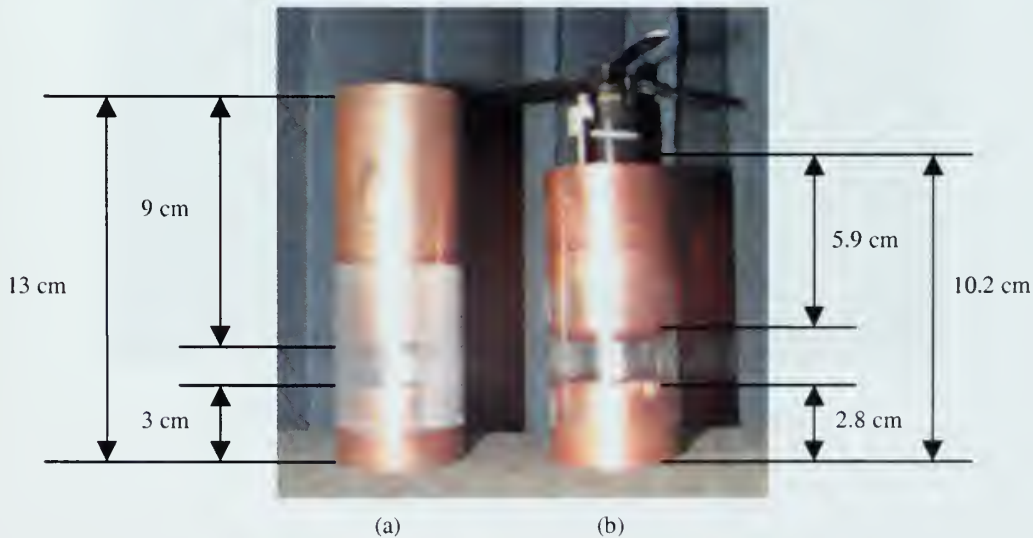


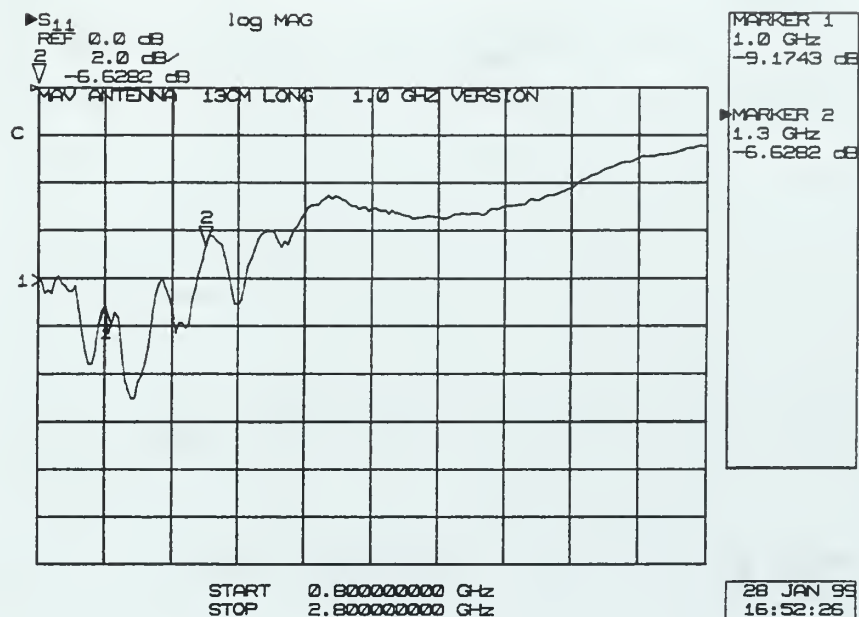
Figure 51. MAV Antennas, Fabricated from 4.4 cm Diameter Copper Pipe.
(a) 1.0 GHz Version (MAV-1). (b) 1.3 GHz Version (MAV-2).

G. ANTENNA INPUT IMPEDANCE MEASUREMENT

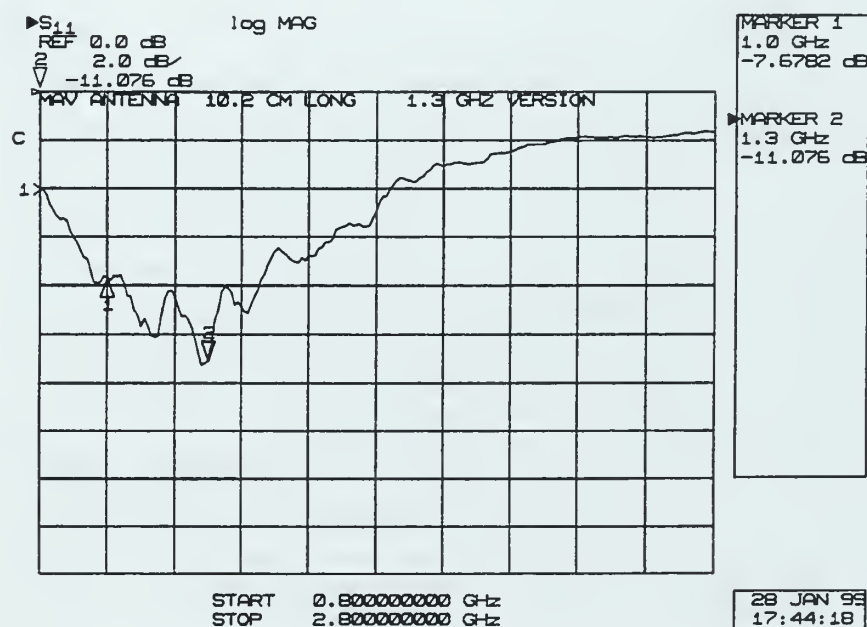
The assembled MAV antennas were connected to the HP8510C Vector Network Analyzer (VNA) as shown in Figure 52. A one port VNA calibration was conducted using calibrated SMA loads. This calibration included the flexible coaxial cable interfacing the VNA to the connector of the antenna. This calibration effectively subtracts out the effects of the VNA and interfacing cabling so that the corrected measurement is very close to that of the isolated device under test (DUT). Measurements of return loss, VSWR and input impedance were made over the range 0.8 to 2.8 GHz for the two antennas fabricated. The return loss for the two antennas is shown in Figure 53, VSWR in Figure 54 and input impedance in Figure 55.



Figure 52. VNA Measurements on MAV Antenna.



(a)

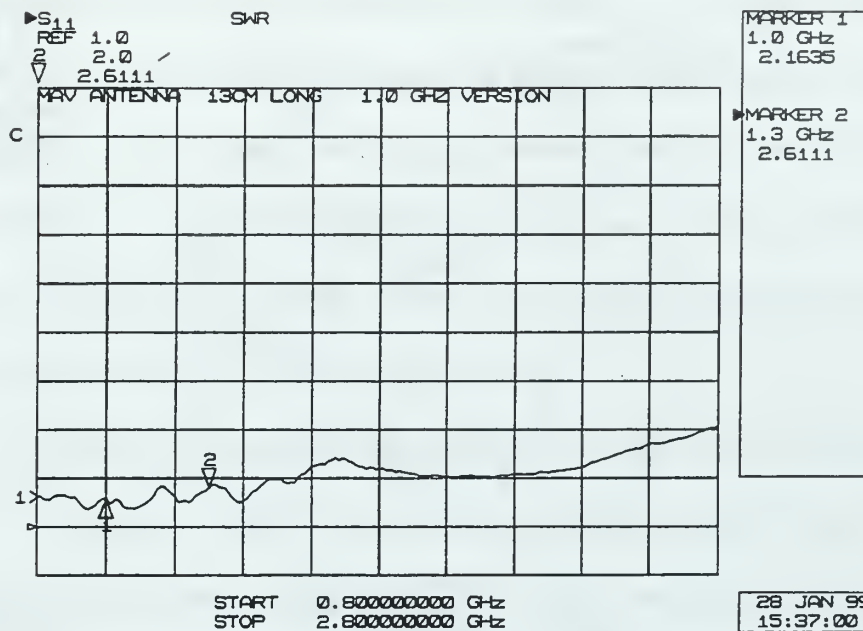


(b)

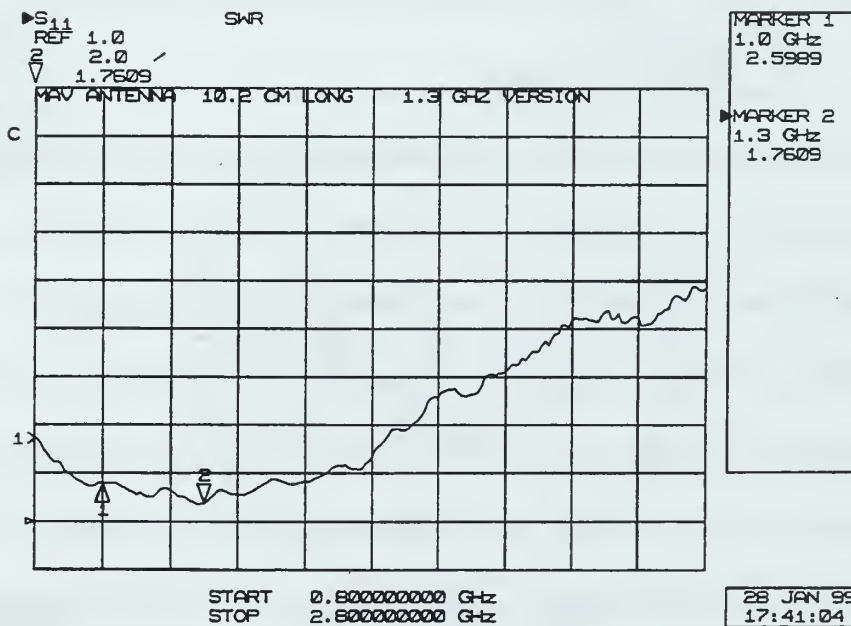
Figure 53. HP8510 VNA Measurement of Return Loss for MAV Antennas.

(a) 1.0 GHz Version; Length 13 cm (MAV-1).

(b) 1.3 GHz Version; Length 10.2 cm (MAV-2).



(a)



(b)

Figure 54. HP8510 VNA Measurement of VSWR for MAV Antennas.

(a) 1.0 GHz Version, Length 13 cm (MAV-1).

(b) 1.3 GHz Version, Length 10.2 cm (MAV-2).

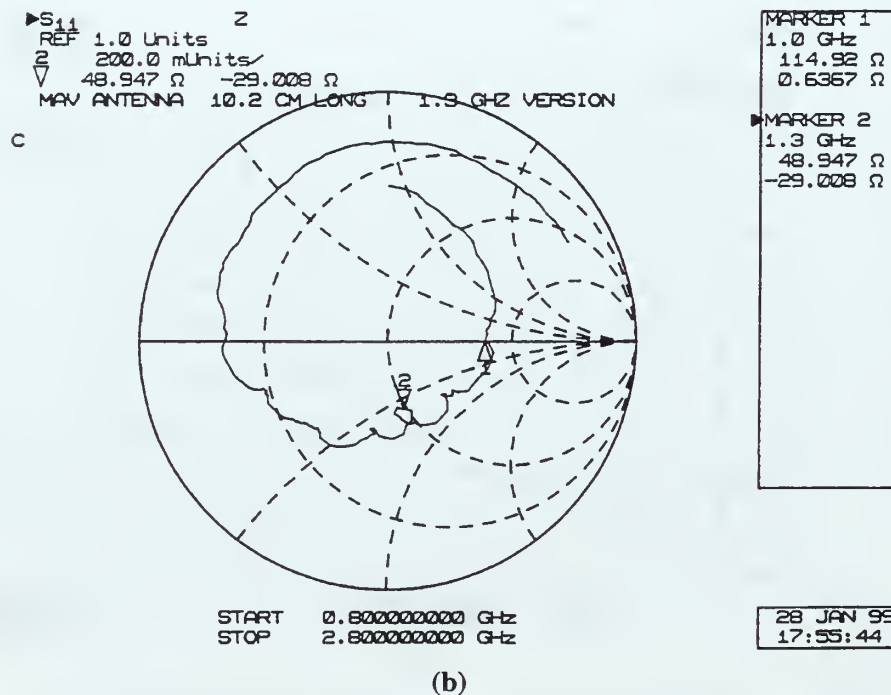
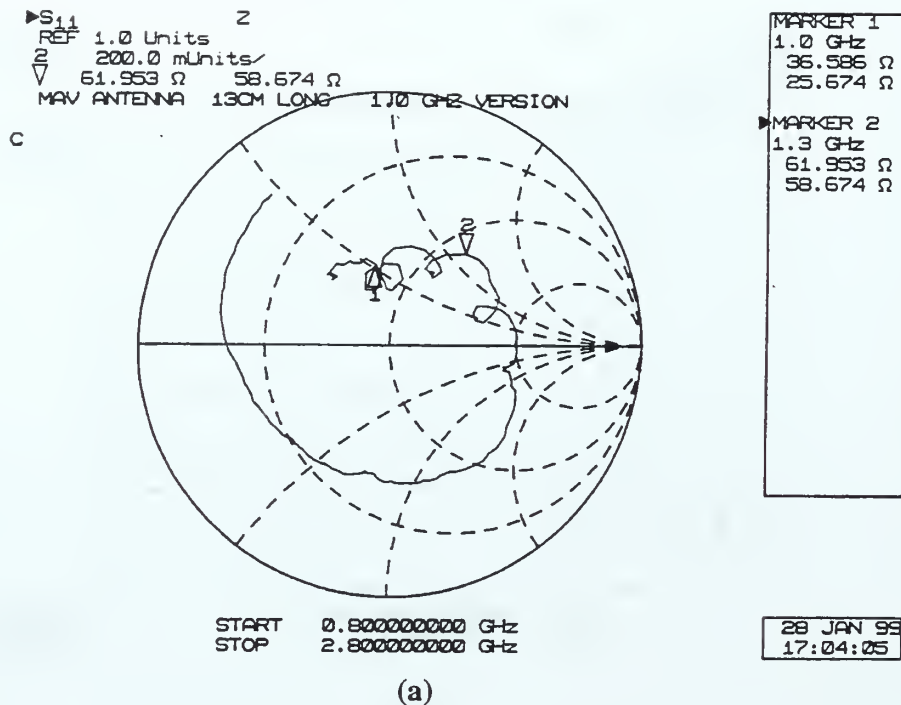


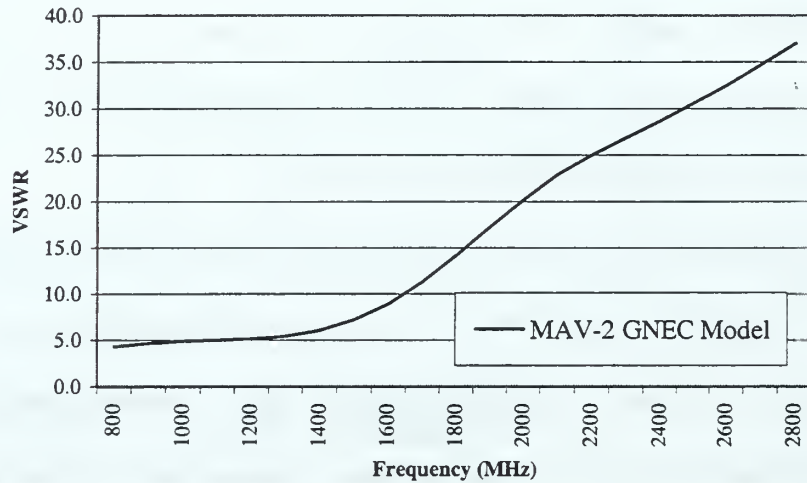
Figure 55. HP8510 VNA Measurement of MAV Antenna Impedance.
 (a) 1.0 GHz Version (MAV-1). (b) 1.3 GHz Version (MAV-2).

VNA measurements of the as-built MAV antennas show that the characteristics, although not optimum, were sufficient for the WPT application. Both antennas exhibited a return loss of close to 10 dB at their operating frequencies. The return loss and the VSWR of these antennas were assumed to be sufficient to continue their use in developing the wireless powered demonstrator models. Future work should investigate building MAV antennas using the dimensions recommended in Table 10.

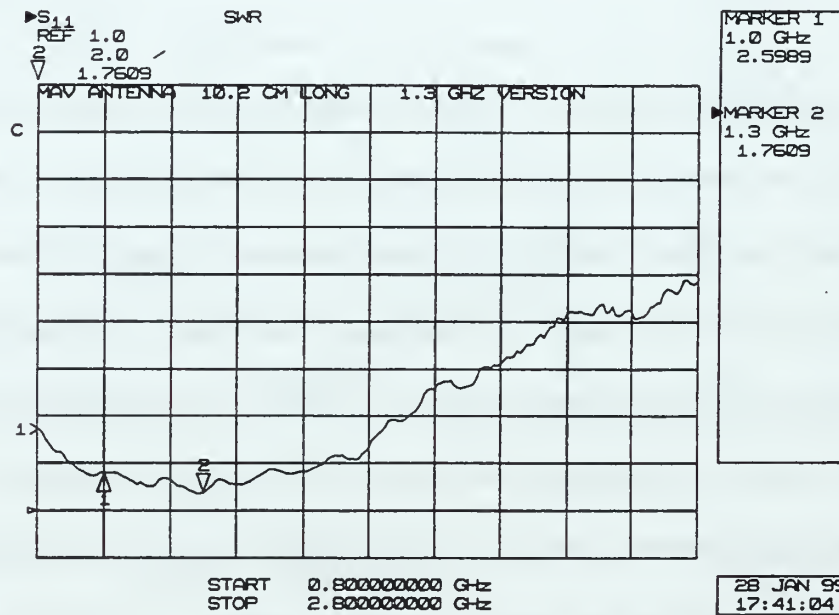
The VNA measurements of these antennas were affected by near field objects such as hands and test equipment and therefore the results would sometimes vary. The data shown in Figure 53 to Figure 55 were made with the MAV antenna situated on top of 4 inches of electromagnetic anechoic absorber foam. Measurements in this configuration tended to be more consistent than when the antenna was situated directly on top of a metal bench.

Figure 56 provides a comparison between the GNEC model of the MAV-2 antenna and VNA measurements on the as-built antenna. The overall trend of VSWR shown in both plots tends to increase as frequency increases, however the rate of increase displayed by the GNEC results is much higher. It is likely that as the frequency increases, the GNEC model used becomes less accurate and perhaps even incorrect. The reason for this claim is that the GNEC model segment length has not decreased in relation to the increase in frequency. As frequency increases above the values for which segment length and radius were developed, the GNEC model diverges from the measured solution. The VNA measurements also display much smaller values at the frequencies of interest than the GNEC calculations. The as built MAV antenna contained a short length of 50 ohm rigid coaxial line that was not included in the GNEC calculations and is not calibrated out in the VNA measurements. It

may be possible that this section of coaxial line may have helped provide a closer match to 50 ohms due to the reference plane shift introduced by the coaxial cable.



(a)



(b)

Figure 56 Comparison of VSWR Calculated by GNEC and that Measured by VNA for the 1.3 GHz MAV Antenna (MAV-2). (a) GNEC Calculation. (b) VNA Measurement.

H. ANTENNA DEVELOPMENT CONCLUSIONS

MAV antenna design using GNEC as a tool was useful, however some caution when reviewing calculated results is required. Some parameters and effects on the MAV antenna impedance can not be easily modeled in GNEC. These parameters include the actual feed for the antenna, which is a semi-rigid coaxial cable, and the potential for an off center feed wire to change the current patterns on the MAV structure. However the GNEC model does provide an idea of how the feed gap location and size effects the impedance of the MAV antenna.

Based upon the GNEC impedance calculations, a 10.2 cm long MAV antenna for the 1.3 GHz operating frequency should have a 1.2 cm gap located 35 percent from the bottom end. The as-built MAV antenna had a 1.5 cm gap located 42 percent from the bottom. The GNEC impedance calculations indicated that the as-built antenna would have impedance that is higher than the desired 50 ohms and the VNA measurements support this result.

It is interesting to note how feed gap size effected the impedance of the antenna. Consider the feed gap as a parallel plate capacitor with capacitance

$$C = \frac{\pi a^2}{d} \epsilon_0 , \quad (32)$$

where a is the radius of the antenna, d is the gap spacing and ϵ_0 is the free space permittivity. Then from (32), one would expect the antenna reactance to become more capacitive as the gap size is made smaller. Indeed as displayed in Figure 46, as gap size decreases, the reactance decreases from positive values. This seems to indicate that the gap

IV. RECTIFIER CONVERSION EFFICIENCY MEASUREMENTS

A. INTRODUCTION

This chapter presents the rectifier RF-to-DC conversion efficiency testing that was conducted on several microstrip rectifier designs and explains the techniques used to measure rectifier conversion efficiency. Rectifier conversion efficiency has been the chief measure of the performance of microwave rectification circuits. This conversion efficiency has been defined many different ways by various researchers. Some of these conversion efficiencies are more applicable to entire transmission system and include effects such as transmitter losses and antenna efficiencies. This thesis is interested in maximizing the efficiency of the rectifier circuitry and, in that regard, the efficiency measurements defined for this work deal with the rectifier circuit only and disregard the loss contributions of the transmitter, transmission path and antenna.

In this thesis, the rectifier conversion efficiency is defined as the ratio of average DC power measured at the output of the microstrip rectifier circuit to the average incident microwave power measured at the input to the microstrip rectifier circuit or

$$\text{Percent Efficiency} = \frac{P_{DC}}{P_{RF}} \cdot 100 , \quad (33)$$

where P_{DC} is the average DC power measured at the output of the microwave rectifier circuit and P_{RF} is the microwave power into the rectifier circuit. P_{RF} is the difference between incident and reflected microwave power measured at the input of the rectifier circuit. Critical to the accuracy of this experiment are measurement of output DC power (P_{DC}), incident microwave power ($P_{incident}$), and reflected microwave power ($P_{reflected}$).

Average DC power (P_{DC}) at the output of the rectifier was obtained using digital multi-meter measurements of voltage across a lumped element load or voltage across and current through a miniature DC motor load. The input microwave power values were obtained by coupling a sample of incident microwave power via a directional coupler, and measuring the sampled microwave power using a thermocouple sensor based microwave power measurement system (specifically the Hewlett Packard HP438A dual channel power meter with two HP8481A thermocouple power sensors).

Rectifier efficiency measurements were conducted using single frequency or continuous wavelength (CW) and pulse modulated CW microwave signals. The CW and pulse modulated CW signals were at 1.0 and 1.3 GHz. Pulse width and repetition rate (prf) for pulse modulated CW signals were varied to determine effects upon rectification efficiency.

Efficiency measurements were also made with several types of loads. These loads included lumped element surface mount (chip) resistors, parallel resistive-capacitive (RC) lumped element loads and miniature permanent magnet DC motors. It will be shown that circuit loading influenced the efficiency of the rectifier circuit.

Section B of this chapter discusses how these measurements were made. Section C presents the measurements in graphical form, while Section D provides a summary of the results. Section E suggests some microwave rectifier improvements based on the results of the efficiency measurements.

B. CONVERSION EFFICIENCY MEASUREMENT DESCRIPTION

A block diagram of a RF-to-DC conversion efficiency measurement apparatus for single frequency or CW input signal with a resistive load is shown in Figure 57.

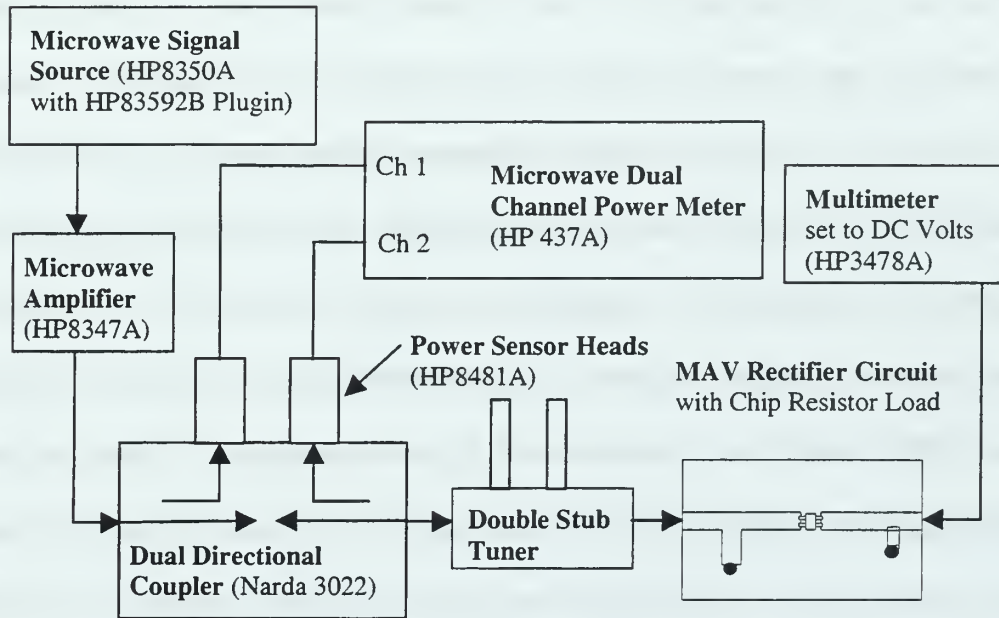


Figure 57. Block Diagram of RF-to-DC Conversion Efficiency Measurement CW Input Signal and Chip Resistor Loading.

A thermocouple power sensor (HP8481A) connected to channel 1 of the digital power meter (HP438A) measured the incident microwave CW signal at a frequency of 1.0 GHz or 1.3 GHz. Reflected microwave power from the MAV rectifier circuit was measured on channel 2 of the power meter. An adjustable external double short circuit stub tuner is used to impedance match the MAV rectifier circuit to the signal source circuit, which had a characteristic impedance of 50 ohms. The tuner is adjusted by varying the length of two parallel short circuits to achieve minimum reflected power as measured by channel 2 of the power meter. DC output power from the rectifier circuit is obtained by measuring the

average voltage across the chip resistor load. Amplifier gain settings were varied to obtain incident microwave power from 0 mw to 180 mw.

When the input power was pulsed, as when simulating a radar transmitter as the power source, or when the load is not a simple resistive load, the conversion efficiency measurement apparatus was modified. Figure 58 shows the measurement setup for a pulsed CW incident power signal and Figure 59 the measurement setup for a miniature DC motor load using the pulsed CW incident power signal. The measurement apparatus used in Figure 58 and Figure 59 provided incident average power levels up to 700 mw for CW signals, which were much larger than the power levels for the test apparatus of Figure 57.

The measurement configurations in Figure 58 and Figure 59 have two differences: (1) the loading of the MAV rectifier circuit, and (2) the manner in which the applied DC power is measured. These configurations used a radar target simulator to build a pulse of width (τ) and repetition frequency (f_p) that was used to modulate the 1.0 GHz or 1.3 GHz CW microwave signal. The Tektronix 477 analog oscilloscope provided a trigger pulse (B gate trigger) that set the pulse repetition frequency (prf) which was displayed on the HP5248 electronic counter. The radar target simulator set the pulse width at 7 μ s, similar to the waveform of the transmitter of the AN/SPS-58 air search radar.

The pulsed output from the radar target simulator modulated the CW signal from the HP8614A signal generator and was amplified by the HP489A microwave traveling wave tube (TWT) amplifier. An isolator was used on the output of the TWT to protect the amplifier from potential reflections of power from the test circuitry. A tiny sample, 30 dB lower than the pulse modulated microwave signal, was coupled by the Narda 3002-30

directional coupler and detected using the HP432A detector. The envelope of the pulse-modulated signal was displayed on the Tektronix 446 analog oscilloscope.

The incident and reflected microwave power was measured using the HP8481A thermocouple power sensor heads and HP438A dual channel digital power meter. A Tektronix 11801A high-speed digital sampling oscilloscope was used to observe the pulse modulated CW microwave signal incident on the MAV microstrip rectifier circuit and the rectified output of the MAV. The high-speed sampling oscilloscope provided insight to the time domain characteristics of the rectifier output signal. DC power provided by the MAV rectifier circuit was determined by measuring the average voltage across the chip resistor load using a HP3578A digital multimeter. When the load was a miniature DC motor, the resultant DC power was determined by measuring the current through and voltage across the motor using two HP3478A multimeters as shown in Figure 59.

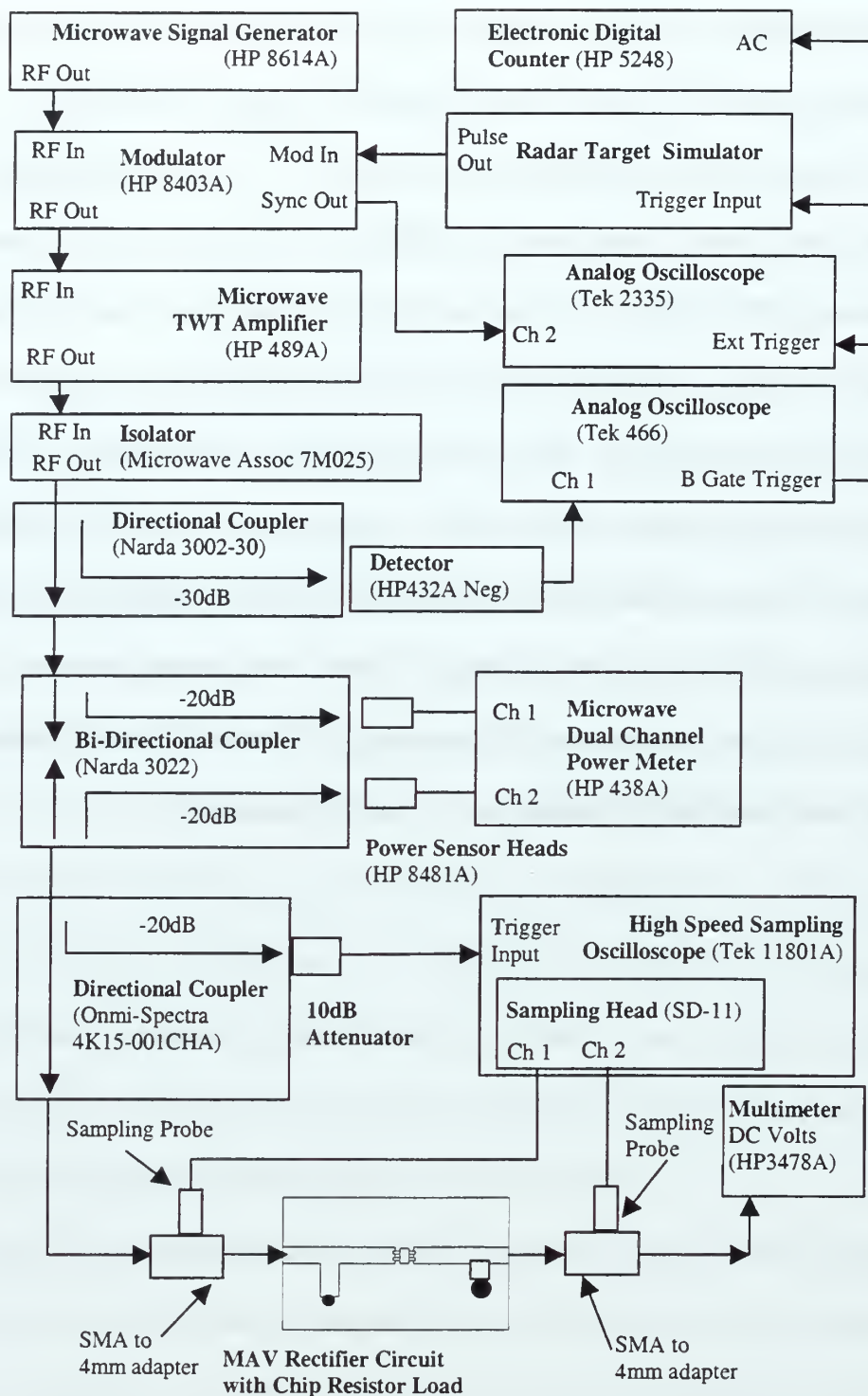


Figure 58. Block Diagram of RF-to-DC Conversion Efficiency Measurement, Pulsed CW Input Signal and Chip Resistor Loading.

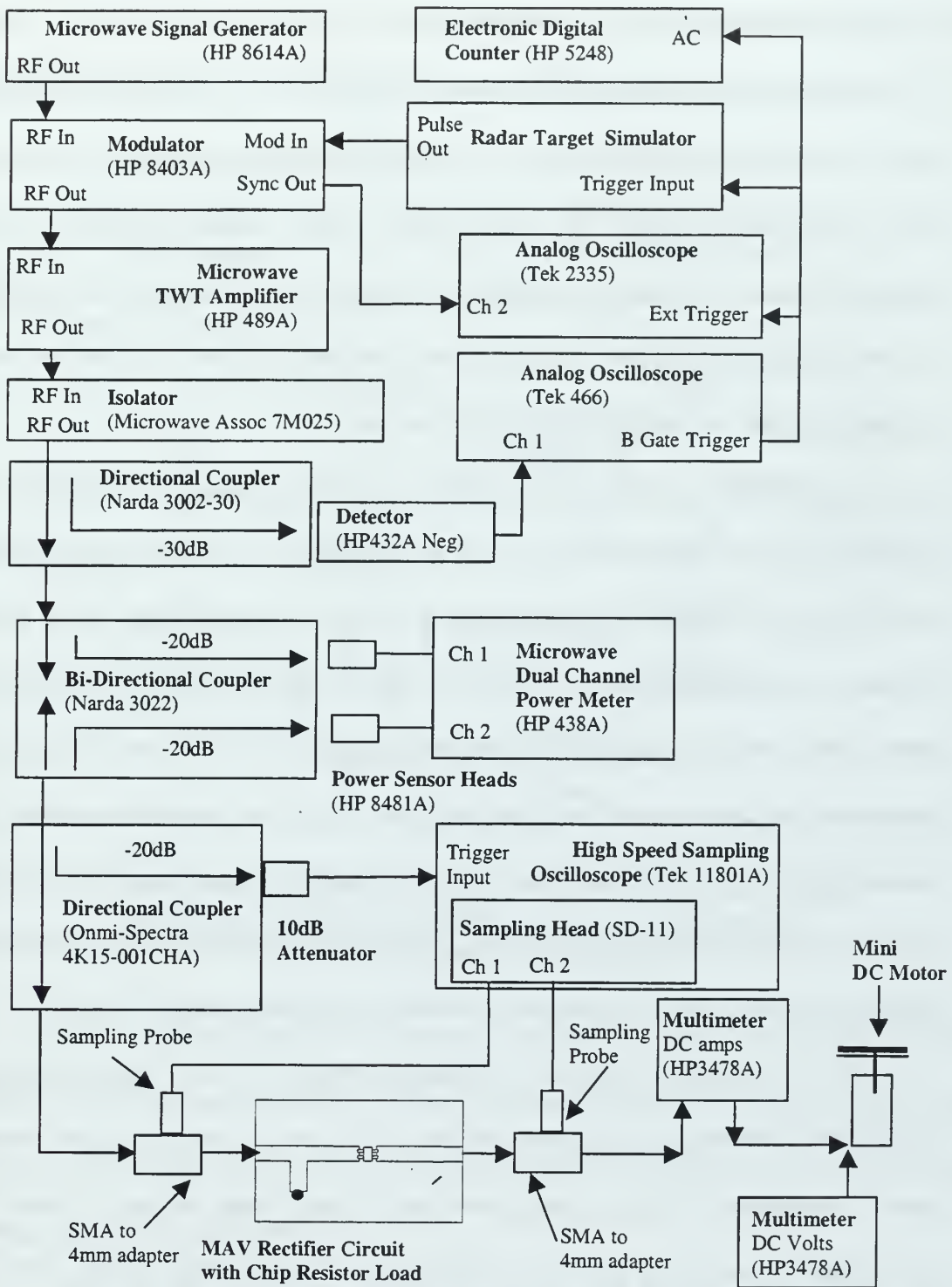


Figure 59. Block Diagram of RF-to-DC Conversion Efficiency Measurement, Pulsed CW Input Signal and DC Motor Loading.

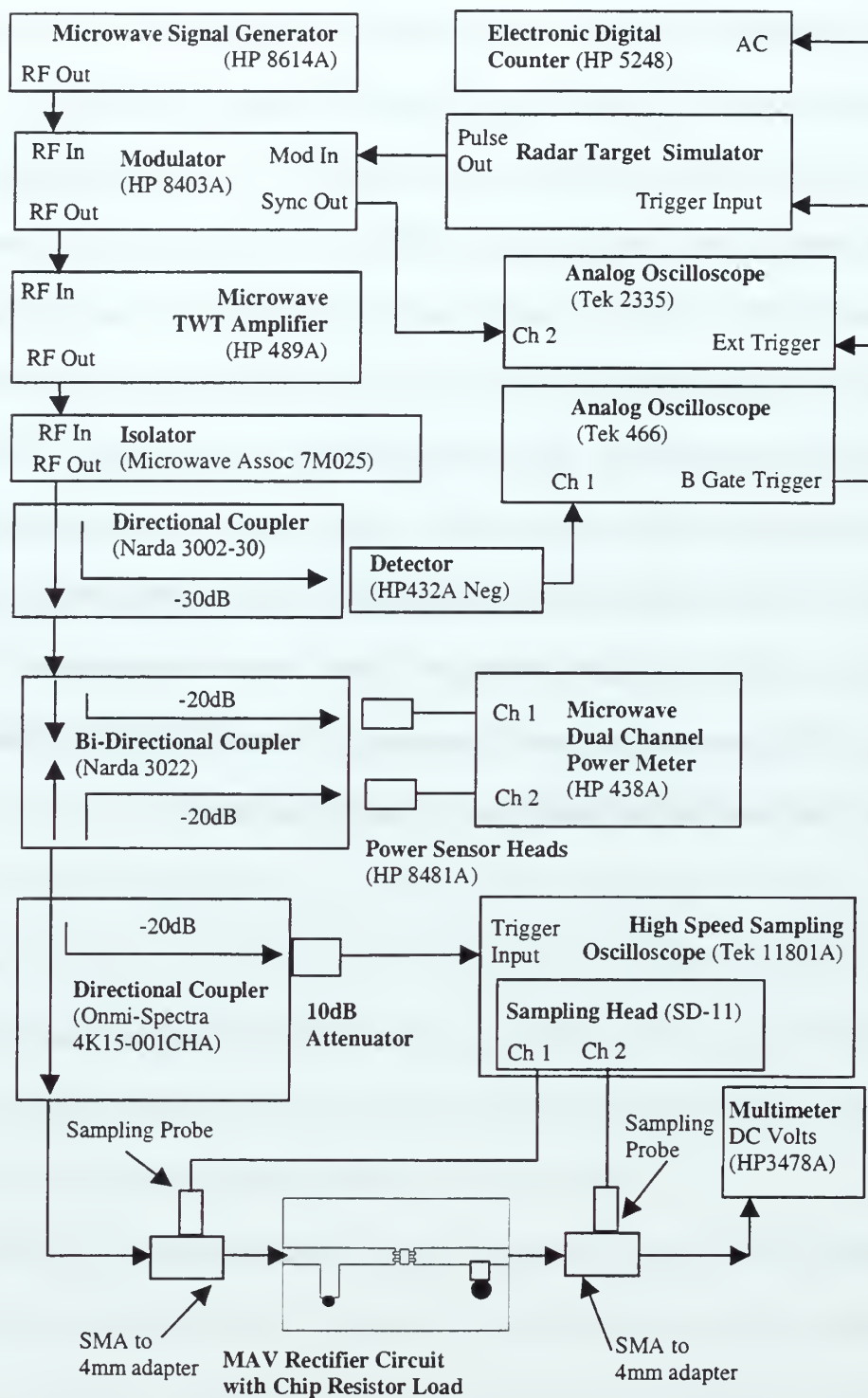


Figure 58. Block Diagram of RF-to-DC Conversion Efficiency Measurement, Pulsed CW Input Signal and Chip Resistor Loading.

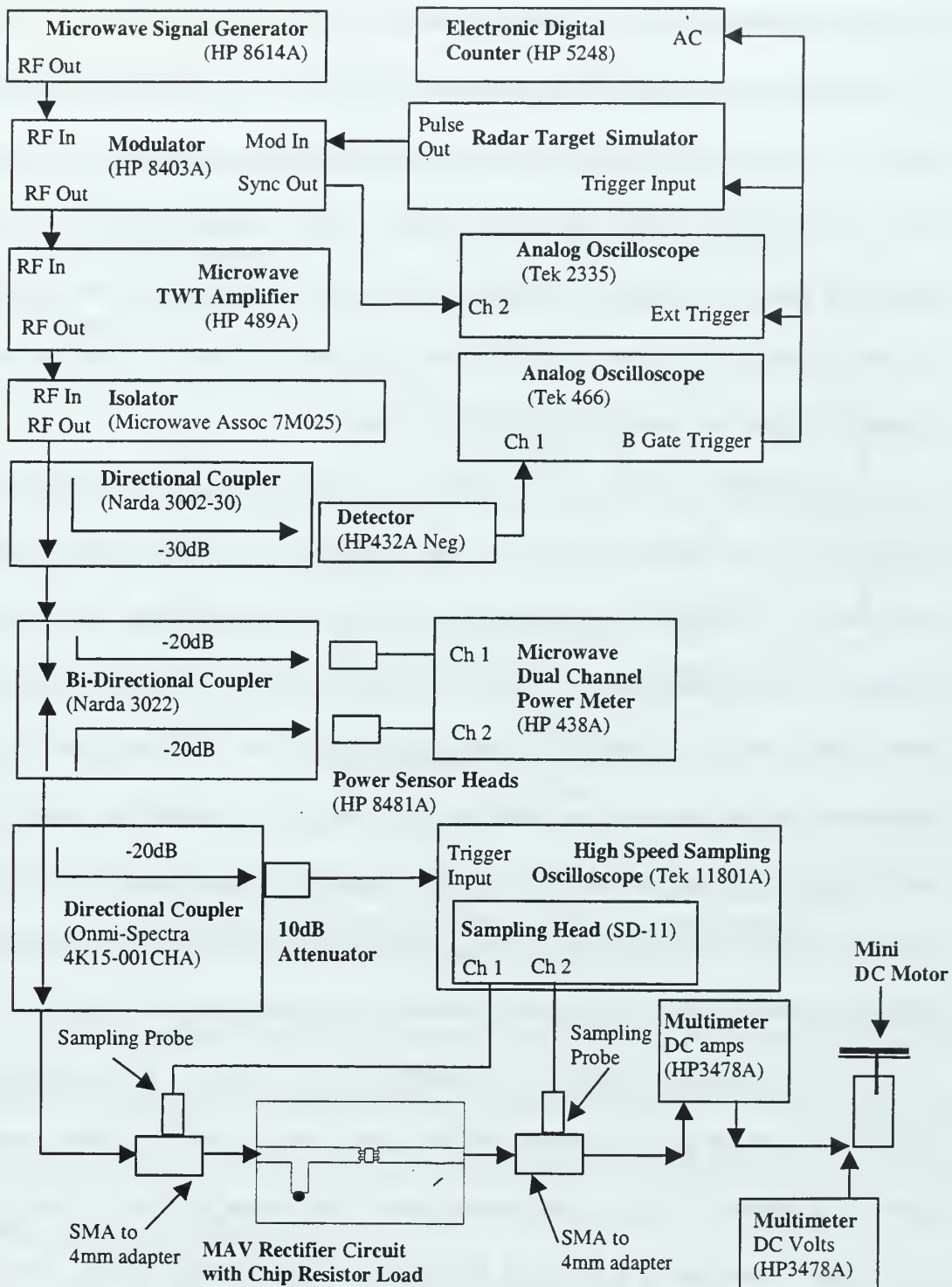


Figure 59. Block Diagram of RF-to-DC Conversion Efficiency Measurement, Pulsed CW Input Signal and DC Motor Loading.

1. Microwave Power Measurements

Measurement of incident and reflected microwave power ($P_{incident}$ and $P_{reflected}$) were made using a dual microwave power meter (Hewlett Packard model 438A) and two thermocouple based sensors (Hewlett Packard model 8481A). Since the incident microwave power measurement is crucial to accurate conversion efficiency calculation, characterization of these power sensor devices is necessary in order to understand how their use may effect the conversion efficiency measurement.

The HP8481A power sensor consists of two thermocouples connected in series. Thermocouples are heat-based sensors and are considered to be true averaging microwave power detectors. Each thermocouple consists of two dissimilar metals. They are joined together in two junctions, one of which is heated by incident microwave energy and the other is left at room temperature. These junctions, called the “hot” and “cold” junctions, generate an emf due to two effects, one being the voltage due to dissimilar metals and the second effect due to the heating of one junction causing electron diffusion and an opposing electric field due to Coulomb’s law. The combined effect, referred to as the Seebeck Effect [Ref 20], provides a net thermoelectric DC voltage of the thermocouple junction.

The DC voltage generated by each thermocouple is very low. The specifications for the HP8481A sensor give 160 nano-volts for every 1 micro-watt of incident microwave power. Additional circuitry in the power sensor and meter are used to transmit the thermocouple signal along a length of cabling to the power meter without effecting the power measurement. Circuitry within the sensor chops the tiny measured DC voltage to form a square wave. The square wave is amplified and AC coupled to the transmission line leading to the power meter. The square wave signal is synchronously detected at the power

meter to produce the power measurement. Figure 60 provides a block diagram of the Hewlett-Packard microwave power measurement system using thermocouple sensors.

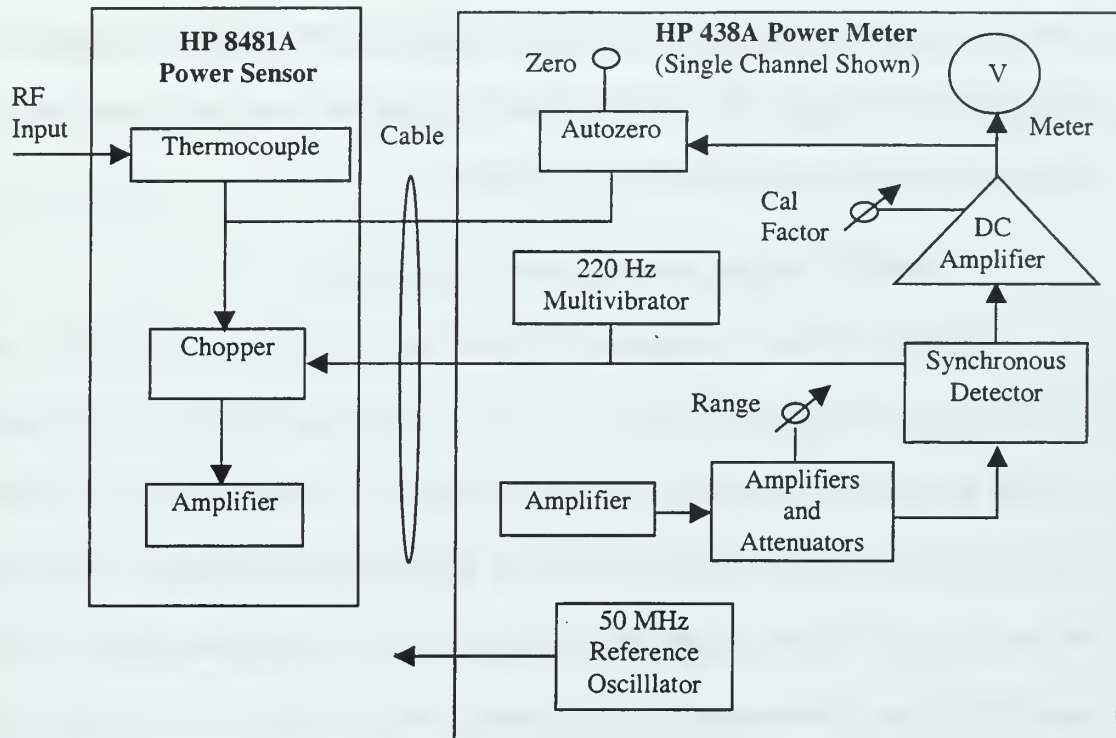


Figure 60. Block Diagram of Microwave Power Measurement System using the Hewlett Packard HP8481A Thermocouple Sensor and HP438A Power Meter [Ref 20].

Prior to making a power measurement, each thermocouple power sensor was first zeroed at the power meter and then calibrated using a 50 MHz, 1 mW reference signal from the power meter. The calibration was conducted whenever equipment was energized and during every 4 hours of operation.

Although diode power sensor technology could have been used to measure microwave power, available diode power sensors provide accurate square law values, and hence linear power measurements, only at lower power levels (-70 dBm to -20 dBm).

Thermocouple power sensors, such as the HP 8481A sensor, maintain pure square law power detection for higher power levels, from -30 dBm to +20 dBm. Newer wide dynamic range diode power sensors, such as the Hewlett Packard model E4412A, can provide CW power measurements from -70 to +20 dBm. However, for modulated signals such as a pulsed CW signal from the AN/SPS-58 radar transmitter, even these new diode power sensors do not provide accurate square law detection.

2. Rectified Output Average Power Measurements

The measurement of average or DC power on the output side of the MAV rectifier circuit was less straightforward than the incident power measurements. It was discovered through experimental trials that the type of circuit load affected the rectifier efficiency measurements. The actual loading for the MAV application would be either a battery system or a miniature DC motor. Therefore two types of circuit loading were used for the MAV rectifier efficiency measurements. The battery system loading was simulated in these measurements by the use of a 37-ohm chip resistor load. An inexpensive miniature DC permanent magnet hobby motor was used for the miniature DC motor loading case.

When the chip resistor loading was used, measurements of P_{DC} were made by measuring the average DC voltage across a chip resistor (37 ohm) load, as indicated in Figure 57. This chip resistor was surface mounted to the microstrip rectifier board with one side at the rectifier output voltage and the other soldered to ground using a via through the microstrip board. A HP3478A digital multimeter was used to make the average voltage measurement. High impedance probes were not available and therefore the multimeter test leads may have loaded the rectifier circuit.

When the rectifier circuit was loaded by the miniature DC motor, P_{DC} was determined by measuring both voltage across and current through the permanent magnet DC motor load. Measurements were made using two HP3478A digital multimeters, one each for voltage and current. The multimeter measuring average or DC current was located within the output circuit, it was not known whether or not the multimeter may have affected the measurement.

C. CONVERSION EFFICIENCY MEASUREMENT RESULTS

Table 11 provides a listing of conversion efficiency measurements that were conducted for several rectifier circuits with various loading conditions. Loading conditions consisted of: (a) chip resistor; (b) chip resistor with external capacitor and (c) miniature DC motor.

Figure	Circuit Designation	Description	Input Signal	Circuit Loading
Figure 61	m3-2	Dual Si-SBD Rectifier, external double shunt stub impedance tuner.	1.0 GHz CW	DC Motor; Chip Resistor
Figure 62	m4-2	Dual Si-SBD Rectifier external double shunt stub impedance tuner.	1.0 GHz CW	DC Motor
Figure 63	m7d-9	Single Si-SBD Rectifier with Shunt Stub impedance element	1.3 GHz CW; Pulsed 1.3 GHz CW	Chip Resistor; Chip Resistor plus capacitor
Figure 64	m8d-8	Dual Si-SBD Rectifier with shut stub impedance element	1.3 GHz CW; Pulsed 1.3 GHz CW	Chip Resistor; Chip Resistor plus capacitor
Figure 65	m8d-8	Dual Si-SBD Rectifier with shut stub impedance element	Pulsed 1.3 GHz CW	Chip Resistor; Chip Resistor plus capacitor

Table 11. Summary of Rectifier Efficiency Measurements.

The maximum rectifier efficiency obtained was approximately 30% for the configurations listed in Table 11. This efficiency is shown in Figure 61 and occurred for the two parallel SBD circuit configuration at an input signal of 1.0 GHz CW with a miniature DC motor as the load. This particular circuit configuration used an external double shunt short circuit stub tuner to match the rectifier impedance to the 50 ohm line. The tuner was

adjusted to maximize power transfer at all input power levels which allowed the rectifier circuit to be matched to the line at the power level tested. This reduced the input reflection coefficient of the circuit, because the input impedance of Si-SBD changes with input power level. Subsequent circuit designs, namely Circuit m7d-8 and m7d-9, incorporated a single short circuit stub tuner located on the rectifier microstrip circuit. This microstrip element, which does not allow impedance tuning for different input power levels, was necessary to fit the entire MAV rectifier within the physical envelope of the MAV antenna.

Subsequent circuit designs (Circuit m7d-8, m7d-9) were not measured for average power output using a DC motor loading since these designs incorporated a 37 ohm chip resistor load into the MAV rectifier circuit. Measurement of voltage across a DC motor alone can not describe the operating power level of the motor since the voltage across a DC motor varies as

$$V_a = I_a R_{dc} + K_v \omega_r , \quad (34)$$

where V_a is the average voltage across the motor terminals, I_a is the current supplied to the motor, R_{dc} is the motor resistance at DC, K_v a constant that accounts for the magnetic flux of the field and ω_r is the motor speed [Ref 21]. Measurement of both voltage across and current through the DC motor is required in order to obtain the power supplied to the motor. The available equipment to measure current, a multimeter, would be in series with the DC motor load and the microwave signal loading effects of the multimeter were unknown. Therefore it was decided to focus on measuring rectifier average output power using the chip resistor loading where the output transmission lines could be kept short and adverse effects minimized.

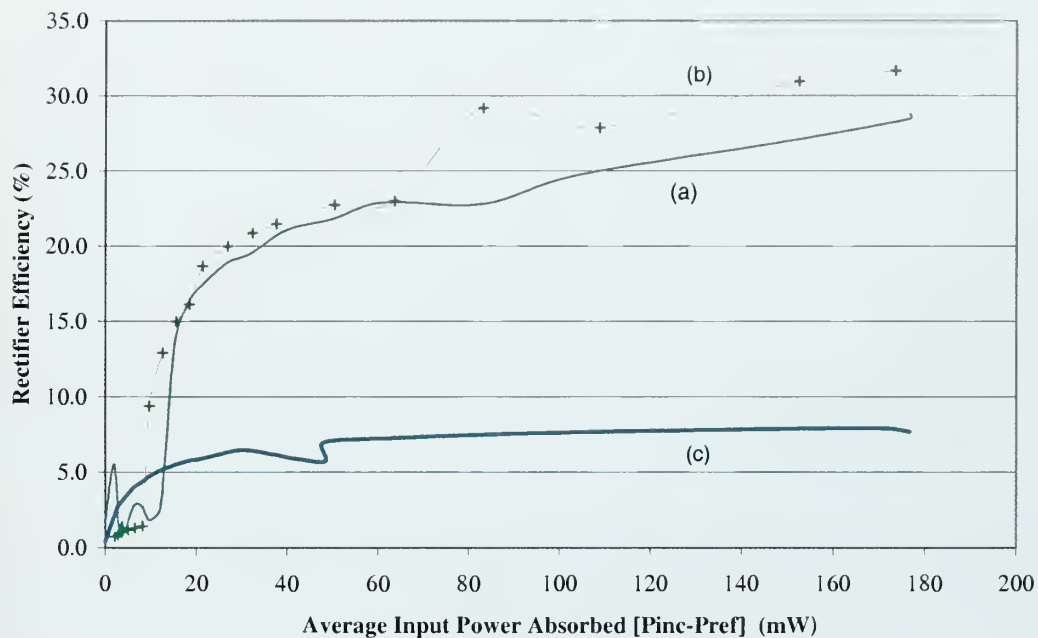


Figure 61. MAV Rectifier Efficiency Measurements for Two Parallel Si-SBD Microstrip Rectifier Circuit (Circuit M3-2) with External Double Short Circuit Stub Impedance Matching Tuner.
 (a) 1.0 GHz CW Input Signal with Miniature DC Motor as Load.
 (b) 1.0 GHz CW Input Signal with Miniature DC Motor as Load.
 (c) 1.0 GHz CW Input Signal with 10 ohm Lumped Element Resistor as Load.

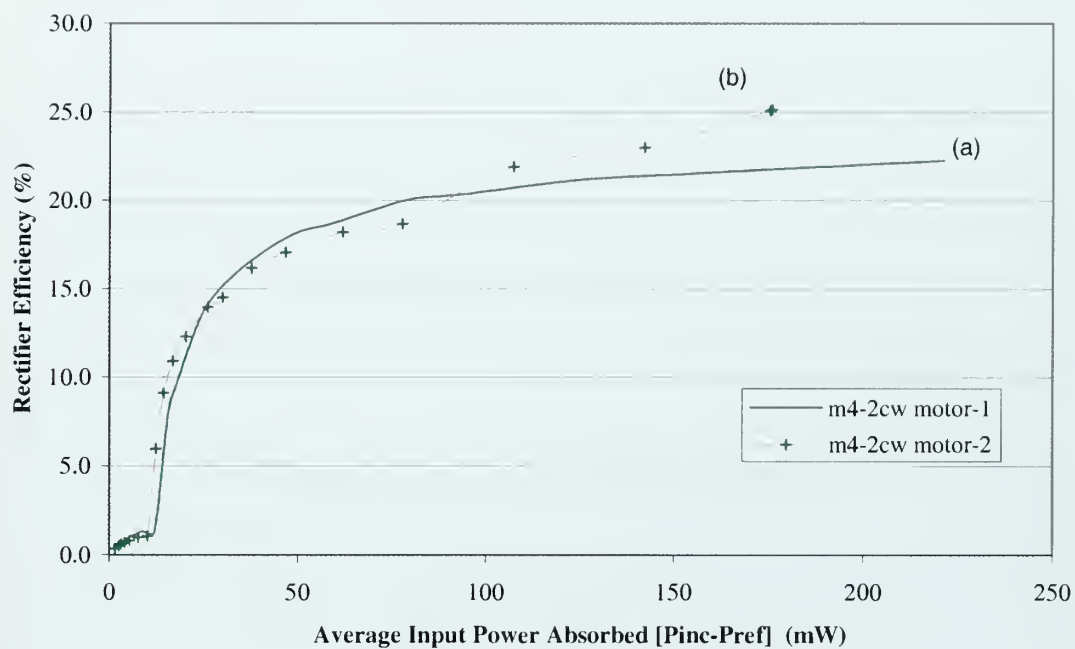


Figure 62. MAV Rectifier Efficiency Measurements for two Parallel Si-SBD Microstrip Rectifier Circuit (Circuit m4-2) with External Impedance Matching Tuner.

(a) 1.0 GHz CW Input Signal with Miniature DC Motor as Load.

(b) 1.0 GHz CW Input Signal with Miniature DC Motor as Load (Second Data Set).

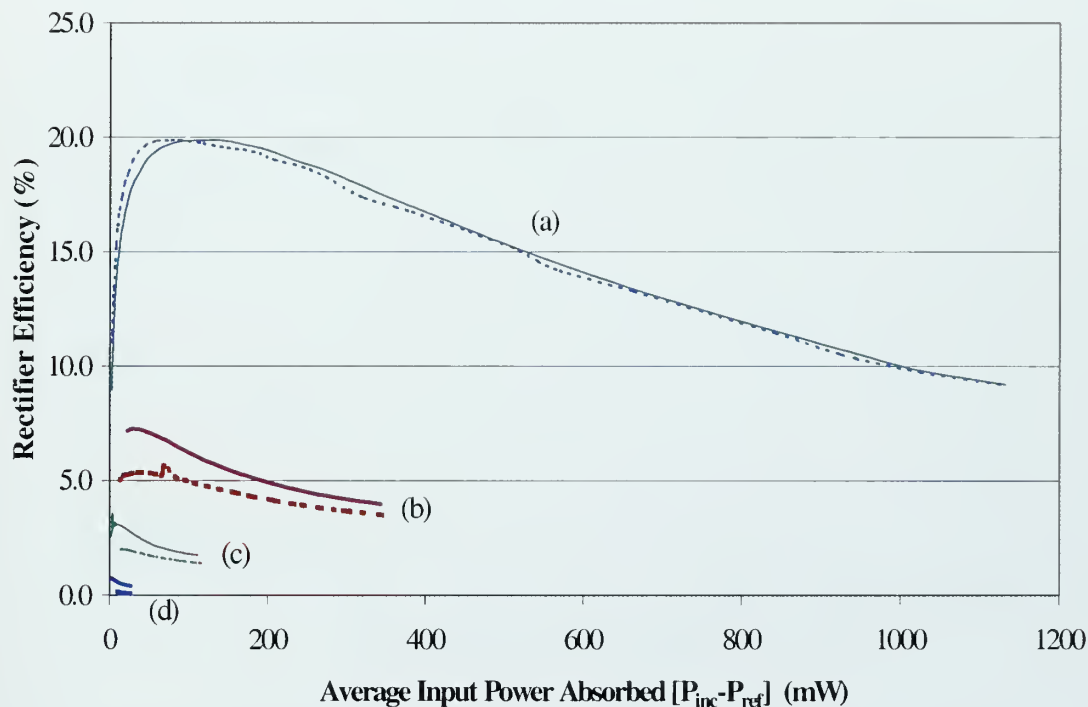


Figure 63. MAV Rectifier Efficiency Measurements (Circuit m7d-9)
Single Si-SBD Microstrip Rectifier Circuit
with Shunt Stub Impedance Matching.

Circuit Loading:

(Solid Line) 39.7 ohm Chip Resistor with 10 uF Capacitor in Parallel.

(Dashed Line) 39.7 ohm Chip Resistor.

Input Signals:

(a) 1.3 GHz CW.

(b) 1.3 GHz CW Modulated by 7uS Pulse at prf= 36k (Duty Cycle= 0.25).

(c) 1.3 GHz CW Modulated by 7 uS Pulse at prf= 13k (Duty Cycle= 0.09).

(d) 1.3 GHz CW Modulated by 7 uS Pulse at prf= 3k (Duty Cycle= 0.02).

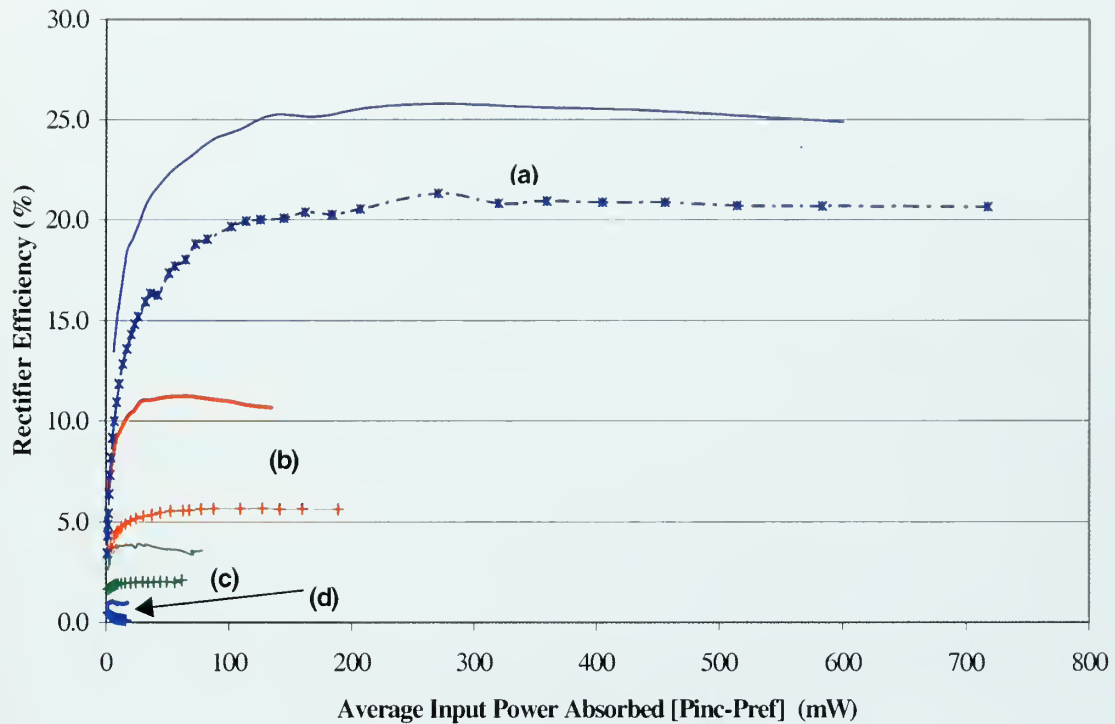


Figure 64. MAV Rectifier Efficiency Measurements (Circuit m7d-8)
Two Parallel Si-SBD Microstrip Rectifier Circuit
with Shunt Stub Impedance Matching.

Circuit Loading:

(Solid Line) 39.7 ohm Chip Resistor with 10 uF Capacitor in Parallel.

(Dashed Line) 39.7 ohm Chip Resistor.

Input Signals:

(a) 1.3 GHz CW.

(b) 1.3 GHz CW Modulated by 7uS Pulse at prf= 36k (Duty Cycle= 0.25).

(c) 1.3 GHz CW Modulated by 7 uS Pulse at prf= 13k (Duty Cycle= 0.09).

(d) 1.3 GHz CW Modulated by 7 uS Pulse at prf= 3k (Duty Cycle= 0.02).

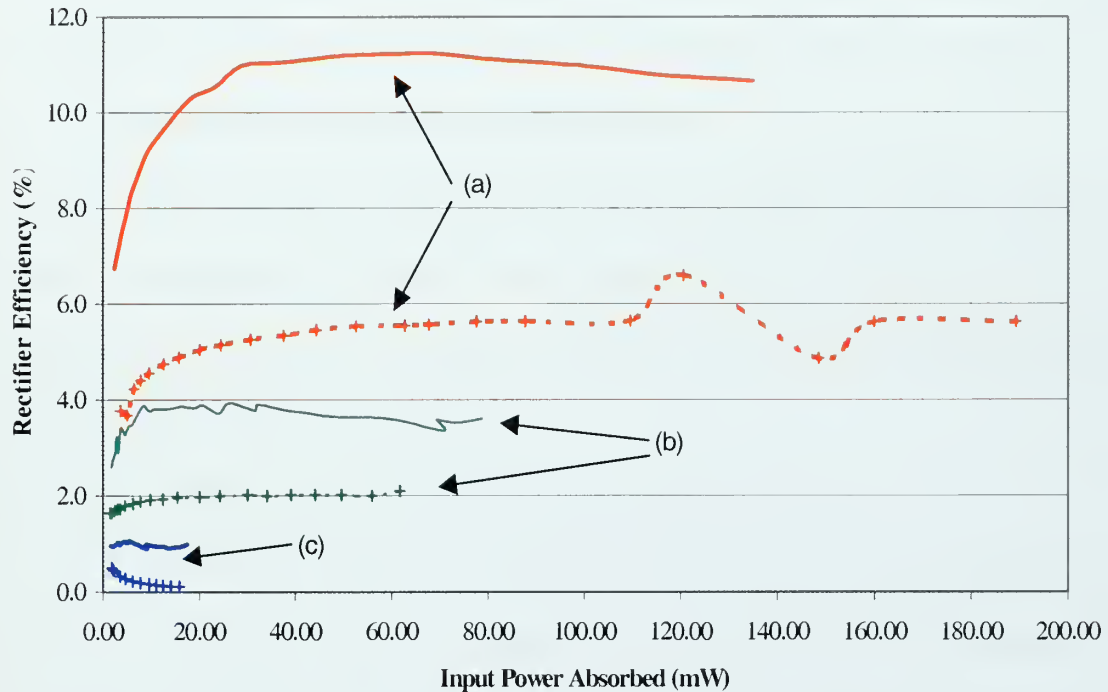


Figure 65. MAV Rectifier Efficiency Measurements – Expanded (Circuit m7d-8)
Two Parallel Diode Rectifier Circuit with Shunt Stub Impedance Matching
Expanded Scale showing Only Pulsed CW Input Signal Results.

Circuit Loading:

(Solid Line) 39.7 ohm Chip Resistor with 10 uF Capacitor in Parallel.

(Dashed Line) 39.7 ohm Chip Resistor.

Input Signals:

(a) 1.3 GHz CW Modulated by 7uS Pulse at prf= 36k (Duty Cycle= 0.25).

(b) 1.3 GHz CW Modulated by 7 uS Pulse at prf= 13k (Duty Cycle= 0.09).

(c) 1.3 GHz CW Modulated by 7 uS Pulse at prf= 3k (Duty Cycle= 0.02).

D. SUMMARY OF CONVERSION EFFICIENCY RESULTS

Conversion efficiency measurements demonstrated the nonlinearity of Si-SBD circuitry and that rectifier circuit loading can influence rectifier conversion efficiency. Specifically the following effects were observed in the rectifier efficiency measurements.

1. Minimum Incident Power Requirement

A minimum input power level was required to achieve an average output or DC power and therefore rectification. This minimum incident microwave power level was larger when the load was a DC motor. This effect is seen clearly in Figure 61 for Circuit m3-3 and Figure 62 for Circuit m4-2.

2. Applied Microwave Power for Peak Rectifier Efficiency

The efficiency peaked for incident microwave signal power after which the efficiency either held constant or began to drop. Efficiency for the single Si-SBD configuration peaked at 20 percent for approximately 100 mW of average microwave power. Increasing the incident microwave power showed a noticeable drop in rectifier efficiency as shown in Figure 63 for Circuit m7d-9. The peak for the two parallel Si-SBD configuration also peaked at approximately 20 percent, however, this peak occurred at 200 mW of average microwave power. Rectifier efficiency was observed to hold constant at 20 percent for average microwave powers above 200 mW

3. Efficiency Decrease for Incident Power Above Peak Efficiency

When incident microwave power levels exceeded the level at which peak rectifier efficiency was achieved, the rectification efficiency had the tendency to decrease as the incident power level was increased. This effect is clearly shown in Figure 63 for the single

SBD diode circuit, m7d-9. As the power level increases, the current through the diode increases and corresponding ohmic or I^2R losses increase. These ohmic losses across the diode generate heating which, if increased too high, can result in destruction of the Si-SBD. Device heating from the increased ohmic losses can also increase the diode impedance and result in larger reflected microwave power ($P_{reflected}$), which further erodes the rectifier efficiency.

4. Multiple SBDs in Parallel Increase the Rectifier's Power Rating

When multiple SBDs in parallel were used, the peak rectifier efficiency remained at peak performance values for a wider range and larger incident microwave power levels than when the circuit contained only a single SBD. This result is clear from the data graphed in Figure 65 for the two parallel Si-SBD rectifier circuit, m7d-8. Incident microwave power values for peak efficiency increased slightly, but was not too appreciable. Therefore by using multiple SBD in a parallel arrangement, a rectifier circuit can be produced that would rectify higher incident power levels with no decrease in efficiency and does not require a much larger incident power to operate.

5. Circuit Loading Affects the Rectifier Efficiency

When a parallel capacitance was added to the chip resistor load, the rectifier conversion efficiency was noticeably increased. Figure 64 and Figure 65 demonstrate this efficiency increase for both CW and pulsed CW incident microwave signals. The largest efficiency increase was achieved for the pulsed CW. The efficiency increase for a CW incident signal was from 20 to 25 percent, which results in a 25 percent increase in efficiency over a circuit with no parallel capacitance. The increase for the 0.25 duty cycle,

pulsed CW incident power signal was from 5.5 percent to 11 percent, which corresponds to about a 100 percent increase in efficiency.

When a miniature DC motor was used as the load, rectification efficiency improved. This improvement required a slightly higher incident power to achieve the peak rectification efficiency as compared to a resistor load. However, the peak efficiency achieved was much greater. Figure 61 displays the efficiency difference between a DC motor load and a resistor load for the parallel Si-SBD at 1.0 GHz CW input power signal. Rectifier efficiency for this circuit using DC motor loading increased to greater than 20 percent versus the 8 percent for resistor loading. Also shown in Figure 61, the rectifier efficiency seemed to improve as incident power was increased with no decrease in efficiency at higher power levels. However in that particular test, the available input power was limited 180 mw. It is expected that rectifier efficiency would have decreased had higher power incident microwave signals been used.

It should be noted that while conducting efficiency testing with DC motor loading, significant variation in results was obtained when an appreciable amount of lead length existed between the rectifier circuit and the DC motor. Lead lengths were minimized and affixed into position to avoid changes during measurements. It is recommended that the rectifier circuit be loaded with some sort of power storage device such as a battery or capacitor rather than the DC motor directly. The motor could then take its power from the battery or capacitor. This type of loading scheme would help solve two problems, (1) the RF loading of microwave rectifier affecting circuit input impedance and (2) the potential for motor power dropouts as the propagation paths to the MAV change.

E. RECOMMENDATIONS TO INCREASE CONVERSION EFFICIENCY.

Rectifier conversion efficiency measurements on the circuits described provide insight into making the following recommendations for future microwave rectification circuits.

1. Multiple SBDs in Parallel

The use of multiple SBDs in parallel can increase the dynamic range of the rectifier at the peak rectification efficiency. Placing multiple diodes in parallel lowers the forward resistance across the rectifier circuit by

$$R_{total\ forward} = \frac{R_{forward}}{N}, \quad (35)$$

where N is the number of SBDs in parallel and $R_{forward}$ is the forward resistance of a single SBD.

2. Addition of a Load Capacitance

A load capacitance should be incorporated into the rectifier circuit to increase the overall rectification efficiency.

3. Impedance Match SBD Diodes at the Expected Microwave Power

The impedance matching circuitry for the SBDs should be designed to match the impedance of the diodes at the expected input power levels. Power management could be used on the transmit side to help ensure that the power levels remain constant and that the rectifier circuitry matches the line impedance.

V. OPERATIONAL DEMONSTRATION OF WIRELESS POWER TRANSFER THROUGH FREE SPACE

A. INTRODUCTION

This chapter discusses an operational demonstration of the combined MAV antenna, microstrip rectifier circuit and DC motor, where the rectifier circuit and motor are contained within the upper half of the MAV antenna. Demonstrations were conducted to show the startup and operation of the miniature DC motor using only rectified microwave power transmitted over a short distance of free space. The demonstration showed that the miniature DC motor could be operated at visually determined speeds exceeding 500 rpm with less than 0.5 watt of transmitted power.

Two separate MAV models were tested: (1) MAV-1 was used for a 1.0 GHz CW signal WPT demonstration and (2) MAV-2 was used for 1.3 GHz CW and pulsed CW signals WPT demonstrations. The as-built MAV models were developed to simulate the physical characteristics of a rotorcraft type MAV currently under development by Lutronix. Because it was not intended to fly, weight reduction in the design and fabrication was not an issue.

B. DEMONSTRATION APPARATUS

The microwave signals transmitted through free space for the demonstration of WPT were of two basic types: CW and pulsed CW. These signals were used to demonstrate remote powering of the MAV DC motor at various distances. The motivation for using the pulsed CW signal was its similarity to the AN/SPS-58 air search radar, which is a potential

high power-transmitting source. Since the AN/SPS-58 radar uses a frequency of 1.3 GHz, CW and pulsed CW tests were conducted only at 1.3 GHz, whereas the testing at 1.0 GHz used only a CW waveform as the transmitted signal. Two setups were assembled to provide the demonstration of WPT for operation of the MAV. One setup used 1.0 GHz CW as the transmitting signal to power the MAV-1 model. The second setup was for 1.3 GHz CW and pulsed CW waveforms and used to power the MAV-2 model.

The microwave power delivered to the transmitting horn for these experiments was limited to less than 2 watts because of available equipment. As a safety precaution, the electric field in free space was measured using a broadband radiation monitor (field strength meter). Measurements ensured personnel safety from excessive radiation when compared to IEEE/ANSI specification limits [Ref 22]. Safety limitations with regard to RF/microwave radiation exposure for human personnel are discussed further in Section 3. As a precaution, computers in the direct line of sight of the transmitting horn were covered with additional metal foil shielding to prevent damage.

1. 1.0 GHz CW Demonstration Apparatus

A block diagram of the equipment apparatus for the 1.0 GHz WPT demonstration is shown in Figure 66. Free space transmission of microwave power used a voltage-controlled oscillator (VCO) as the 1.3 GHz CW signal source. The 1.3 GHz CW signal was increased to a maximum of 200 mW by a solid state variable gain microwave amplifier (HP8347A) and then fed to a large L-band pyramidal standard gain horn antenna (Microline/FXR L638A). Thermocouple power sensors and a power meter measured incident and reflected power to the transmitting horn antenna via a dual directional coupler (Narda 3022). The

double stub short circuit tuner placed between the transmitting horn antenna and the directional coupler was used to help impedance match the antenna to the 50 ohm coaxial cable transmission line. A photograph of the demonstration is shown in Figure 67.

The MAV-1 model used for the 1.0 GHz CW WPT demonstration consisted of a copper pipe dipole antenna and microstrip SBD rectifier, (designated as Circuit 6C in Chapter II Section F), designed for operation at 1.0 GHz. A photo of MAV-1 situated in front of the horn antenna aperture is shown in Figure 68. A photo of the disassembled MAV-1 model with dimensions for the antenna and rectifier (circuit 6C) are shown in Figure 69.

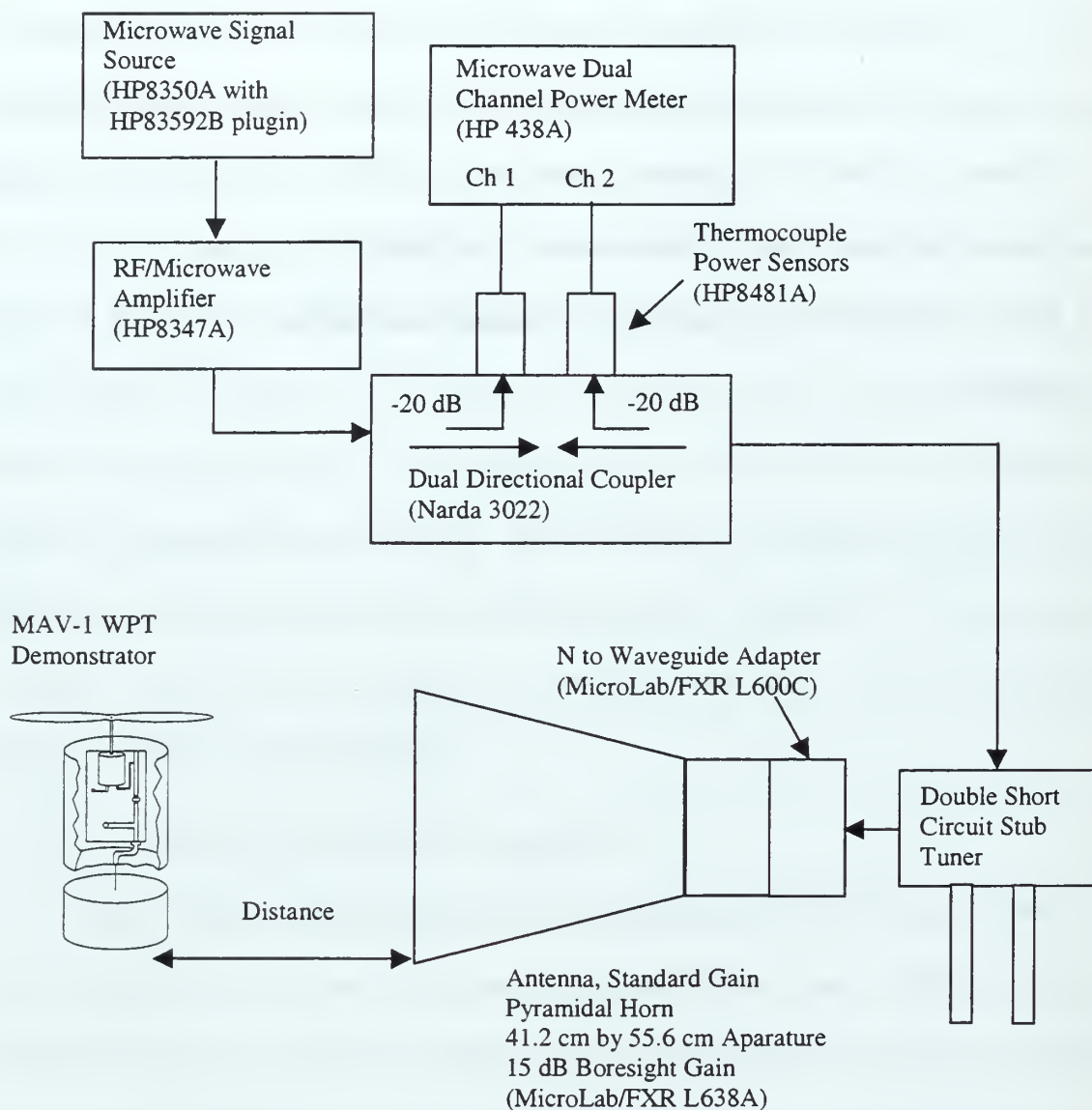


Figure 66. MAV-1 (1 GHz CW) Wireless Power Transfer Demonstration Aparatus.

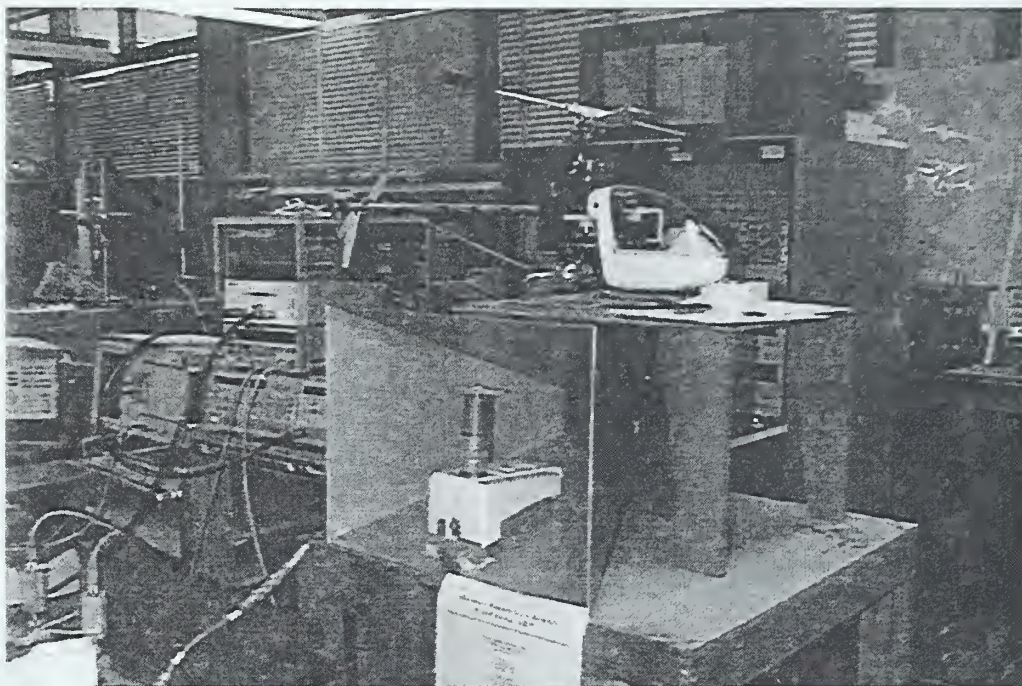


Figure 67. Wireless Power Transfer Demonstration
1.0 GHz CW Transmission Signal to Power MAV-1.

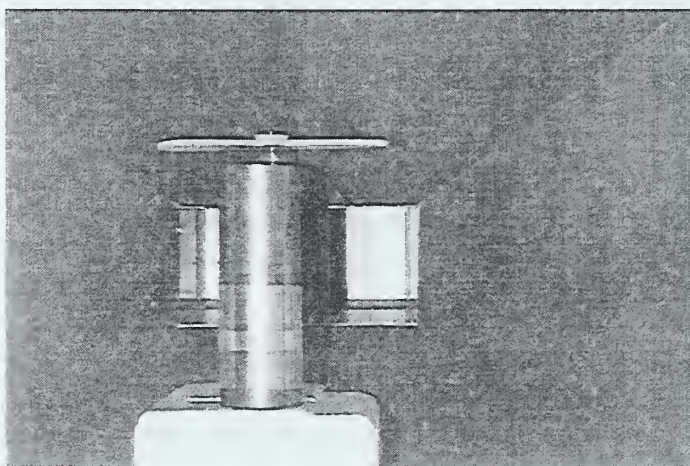
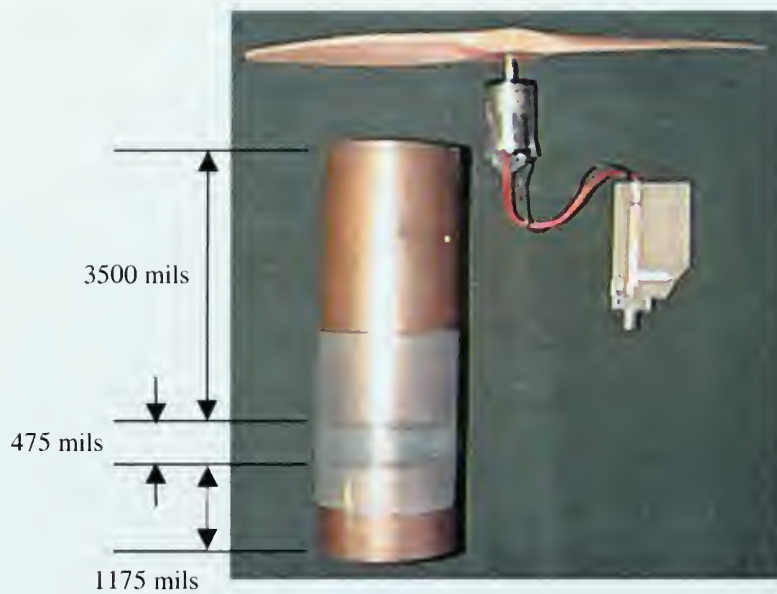
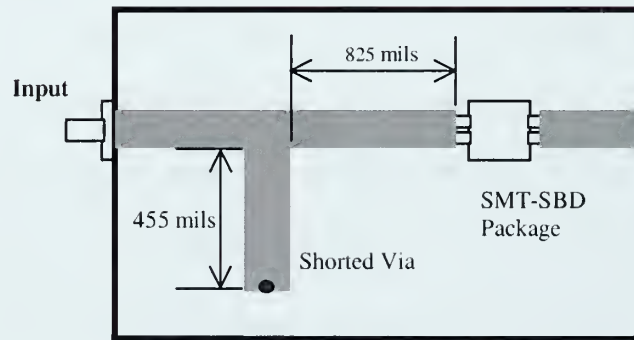


Figure 68. MAV-1 at the Face of the Transmitting Horn Aperture.



(a)



Etched FR-4 PC Board, 110 mil line width

(b)

Figure 69. MAV-1 Model for 1.0 GHz WPT Demonstration.
 (a) MAV-1 Antenna and Rectifier Disassembled with Antenna Dimensions.
 (b) MAV-1 Microstrip Rectifier Circuit Dimensions.

2. 1.3 GHz CW and Pulsed CW Demonstration Apparatus

A block diagram of the apparatus for the WPT demonstration of 1.3 GHz CW and pulsed CW signals is shown in Figure 70. The microwave CW and pulsed CW signal is supplied by methods similar to those explained in Chapter IV for the rectifier efficiency testing. For this setup the microwave traveling wave tube (TWT) amplifier (HP489A) supplied up to 1.8 watts of average power to the pyramidal horn antenna. The TWT supplied a larger power level than the solid state amplifier (HP8347A) used in 1 GHz WPT demonstration. Because of the higher power, the transmission range of the MAV-2 model was further from the transmitting horn antenna than the range for the MAV-1 demonstration. As in the case of the 1.0 GHz WPT demonstration, a double stub tuner was attached to the input of the transmitting horn antenna to help impedance match the horn antenna to the 50 ohm coaxial cable line. Photos of the 1.3 GHz WPT demonstration as setup in the NPS Radar Laboratory are shown in Figure 71 and Figure 72.

The MAV-2 model consisted of a design similar to MAV-1 with dimensions changed to suit the 1.3 GHz operating frequency. A photo of the disassembled MAV-2 model is shown with antenna and rectifier circuit dimensions in Figure 73.

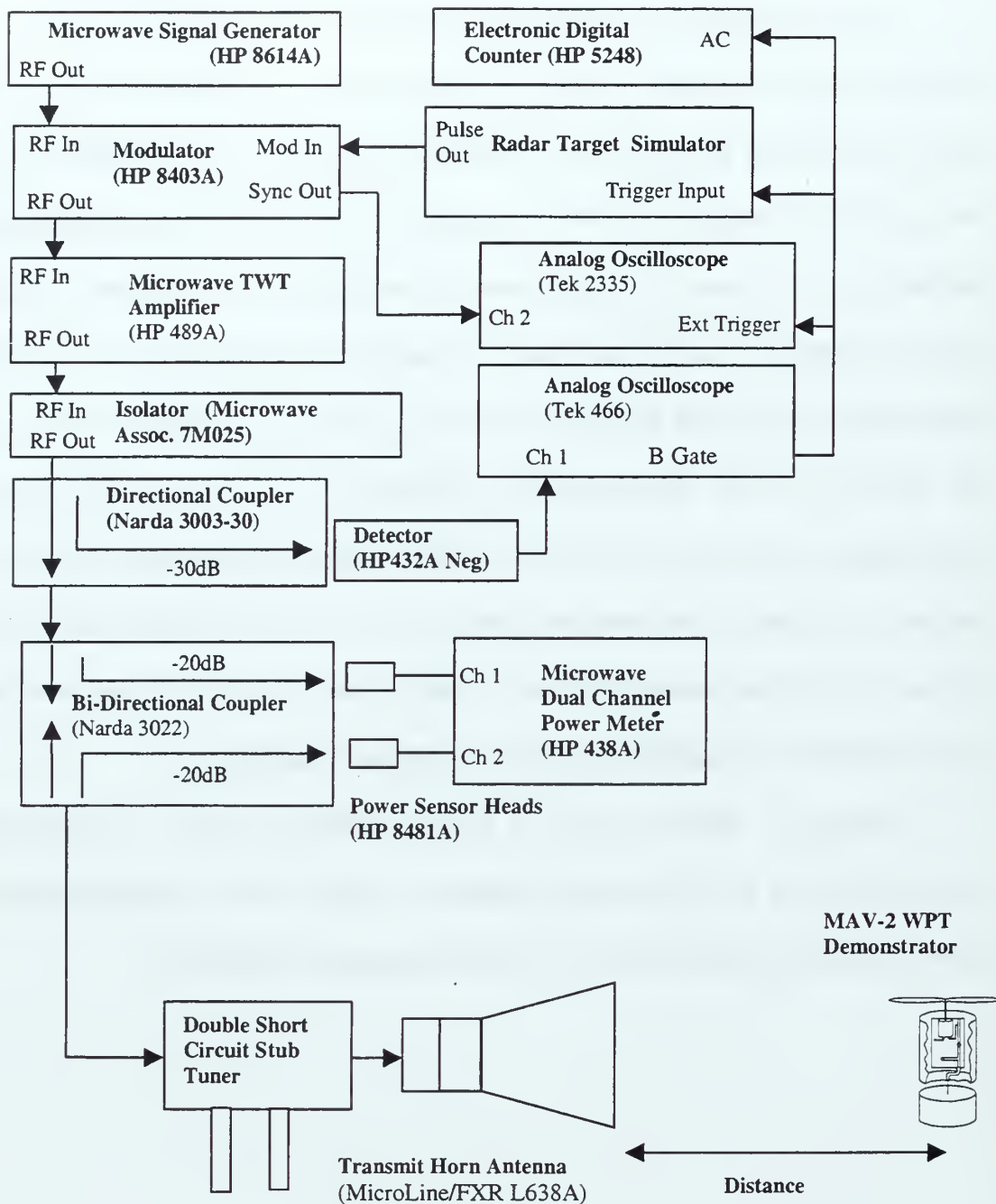


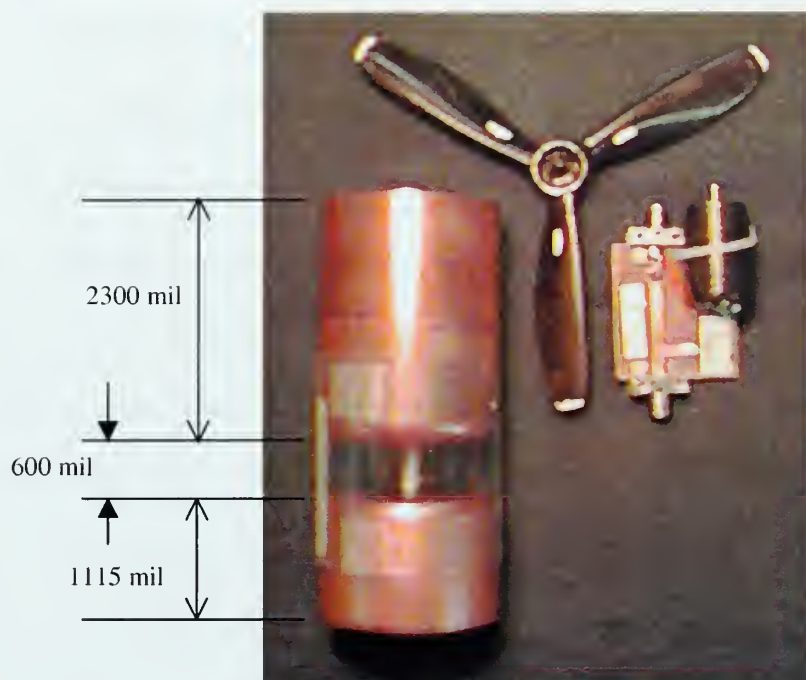
Figure 70. Block Diagram of Wireless Power Transfer Demonstration Apparatus
1.3 GHz CW and Pulsed CW Transmit Signals.



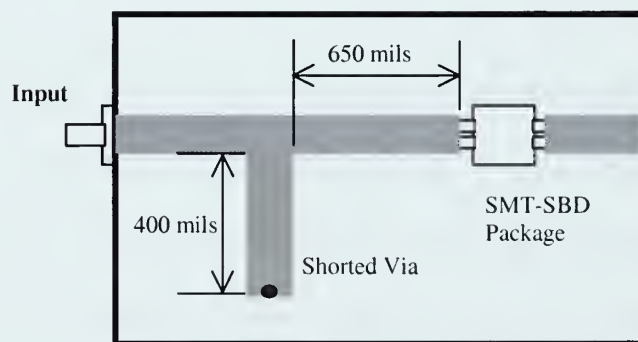
Figure 71. Wireless Power Transfer Demonstration
1.3 GHz CW and Pulsed CW Transmission to MAV-2.



Figure 72. Wireless Power Transfer Demonstration
1.3 GHz CW Transmission Operating DC Motor to MAV-2.



(a)



Etched FR-4 PC Board, 110 mil line width

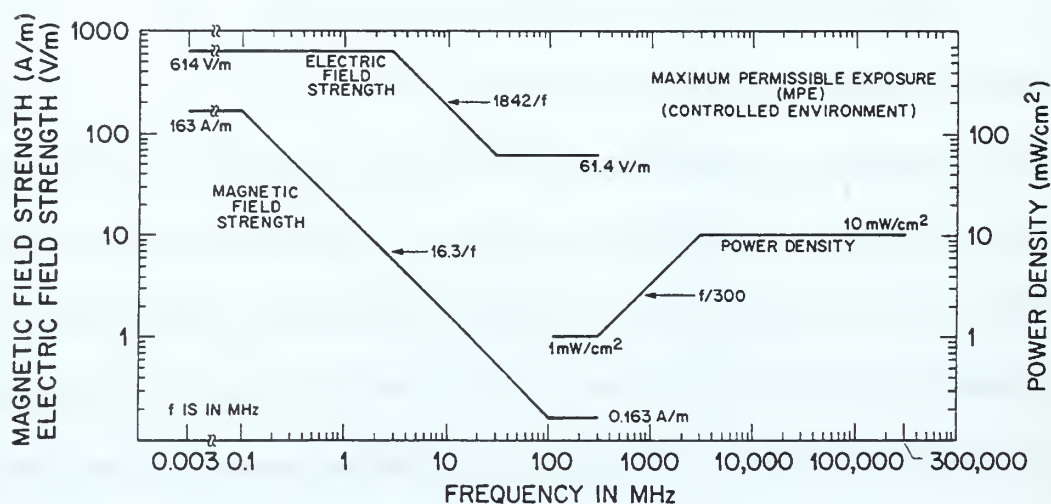
(b)

Figure 73. MAV-2 Model for 1.3 GHz WPT Demonstration.
 (a) MAV-2 Antenna and Rectifier Disassembled with Antenna Dimensions Indicated.
 (b) MAV-2 Microstrip Rectifier Circuit Dimensions (Circuit 7d-5).

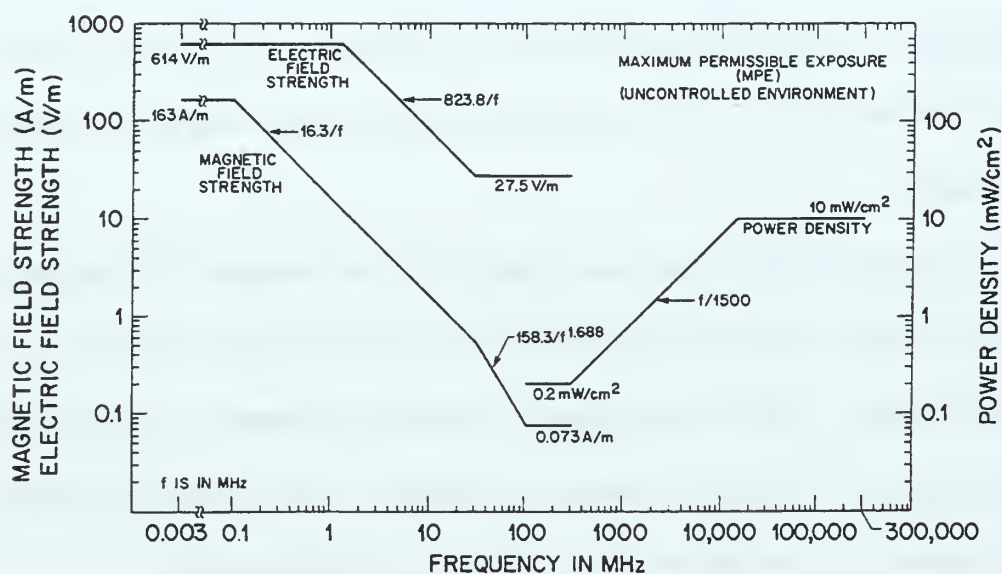
3. RF/Microwave Radiation Exposure Limitations to Human Personnel

Electromagnetic energy is called non-ionizing radiation. Due to the potential of high amounts of radiated power for WPT applications, EM safety for personnel and equipment must be considered. Acceptable levels of RF/Microwave radiation for personnel safety have been established and published by the Institute of Electrical and Electronic Engineers (IEEE) and are recognized as an American National Standard (ANSI) [Ref 22]. Graphs illustrating safety limits verses frequencies are shown in Figure 74 for controlled and uncontrolled environments. Essentially, the controlled environments are described as being areas where personnel that may be exposed to RF/Microwave radiation are knowledgeable of the hazard and have the appropriate devices to measure the power density of the fields radiating them. Uncontrolled environments are locations where personnel might not be aware of the hazard or do not have appropriate equipment to measure the incident field power density.

The recommended power density limits for human exposure at the frequencies used in this WPT demonstration are 3.33 mw/cm^2 for 1.0 GHz operation and 4.33 mw/cm^2 for 1.3 GHz operation. These values assumed a controlled environment. Because of amplifier power limitations, RF/Microwave radiation values were exceeded only for locations inside of the aperture of the horn antenna at the 1.3 GHz CW operating signal.



(a)



(b)

Figure 74. Maximum Permissible Exposure to RF/Microwave Radiation [Ref 22].

- (a) Controlled Environment Specifications.
- (b) Uncontrolled Environment Specifications.

C. MICROWAVE LINK POWER BUDGET

As a result of conducting rectifier efficiency measurements using a miniature DC motor as a load, it was determined that a minimum amount of input microwave power is required in order to start the motor turning and to keep it spinning. This amount of power varies with the MAV model being used and the type of signal transmitted. Typically, the average microwave power required by the rectifier circuits for a miniature DC motor operation was 15 mW.

To obtain the required average microwave power level at the input to the rectifier circuit, it is useful to understand the range at which power levels like this can be achieved. One means to get this value is to use the Friis free space transmission equation [Ref 14, 15]

$$P_{received} = P_T \frac{G_1 G_2 \lambda^2}{(4\pi r)^2} \quad (36)$$

where G_1 and G_2 are the power gains of the transmitting and receiving antennas, r is the distance between antennas, P_T is the power transmitted and λ is the operating wavelength. Typically (34) applies for electromagnetic field propagation in the far field zone of the transmitting antenna. In this case the transmitting antenna is the L-band Microline/FXR horn antenna. Calculation of the distance to the far field involves using [Ref 14, 15]

$$r_{far\ field} = \frac{2D^2}{\lambda}, \quad (37)$$

where D is the largest dimension on the antenna, which for a horn antenna is often taken as the distance across the diagonal of the aperture. The far field distance for the MicroLine/FXR L-band horn was calculated to be 4.6 meters for 1.0 GHz operation and 6 meters for 1.3 GHz operation. MAV fat dipole antenna gains were calculated using GNEC[®]

and resulted in values of 1.48 dB for 1.0 GHz operation and 1.67 dB for 1.3 GHz operation. Using (34), the gains for the MAV antennas, and a manufacturer's specification of 15 dB gain of the Microline/FXR horn antenna, the transmitter power required to operate the rectifier and DC motor combination at the far field boundary were calculated and are presented in Table 12.

MAV Model	Freq (GHz)	Transmitting Antenna Gain (G1) (dB)	Receiving Antenna Gain (G2) (dB)	Minimum Distance to Far Field (meters)	Minimum Transmit Power for MAV Operation (watts)
MAV-1	1.0	15	1.48	4.6	27 watts
MAV-2	1.3	15	1.67	6.0	73 watts

Table 12. Far Field Operation Specifications for WPT of MAV Demonstrators.

Required transmitter power for MAV operation verses distance was calculated using (34) and is plotted in Figure 75. These calculations assume that the MAV is in the far field and no other propagation losses are present other than free space path loss. The required power levels shown in Table 12 and Figure 75 would likely result in field power densities that exceeded the human safety levels previously shown in Figure 74 [Ref 22]. However power levels required for far field operation of the MAV models using the Microline/FXR horn antenna were not achievable with the available amplifier. The WPT demonstration therefore consisted of placing the MAV model in the near field of the horn antenna.

The high power microwave safety issue and its impact on the operational limitations of the MAV was addressed in more detail in [Ref 23]. An actual fielded system can operate

at ranges of 30 to 50 meters and remain within safety limits if the rectifier efficiency is increased, power management employed, and dwell times limited.

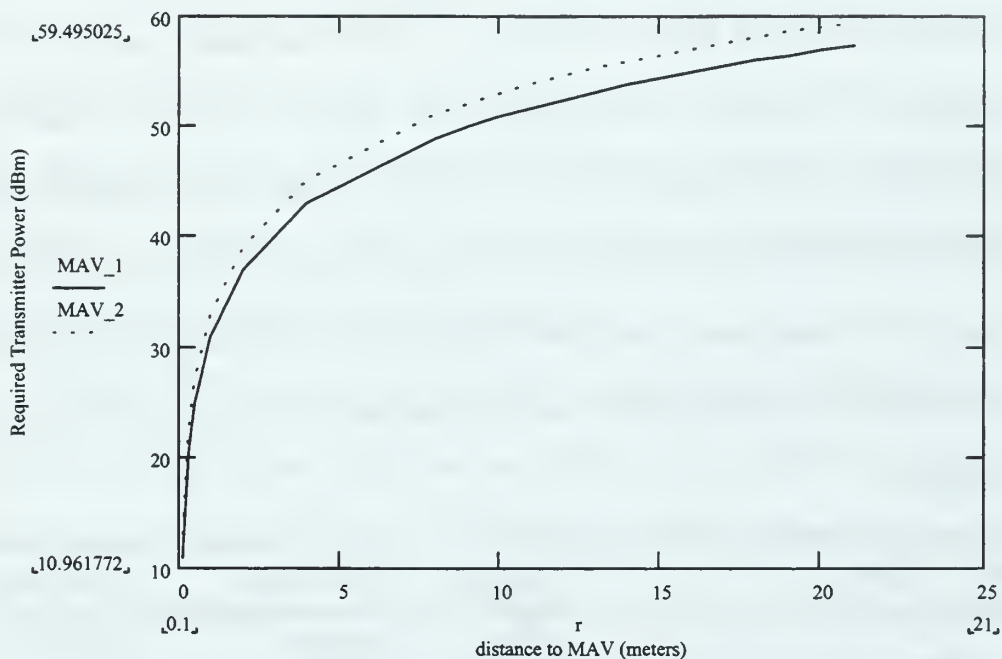


Figure 75. WPT Transmitter Power Levels for Far Field Operation of MAV. Transmit Antenna is 15 dB Pyramidal Horn, Required Power by MAV is 15 dBm.

D. FREE SPACE WPT DEMONSTRATION RESULTS

WPT was demonstrated at 1.0 GHz CW, 1.3 GHz CW and 1.3 GHz pulsed CW with 0.25 percent duty cycle. The miniature DC motor was operated at maximum distances from the transmitting horn as shown in Table 13. At the maximum operating distance, a measurement of microwave field strength was conducted using an Electromagnetic Radiation Monitor (Narda Model 8616) and Isotropic Probe (Narda Model 8623D). The isotropic probe was able to measure field power densities up to 100 mw/cm². The distances shown in Table 13 are located closer than the minimum far field distance of the transmitting horn antenna and therefore the MAV can be considered to be within the near field of the horn antenna.

MAV Model	Signal	Transmit Power (dBm)	MAV Motor Operating Distance (meters)	Field Strength Measured (mw/cm ²)
MAV-1	1.0 GHz CW	2.50 dBm (1.78 mw)	0.05	0.42
MAV-2	1.3 GHz CW	32.6 dBm (1830 mw)	0.76	0.40
MAV-2	1.3 GHz Pulsed CW Prf=36 kHz;7 us pulse width 25 percent duty cycle	26.4 dBm (440 mw)	-0.05(inside horn)	0.45
MAV-2	1.3 GHz Pulsed CW Prf=13 kHz;7 us pulse width 9 percent duty cycle	1.61 dBm (1.45 mw)	Motor did not operate	N/A
MAV-2	1.3 GHz Pulsed CW Prf=3030 Hz;7 us pulse width 2 percent duty cycle AN/SPS-58 Operating Specs	-4.94 dBm (0.32 mw)	Motor did not operate	N/A

Table 13. MAV WPT Demonstration Summary.

E. CONCLUSIONS AND RECOMMENDATIONS

Wireless power transfer through free space propagation was demonstrated for designs of the MAVs that operated at 1.0 GHz and 1.3 GHz. It was observed that a minimum power density of 0.40 mw/cm^2 at the MAV location was generally needed to start and operate the miniature DC motor of the MAV model. For the present demonstration this power density could not be achieved in the far field, however, using higher power amplification or combining multiple sources may provide the required power density at distances in the far field of the transmission antenna.

Far field WPT operation of the MAV-2 model may be achieved by using the AN/SPS-58 air search radar transmitter and antenna. The AN/SPS-58 radar transmitter characteristics are shown in Table 14. The calculated MAV-2 operating distances from the AN/SPS-58 radar antenna are shown in Figure 76 with a line illustrating the maximum power available from the radar transmitter. These calculations were done by a MathCad spreadsheet and are attached as Appendix G. From the graph of Figure 76, MAV-2 may operate to a range of 28 meters using the AN/SPS-58 radar transmitter and antenna system as a source.

Frequency (GHz)	Pulse Width (uS)	Pulse Repetition (Hz)	Duty Cycle (percent)	Peak Power (watts)	Average Power (watts)	Antenna Gain (dB)
1.3	7	3048	2.1	12 kW	260	23

Table 14. AN/SPS-58 Air Search Radar Transmitter Specifications.

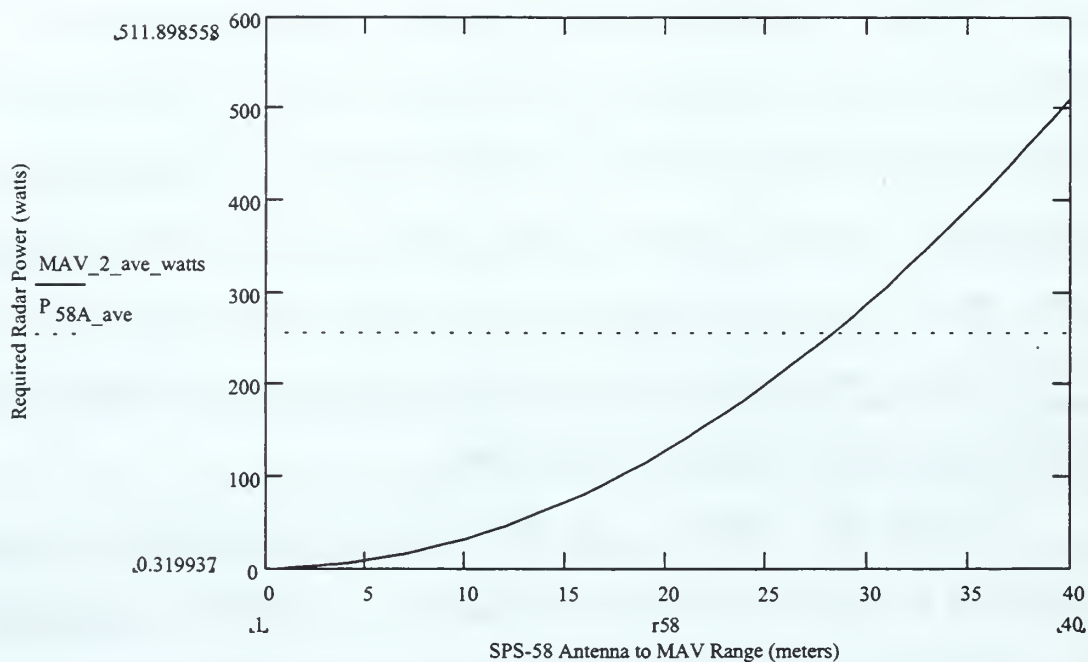


Figure 76. MAV-2 Required Transmitter Power verses Distance From Source Antenna and Available AN/SPS-58 Radar Transmitter Power. MAV_2_ave_watts is the MAV-2 Required Transmitter Power, P58A_ave is the available AN/SPS-58 Radar Transmitter Power.

VI. SUMMARY, CONCLUSIONS, AND RECOMMENDATIONS

A. SUMMARY

A receiving system for wireless power transfer (WPT) to a micro air vehicle (MAV) has been demonstrated using commercially available off the shelf (COTS) hardware. The receiving system was demonstrated to operate at two frequencies, 1.0 GHz and 1.3 GHz with less than 2 watts of transmitted power. Required power density at the MAV was determined to be less than 1 mW to demonstrate operation of a simple DC motor. A novel approach was the use of a semi-omni directional antenna on the MAV, where power can be received at any bearing relative to the MAV. Previous work had concentrated on the use of large highly directional array receiving antennas, which would require a MAV to maintain a particular orientation.

In this thesis, the remotely operated micro air vehicle applications of interest are surveillance and urban warfare. This work could also be applied towards commercial interests, such as the use of RF/Microwave powered identification (RF ID) tags for inventory purposes. WPT could also be used to remotely operate many low powered devices in which the use of on board batteries or power cabling is prohibited.

B. CONCLUSIONS

Wireless power transfer to a remote vehicle is possible and has been demonstrated. Rectifier RF-to-DC conversion achieved a 30 percent efficiency using COTS hardware. Higher efficiencies may be achieved using components with precisely specified characteristics and tight tolerances. These components would include low forward

resistance diodes, such as Schottky GaAs diodes and high dielectric substrates with a controlled relative permittivity.

The limiting factor for MAV range is the amount of RF power density provided at the MAV location. This power density depends upon the transmitter power available and the gain of the transmitting antenna. It is critical that the transmitted power be narrowly confined in a tight beam pattern such that the spot size at the MAV site is not much greater than the MAV itself. If this is the case, then much of the power will be absorbed by the MAV antenna and converted to DC to power the MAV. Generally the larger the antenna gain, the greater its size. Therefore transmitting antennas would likely be large. Fractal techniques, however, may allow the design of smaller antennas [Ref 24].

Deploying multiple transmitter sites and combining the power at the MAV location could reduce the need for a large transmitting antenna. Power levels would likely fluctuate as some beams become blocked by obstacles or otherwise disturbed by the propagation path. Reference 23 discusses the possibility of coherently combining the received power at the MAV through a technique called “beam tagging.” The beam tagging technique would provide a stable maximum power at the MAV. Beam tagging requires feedback from the MAV to the source transmitters and would add some complexity to the system. However, if WPT is used solely to recharge an on-board battery, power fluctuations could be tolerated by the MAV, and the need for a beam tagging system reduced.

C. SUGGESTIONS FOR FURTHER RESEARCH

The following areas are suggested for further investigation in order to provide more efficient WPT to a MAV and reduce the weight of the MAV.

1. GaAs Schottky-barrier Diodes

This thesis concentrated on using the Hewlett Packard HSMS-2825 Silicon Schottky-barrier diode in a surface mount package. It is well known that gallium arside Schottky-barrier diodes (GaAs SBD) can provide a quicker diode with larger reverse current blockage. The potential for greater RF-to-DC conversion efficiency exists when using GaAs technology. The drawback to using GaAs is the cost and the possibility of easier destruction of the semiconductor device either by high power microwave heating or by electro-static discharge. Although silicon devices can also be affected by heating and static discharge, silicon is not as sensitive to these effects. This thesis did not investigate the use of GaAs diodes.

2. Additional Rectifier Circuit Configurations

Experiments and studies in Chapter IV indicated that multiple diodes be used in parallel to provide high RF-to-DC conversion efficiency over a wider dynamic input power range. In this thesis, a single Si-SBD SMT package was used that contained two diodes in parallel. In order to place additional diodes in parallel, power splitting would have been required in order to split the input RF power to the multiple diode packages. Other means to achieve this without a power splitter requires that additional diodes be packaged in the same SMT package or that much smaller packages be available.

An additional recommendation is to use a filter capacitor on the output side of the SBD rectifier circuit. As discussed in Chapter IV, an output filter capacitor may increase the RF-to-DC rectification efficiency. This was experimentally shown for input signals, such as the pulsed CW input signals from a radar transmitter. Design of the filter capacitor with the

DC motor or battery loading could be achieved for greatest RF-to-DC conversion at the transmitting frequency.

3. High Powered Sources

The WPT demonstration presented in this thesis was limited in the distance of MAV operation from the transmitting antenna. This limitation was due to the amount of transmitter power that could be obtained from the amplifier available. Increased MAV operation range could be demonstrated using a higher power source. Suggested sources may include the AN/SPS-58 air search radar; however, it was shown earlier that the low duty cycle of the pulsed CW signal significantly reduces the average signal power for a extremely high peak power level.

Another potential transmitter source may be to use a very high power CW amplifier. One such amplifier would be the Model 200T1G2 power amplifier available from Amplifier Research of Souderton, PA. This power amplifier has an average power rating of 200 watts CW over a frequency band of 1 to 2 GHz. According to Chapter V (Table 9 and Figure 63), the increase in power is projected to power MAV operation 10 meters away from the Microline/FXR transmitting horn.

A third possibility would be to demonstrate lower range MAV operation by using an US Navy fleet operational radar that could support high duty cycles. One such system is the AEGIS/SPY-1 Radar System.

4. MAV Antenna Improvements

This thesis concentrated on developing a WPT demonstrator without regard to the weight of the vehicle. Depositing a thin metal film or applying a conductive coating onto a carbon fiber MAV body can yield a truly lightweight antenna. Lutronix has produced

several carbon fiber MAV bodies. Appendix H lists companies that could apply conductive coatings or deposit thin metal films to a carbon fiber MAV body. Usually these coatings or films are applied to shield plastic enclosed equipment from EMI. The manufacturers have recommended using silver coating with a uniform 0.030 mm dry film thickness.

The as-built MAV copper antennas for this WPT demonstration were not optimized for impedance matching as determined in the GNEC[®] simulations of Chapter III. It is recommended that additional copper antennas be fabricated using the geometry of the GNEC[®] simulations of Chapter III. These additional antennas would be measured for input impedance and the best geometry selected. This optimum geometry would be used as the basis for depositing a thin metal film on a carbon fiber body. Evaluation of input impedance would determine if the carbon fiber and thin film have a significant effect on antenna properties.

5. Improved MAV DC Motor

The demonstration DC motor used is an inexpensive hobby motor with very low torque and was likely to have low efficiency. Highly efficient, precision micro-motors that can operate at high speed are available at a cost of roughly \$200. One such DC motor is the RE010-17 series rare Earth DC motor from Maxon Precision Motors of Burlingame, CA. This motor at 10 mm in diameter and 27 mm long is significantly smaller than the demonstration motor used. Due to its use of rare Earth Neodymium (NdFe) magnets, sinter sleeve bearings and a planetary gearhead, this motor would likely have higher power efficiency. The proposed motor operates at 19,000 rpm with an input power of less than 0.75 watt. Use of such a motor would obtain additional weight savings over the DC motor

used in this demonstration and could achieve enough rotor speed to provide lift to a helicopter type MAV.

D. OTHER POTENTIAL INVESTIGATIONS

During microstrip rectifier testing, a significant power level for the second harmonic of the transmitted signal was observed to originate from the diode. This effect is well known and is sometimes used to form a frequency doubler. An operational MAV would need to communicate back to the control station, and this second harmonic could be used to transmit data from the MAV to the control station. This data could include information, such as video and perhaps information for intelligent transmitter power management.

APPENDIX A. EEsof LIBRA[®] CIRCUIT MODEL TO DETERMINE PERMITTIVITY OF FR-4 PC BOARD

Figure 77 presents the EEsof Libra[®] circuit model used to determine the relative permittivity (ϵ_r) value for the FR-4 PC board material used to manufacture the microstrip rectifier circuits. This circuit was designated Circuit 3-1. Libra[®] simulations were conducted and compared to VNA measurements of Circuit 3-1 in Chapter II.

```

!   SCCS file /home/emag1/vitale/EEsof/libra30/ckt3-1.ckt
!   LIBRA CIRCUIT FILE
!
!   Microstrip Through for WPT-MRPV Project
!   file reentered by hand after emag1 disk crash
!
!   BY:      R.L. Vitale
!   Date:    5/30/97  1746hrs
!   Ckt:     FR-4 PC Board Microstrip transmission line
!           through line to determine er of PCB from Physics Dept
!   Using PC Board Circuit 3-1, manufactured by NPS Physics Dept
!   robotics lab.  Circuit dimensions are
!
!   Microstrip width = 155 mils
!   Microstrip Length = 4365 mils
!   PCB Thickness    = 63 mils
DIM
RES OH
IND NH
CAP PF
COND /OH
FREQ GHZ
PWR DBM
VOL V
CUR MA
LNG MIL
TIME PS
ANG DEG
VAR
EQN
CKT
  MSUB  ER=5.2  H=63  T=1.4  RHO=0.84  RGH=0
  COAX  1  2  0  0  DI=39.4  DO=177.1  L=196.8  ER=2.1  TAND=0.002  RHO=1
  COAX  2  3  0  0  DI=114.2  DO=177.1  L=177.1  ER=1  TAND=0.002  RHO=1
  MLIN  3  4  W=155  L=4365  ! input microstrip
  COAX  4  5  0  0  DI=114.2  DO=177.1  L=177.1  ER=1  TAND=0.002  RHO=1
  COAX  5  6  0  0  DI=39.4  DO=177.1  L=196.8  ER=2.1  TAND=0.002  RHO=1
  DEF2P 1  6  Ckt3-1

```

Figure 77. EEsof Libra[®] Circuit File for Sample Microstrip (Circuit 3-1).

```

TERM
PROC
MODEL
SOURCE
DCTR
    dctr1
    dctr2
FREQ
    SWEEP    0.8  2.8  0.02

POWER
FILEOUT
! S-parameter data to output file "Circuit3-1.s2p"
    Ckt3-1 TS SPAR Ckt3-1-52

OUTVAR
OUTEQN
OUT
    Ckt3-1 MAG[Z1]      SCN      ! Impedance to screen
    Ckt3-1 S11          SC2      ! Smith Chart
    Ckt3-1 DB[S11]      GR1      ! Return Loss for through microstrip
    Ckt3-1 DB[S21]      GR1      ! Transmission for Diode
    Ckt3-1 ANG[S11]     GR2
    Ckt3-1 ANG[S21]     GR2

GRID
! freq
    RANGE    0.8      2.8      0.2      ! GHz
! magnitude
    GR1      -50.0    0.0      5.0      ! Db

```

Figure 77. EEsoft Libra® Circuit File for Sample Microstrip (Circuit 3-1) (continued).

APPENDIX B. MICROSTRIP LINE WIDTH CALCULATIONS

Figure 79 presents a MathCad® spreadsheet used to calculate the microstrip line width required for a characteristic impedance of 50 ohms. A relative permittivity of 4.8 was used. This value was the experimentally determined value for the fiberglass FR-4 PC board used as the material to manufacture the microstrip rectifier circuits. A simple 50 ohm transmission through line was designed and designated as Circuit 4-1. Libra® simulations were conducted and compared to VNA measurements of Circuit 4-1 in Chapter II.

**1: Calculations of Microstrip Line Width,
Effective Relative Permittivity and Line Impedance**

MAV Rectifier Circuit Design Parameters

Desired Characteristic Impedance: $Z_{0m} := 50$ ohms
Desired Operating Frequency: $f_0 := 1$ GHz

Material Parameters

Substrate Thickness: $thick := \frac{1}{16}$ $d := thick \cdot 1000$ $d = 62.5$ mils
Dielectric Constant: $\epsilon_r := 4.8$ *experimentally determined.
Material is precoated,
fiberglass epoxy PC Board
(FP4 Type).*

Other Parameters

complex number: $j := (-1)^{0.5}$
Free space velocity (GHz): $c := 3 \cdot 10^8$ $cGHz := \frac{c}{1 \cdot 10^9}$ $cGHz = 0.3$

1A: Determine W/d ratio for 50 ohm microstrip line (Posar 4.206)

equation constants:

$$A := \frac{Z_{0m}}{60} \cdot \sqrt{\frac{\epsilon_r + 1}{2}} + \frac{\epsilon_r - 1}{\epsilon_r + 1} \cdot \left(0.23 + \frac{0.11}{\epsilon_r} \right) \quad B := \frac{377 \cdot \pi}{2 \cdot Z_{0m} \cdot \sqrt{\epsilon_r}}$$

for $W/d < 2$

$$W_{over_d} := \frac{8 \cdot e^A}{e^{2 \cdot A} - 2}$$

for $W/d > 2$

$$W_{over_d} := \frac{2}{\pi} \cdot \left[B - 1 - \ln(2 \cdot B - 1) + \frac{\epsilon_r - 1}{2 \cdot \epsilon_r} \cdot \left(\ln(B - 1) + 0.39 - \frac{0.61}{\epsilon_r} \right) \right]^2$$

$W_{over_d} = 1.79$ *thus equation for $W/d < 2$ is used.*

Figure 78. Microstrip Width Calculations.

1B: Determine effective permittivity for microstrip line (Posar)

Effective Dielectric Constant
(relative permittivity)
for 50 Ω Microstrip Line

$$\epsilon_e := \frac{\epsilon_r + 1}{2} + \frac{\epsilon_r - 1}{2} \cdot \frac{1}{\sqrt{1 + 12 \cdot \frac{1}{W_{\text{over}_d}}}}$$

$$\epsilon_e = 3.585$$

1C: Determine guide wavelength (at desired frequency) for microstrip line

Velocity of propagation: $v_p := \frac{c \text{GHz}}{\epsilon_e^{0.5}}$

Guide Wavelength in mils: $\lambda_{\text{ustrip}} := \frac{v_p}{f_0} \cdot \left(\frac{100}{1} \right) \cdot \left(\frac{1}{2.54} \right) \cdot \left(\frac{1000}{1} \right)$

$$\lambda_{\text{ustrip}} = 6.238 \cdot 10^3 \text{ mils}$$

Half Wavelength in mils: $L := \frac{\lambda_{\text{ustrip}}}{2} \quad L = 3.119 \cdot 10^3 \text{ mils}$

1E. Measurements for 50 ohm microstrip line and check on Impedance

Width := $W_{\text{over}_d} \cdot d$ Width = 111.896 mils

$$\lambda_{\text{ustrip}} = 6.238 \cdot 10^3 \text{ mils}$$

Impedance Check (Posar 4.205 for $W/d < 1$)

$$Z_{0\text{ustrip}} := \frac{60}{\sqrt{\epsilon_e}} \cdot \ln \left(\frac{8 \cdot d}{\text{Width}} + \frac{\text{Width}}{4 \cdot d} \right) \quad Z_{0\text{ustrip}} = 50.467 \text{ ohms}$$

Figure 78. Microstrip Width Calculations (Continued).

APPENDIX C. EEsof LIBRA[®] CIRCUIT MODEL FOR MICROSTRIP THROUGH LINE

Figure 79 presents the EEsof Libra[®] circuit model developed to simulate the 50 ohm microstrip line fabricated from FR-4 PC Board material with an unknown permittivity. This circuit was designated Circuit 4-1. Libra[®] simulations were conducted and compared to VNA measurements of Circuit 4-1 in Chapter II.

```

!   SCCS file /home/emag1/vitale/EEsof/libra30/ckt4-1.ckt
!   LIBRA CIRCUIT FILE
!   Microstrip Through for WPT-MRPV Project
!   file reentered by hand after emag1 disk crash
!   BY:      R.L. Vitale
!   Date:    6/5/97  1746hrs
!   Ckt:     FR-4 PC Board Microstrip transmission line
!   50 ohm transmission line

!   Using PC Board Circuit 4-1, manufactured by NPS Physics Dept
!   robotics lab.  Circuit dimensions are
!   Microstrip width  =   105 mils
!   Microstrip Length =  4325 mils
!   PCB Thickness     =    63 mils

DIM
RES OH
IND NH
CAP PF
COND /OH
FREQ GHZ
PWR DBM
VOL V
CUR MA
LNG MIL
TIME PS
ANG DEG

VAR
EQN
CKT
  MSUB  ER=4.8  H=63  T=1.4  RHO=0.84  RGH=0
  COAX  1  2  0  0  DI=39.4  DO=177.1  L=196.8  ER=2.1  TAND=0.002  RHO=1
  COAX  2  3  0  0  DI=114.2  DO=177.1  L=177.1  ER=1  TAND=0.002  RHO=1
  MLIN  3  4      W=105  L=4325      ! input microstrip
  COAX  4  5  0  0  DI=114.2  DO=177.1  L=177.1  ER=1  TAND=0.002  RHO=1
  COAX  5  6  0  0  DI=39.4  DO=177.1  L=196.8  ER=2.1  TAND=0.002  RHO=1
  DEF2P 1  6      Ckt4-1

```

Figure 79. EEsoft Libra[®] Circuit Model for FR-4 Microstrip Through Line.

```

TERM

PROC
MODEL
SOURCE
DCTR
    dctr1
    dctr2
FREQ
    SWEEP    0.8  2.5  0.01
POWER
FILEOUT
! S-parameter data to output file "Circuit4-1-xx.s2p"
    Ckt4-1 TS SPAR Ckt4-1-48
OUTVAR
OUTEQN
OUT
    Ckt4-1 S11          SC2      ! Smith Chart
    Ckt4-1 DB[S11]      GR1      ! Return Loss for through microstrip
    Ckt4-1 DB[S21]      GR1      ! Transmission for Diode
    Ckt4-1 ANG[S11]     GR2
    Ckt4-1 ANG[S21]     GR2
GRID
! freq
    RANGE    0.8      2.5      0.17      ! GHz
! magnitude
    GR1      -50.0    0.0      5.0      ! dB

```

Figure 79. EEsoft Libra[®] Circuit Model for FR-4 Microstrip Through Line (continued).

APPENDIX D. DIODE S-PARAMETER CALCULATIONS

Figure 80 presents a MathCad® spreadsheet used to calculate the S-parameters of the SMT-SBD package. Calculations shift the reference planes of VNA measurements done on the diode test fixture (Circuit 4-2). A relative permittivity of 4.8 was used which was the experimentally determined value for the fiberglass FR-4 PC board used as the material to manufacture the microstrip rectifier circuits.

A. Fabricate test fixture, measure input & output microstrip line lengths.

MRPV Fixture 4-2 was fabricated to measure the S parameters of the HP Schottky-barrier diode package. Fixture 4-2 is a microstrip fixture made from FR-4 Fiberglass epoxy PC board material with SMA connectors for interface to the vector network analyzer. Input and output microstrip lines are 110 mils in width and have lengths $Lin = dis_{port1}$ (mils) and $Lout = dis_{port2}$ (mils).

The shift in reference planes (from Fixture 4-2 connectors to Schottky diode) is calculated and applied to the measured S parameters of Fixture 4-2 to determine the S parameters of the HSMS-2825 silicon Schottky-barrier diode package.

$dis_{port1} := 2725 + 316$	mils	<i>distance = ustrip + connector dist measured using calipers (form MRPV Fixture 4-2)</i>
$dis_{port2} := 1508 + 350$	mils	

MRPV Rectifier Circuit Design Parameters

Desired Characteristic Impedance:	$Z_{0m} := 50$	ohms
Desired Operating Frequency:	$f_0 := 1$	GHz

Material Parameters

Substrate Thickness:	$thick := \frac{1}{16}$	$d := thick \cdot 1000$ $d = 62.5$ mils
Dielectric Constant:	$\epsilon_r := 4.8$	from previous work, this value was experimentally determined. Material is precoated, fiberglass epoxy PC Board (FP4 Type).

Other Parameters

complex number:	$j := (-1)^{0.5}$	
Free space velocity (GHz):	$c := 3 \cdot 10^8$	$cGHz := \frac{c}{1 \cdot 10^9}$ $cGHz = 0.3$

Figure 80. Calculations of SMT-SBD Package S parameters.

B: Determine W/d for 50 ohm microstrip line (Posar 4.206)

equation constants:

$$A := \frac{Z_{0m}}{60} \cdot \sqrt{\frac{\epsilon_r + 1}{2}} + \frac{\epsilon_r - 1}{\epsilon_r + 1} \cdot \left(0.23 + \frac{0.11}{\epsilon_r} \right) \quad B := \frac{377 \cdot \pi}{2 \cdot Z_{0m} \cdot \sqrt{\epsilon_r}}$$

for W/d < 2

for W/d > 2

$$W_{over_d} := \frac{8 \cdot e^A}{e^{2 \cdot A} - 2} \quad W_{over_d} := \frac{2}{\pi} \cdot \left[B - 1 - \ln(2 \cdot B - 1) + \frac{\epsilon_r - 1}{2 \cdot \epsilon_r} \cdot \left(\ln(B - 1) + 0.39 - \frac{0.61}{\epsilon_r} \right) \right]^2$$

$$W_{over_d} = 1.79$$

thus equation for W/d < 2 is used.

Determine effective permittivity for microstrip line (Posar)

Effective Dielectric Constant
(relative permittivity)
for 50 Ω Microstrip Line

$$\epsilon_e := \frac{\epsilon_r + 1}{2} + \frac{\epsilon_r - 1}{2} \cdot \frac{1}{\sqrt{1 + 12 \cdot \frac{1}{W_{over_d}}}}} \quad \epsilon_e = 3.585$$

Determine guide wavelength (at desired frequency) for microstrip line (Posar)

Velocity of propagation:

$$v_p := \frac{cGHz}{\epsilon_e^{0.5}}$$

Guide Wavelength in mils:

$$\lambda_{ustrip} := \frac{v_p}{f_0} \cdot \left(\frac{100}{1} \right) \cdot \left(\frac{1}{2.54} \right) \cdot \left(\frac{1000}{1} \right)$$

$$\lambda_{ustrip} = 6.238 \cdot 10^3 \quad \text{mils}$$

Figure 80. Calculations of SMT-SBD Package S parameters (Continued).

B. Measure the S parameters of MRPV Fixture 4-2 using VNA

S parameter measurements of MPRV diode fixture 4-2. S parameters are measured at the ports of the board by a Hewlett Packard HP8510 Vector Network Analyzer. Measurements are dated 12/24/96. 1st Column is magnitude (dB), 2nd is phase in degrees

freq (GHz)	Log Mag	Phase	Log Mag	Phase	Log Mag	Phase	Log Mag	Phase
	F _{11_port1} :=		S' ₁₁ :=		S' ₁₂ :=		S' ₂₁ :=	
							S' ₂₂ :=	
0.80	-2.15	52.83	-5.09	178.68	-5.25	179.07	-2.14	125.35
0.86	-2.25	29.40	-4.88	157.16	-4.91	156.68	-2.36	105.10
0.93	-2.55	5.16	-4.42	134.21	-4.46	133.78	-2.66	83.76
1.00	-2.87	-18.34	-4.04	111.64	-4.24	112.06	-2.85	63.55
1.07	-3.09	-40.64	-3.87	90.42	-3.99	90.45	-3.05	43.33
1.14	-3.42	-63.24	-3.63	68.80	-3.69	68.58	-3.36	22.72
1.20	-3.89	-86.63	-3.28	46.51	-3.43	46.88	-3.66	2.66
1.27	-4.21	-109.36	-3.14	25.56	-3.30	26.15	-3.83	-16.01
1.34	-4.56	-132.75	-3.00	4.57	-3.05	4.52	-4.20	-35.40
1.41	-5.17	-157.94	-2.71	-17.67	-2.80	-17.35	-4.63	-54.13
1.48	-5.62	176.67	-2.54	-39.16	-2.64	-38.65	-4.93	-71.65
1.54	-5.94	150.85	-2.45	-60.18	-2.50	-60.16	-5.28	-88.96
1.61	-6.30	124.16	-2.32	-81.70	-2.37	-81.54	-5.62	-105.55
1.68	-6.61	97.02	-2.21	-103.28	-2.28	-102.98	-5.89	-121.74
1.75	-6.70	70.79	-2.18	-124.18	-2.22	-124.18	-6.14	-137.82
1.82	-6.91	44.73	-2.10	-145.61	-2.16	-145.56	-6.40	-154.12
1.88	-7.07	19.50	-2.06	-166.78	-2.13	-166.60	-6.63	-170.56
1.95	-7.23	-4.56	-2.01	172.25	-2.09	172.40	-6.86	172.53
2.02	-7.62	-28.30	-1.93	150.88	-2.04	151.29	-7.23	154.95
2.09	-7.88	-50.38	-1.90	130.25	-1.99	130.69	-7.55	136.99
2.16	-8.26	-71.85	-1.84	109.59	-1.94	110.11	-7.96	118.70
2.22	-8.63	-92.94	-1.80	89.22	-1.89	89.73	-8.37	99.97
2.29	-9.32	-113.95	-1.73	68.30	-1.81	68.84	-9.02	80.54
2.36	-10.08	-135.14	-1.67	47.42	-1.74	48.02	-9.71	60.83
2.43	-10.90	-156.62	-1.60	26.49	-1.68	27.06	-10.52	41.04
2.50	-11.80	-178.30	-1.56	5.56	-1.63	6.13	-11.32	21.36

Figure 80. Calculations of SMT-SBD Package S parameters (Continued).

Part 3: Determine the S parameters for Hewlett Packard Schotky Diode by shifting reference planes

$$m := 1.. \text{length}(F_{11_port1}) \quad n := 1.. 2 \quad \text{Input_power} := 15 \text{ dBm} \quad \beta_{\text{ustrip}} := \frac{2 \cdot \pi}{\lambda_{\text{ustrip}}}$$

Find shift in reference plane(s) and then apply to measured data to get approximate S values for the Schotky Diode at the input power level used (10dBm). S parameters may however change depending upon the input power level.

Guide wavelength λ_g in microstrip
for frequencies measured:

Wavenumber β)

$$\lambda_{\text{sweep_ustrip } m, 1} := \frac{\text{cGHz}}{F_{11_port1_m, 1} \cdot \epsilon_e^{0.5}} \cdot \frac{1}{1} \cdot \frac{1000}{2.54} \cdot \frac{1}{1} \quad \beta_{\text{sweep_ustrip } m, 1} := \frac{2 \cdot \pi}{\lambda_{\text{sweep_ustrip } m, 1}}$$

Electrical length of input and output microstrip lines, convert to degrees

$$\theta_{1m} := \left(\text{dist_port1} \cdot \beta_{\text{sweep_ustrip } m, 1} \right) \cdot \frac{180}{\pi}$$

$$\theta_{2m} := \left(\text{dist_port2} \cdot \beta_{\text{sweep_ustrip } m, 1} \right) \cdot \frac{180}{\pi}$$

$$F_{11_port1} =$$

$$\theta_1 =$$

$$\theta_2 =$$

θ_1 is the shift on input line

where

θ_2 is the shift on the output line

F_{11_port1} are the operating frequencies

0.800	140.392	85.777
0.860	150.921	92.210
0.930	163.205	99.716
1.000	175.490	107.221
1.070	187.774	114.727
1.140	200.058	122.232
1.200	210.588	128.665
1.270	222.872	136.171
1.340	235.156	143.676
1.410	247.440	151.182
1.480	259.725	158.687
1.540	270.254	165.121
1.610	282.538	172.626
1.680	294.823	180.132
1.750	307.107	187.637
1.820	319.391	195.143
1.880	329.920	201.576
1.950	342.205	209.081
2.020	354.489	216.587
2.090	366.773	224.092
2.160	379.058	231.598
2.220	389.587	238.031
2.290	401.871	245.537
2.360	414.155	253.042
2.430	426.440	260.548
2.500	438.724	268.053

Figure 80. Calculations of SMT-SBD Package S parameters (Continued).

S Parameters of diode inferred by shifting reference plane

Same Magnitudes

New Angles

$$S_{11m,1} := S'_{11m,1}$$

$$S_{11m,2} := S'_{11m,2} + 2 \cdot \theta_{1m}$$

$$S_{12m,1} := S'_{12m,1}$$

$$S_{12m,2} := S'_{12m,2} + 2 \cdot (\theta_{1m} + \theta_{2m})$$

$$S_{21m,1} := S'_{21m,1}$$

$$S_{21m,2} := S'_{21m,2} + 2 \cdot (\theta_{1m} + \theta_{2m})$$

$$S_{22m,1} := S'_{22m,1}$$

$$S_{22m,2} := S'_{22m,2} + 2 \cdot \theta_{2m}$$

S Parameters at Diode, use in Touchstone/Libra Program

F _{11_port1} =	0.80	S ₁₁ =	-2.15 333.61	S ₁₂ =	-5.09 631.02	S ₂₁ =	-5.25 631.41	S ₂₂ =	-2.14 296.90
	0.86		-2.25 331.24		-4.88 643.42		-4.91 642.94		-2.36 289.52
	0.93		-2.55 331.57		-4.42 660.05		-4.46 659.62		-2.66 283.19
	1.00		-2.87 332.64		-4.04 677.06		-4.24 677.48		-2.85 277.99
	1.07		-3.09 334.91		-3.87 695.42		-3.99 695.45		-3.05 272.78
	1.14		-3.42 336.88		-3.63 713.38		-3.69 713.16		-3.36 267.18
	1.20		-3.89 334.55		-3.28 725.02		-3.43 725.39		-3.66 259.99
	1.27		-4.21 336.38		-3.14 743.65		-3.30 744.24		-3.83 256.33
	1.34		-4.56 337.56		-3.00 762.23		-3.05 762.18		-4.20 251.95
	1.41		-5.17 336.94		-2.71 779.57		-2.80 779.89		-4.63 248.23
	1.48		-5.62 696.12		-2.54 797.66		-2.64 798.17		-4.93 245.72
	1.54		-5.94 691.36		-2.45 810.57		-2.50 810.59		-5.28 241.28
	1.61		-6.30 689.24		-2.32 828.63		-2.37 828.79		-5.62 239.70
	1.68		-6.61 686.67		-2.21 846.63		-2.28 846.93		-5.89 238.52
	1.75		-6.70 685.00		-2.18 865.31		-2.22 865.31		-6.14 237.45
	1.82		-6.91 683.51		-2.10 883.46		-2.16 883.51		-6.40 236.17
	1.88		-7.07 679.34		-2.06 896.21		-2.13 896.39		-6.63 232.59
	1.95		-7.23 679.85		-2.01 1.27•10 ³		-2.09 1.27•10 ³		-6.86 590.69
	2.02		-7.62 680.68		-1.93 1.29•10 ³		-2.04 1.29•10 ³		-7.23 588.12
	2.09		-7.88 683.17		-1.90 1.31•10 ³		-1.99 1.31•10 ³		-7.55 585.17
	2.16		-8.26 686.27		-1.84 1.33•10 ³		-1.94 1.33•10 ³		-7.96 581.90
	2.22		-8.63 686.23		-1.80 1.34•10 ³		-1.89 1.34•10 ³		-8.37 576.03
	2.29		-9.32 689.79		-1.73 1.36•10 ³		-1.81 1.36•10 ³		-9.02 571.61
	2.36		-10.08 693.17		-1.67 1.38•10 ³		-1.74 1.38•10 ³		-9.71 566.91
	2.43		-10.90 696.26		-1.60 1.40•10 ³		-1.68 1.40•10 ³		-10.52 562.14
	2.50		-11.80 699.15		-1.56 1.42•10 ³		-1.63 1.42•10 ³		-11.32 557.47

Figure 80. Calculations of SMT-SBD Package S parameters (Continued).

APPENDIX E. Si-SBD MODEL FILE FOR LIBRA[®]

This S parameter data file was used as a component in EEsof Libra[®] microwave circuit simulations to aid the design of impedance matching required for the Si-SBD rectifier circuit. The Hewlett Packard HSMS-2825 dual surface mount Schottky-barrier diode package is described.

```
! FILENAME:      hpdiodel.s2p Version: 1.1
! P/N:  HP Schottky Diode,

!   By:  R.L. Vitale   Date:  5/30/97  18:04
!   Reentered - original lost when emag1 crashed

! BIAS CONDITIONS:  none
! NOTE:  S-Parameters determined by VNA measuremnts with a reference
!        Plane shift then applied.  Numbers obtained from MathCad Spreadsheet
!        dated 1/16/97
!        VNA measurements taken on MRPV Diode Fixture 4-2.

! symbol  freq-unit  parameter-type  data-format  keyword  impedance-ohms
!   #      GHZ      S          DB          R          50

!   freq  dBS11  ANGS11 dBS12  ANGS12 dBS21  ANGS21 dBS22  ANGS22
0.80  -2.15  333.61 -5.09  631.02 -5.25  631.41 -2.14  296.90
0.86  -2.25  331.24 -4.88  643.42 -4.91  642.94 -2.36  289.52
0.93  -2.55  331.57 -4.42  660.05 -4.46  659.62 -2.66  283.19
1.00  -2.87  332.64 -4.04  677.06 -4.24  677.48 -2.85  277.99
1.07  -3.09  334.91 -3.87  695.42 -3.99  695.45 -3.05  272.78
1.14  -3.42  336.88 -3.63  713.38 -3.69  713.16 -3.36  267.18
1.20  -3.89  334.55 -3.28  725.02 -3.43  725.39 -3.60  259.99
1.27  -4.21  336.38 -3.14  743.65 -3.30  744.24 -3.83  256.33
1.34  -4.56  337.56 -3.00  762.23 -3.05  762.18 -4.20  251.95
1.41  -5.17  336.94 -2.71  779.57 -2.80  779.89 -4.63  248.23
1.48  -5.62  696.12 -2.54  797.66 -2.64  798.17 -4.93  245.72
1.54  -5.94  691.36 -2.45  810.57 -2.50  810.59 -5.28  241.28
1.61  -6.30  689.24 -2.32  828.63 -2.37  828.79 -5.62  239.70
1.68  -6.61  686.67 -2.21  846.63 -2.28  846.93 -5.89  238.52
1.75  -6.70  685.00 -2.18  865.31 -2.22  865.31 -6.14  237.45
1.82  -6.91  683.51 -2.10  883.46 -2.16  883.51 -6.40  236.17
1.88  -7.07  679.34 -2.06  896.21 -2.13  896.39 -6.63  232.59
1.95  -7.23  679.85 -2.01  1270.0 -2.09  1270.0 -6.86  590.69
2.02  -7.62  680.68 -1.93  1290.0 -2.04  1290.0 -7.23  588.12
2.09  -7.88  683.17 -1.90  1310.0 -1.99  1310.0 -7.55  585.17
2.16  -8.26  686.27 -1.84  1330.0 -1.94  1330.0 -7.96  581.90
2.22  -8.63  686.23 -1.80  1340.0 -1.89  1340.0 -8.37  576.03
2.29  -9.32  689.79 -1.73  1360.0 -1.81  1360.0 -9.02  571.61
2.36  -10.08 693.17 -1.67  1380.0 -1.74  1380.0 -9.71  566.91
2.43  -10.90 696.26 -1.60  1400.0 -1.68  1400.0 -10.52 562.14
2.50  -11.80 699.15 -1.56  1420.0 -1.63  1420.0 -11.32 557.47
```

Figure 81. EEsof Libra[®] Model for HP HSMS-2825 Si-SBD.

APPENDIX F. EEsof LIBRA[®] CIRCUIT MODEL FOR MICROSTRIP RECTIFIER CIRCUIT

Figure 82 presents the EEsof Libra[®] circuit model developed to simulate the microstrip rectifier circuit using a 2-port S parameter input file and the characteristics of the FR-4 PC Board with permittivity determined through VNA measurement and Libra[®] simulations. This circuit was designated Circuit 4-2. Libra[®] simulations were conducted and compared to VNA measurements of Circuit 4-2 in Chapter II.

```

!   SCCS file /home/emagl/vitale/EEsof/libra30/fix4_2.ckt
!   LIBRA CIRCUIT FILE
!       Microstrip Shotkey Diode Circuit for WPT-MRPV Project
!       Model of Circuit 4-2 constructed after buildout.!
!       BY:      R.L. Vitale
!       Date:    7/10/97  1430hrs
!       Ckt:     HP Schotkey Surface Mount Diode mounted on
!               50 ohm FR-4 PC Board Microstrip transmission line.
!       Microstrip Schotkey Diode using data from VNA measurements on
!       Fixture 4-2 and calculating S parameters from shifting the
!       reference plane.  Calculations done using Mathcad spreadsheet
!       dated 1/16/97.
!       HP Schotkey Diode S Paramenter file:  hpdiodel.s2p
DIM
RES OH
IND NH
CAP PF
COND /OH
FREQ GHZ
PWR DBM
VOL V
CUR MA
LNG MIL
TIME PS
ANG DEG
VAR
EQN
CKT
  MSUB  ER=4.8  H=70  T=1.4  RHO=0.84  RGH=0
  COAX  1  2  0  0  DI=39.4  DO=177.1  L=196.8  ER=2.1  TAND=0.002  RHO=1
  COAX  2  3  0  0  DI=114.2  DO=177.1  L=177.1  ER=1  TAND=0.002  RHO=1
  MLIN  3  4          W=105  L=1500          ! input microstrip
  S2P   4  5  0      hpdiodel          ! diode parameter file
  MLIN  5  6          W=105  L=2750          ! Output microstrip line
  DEF2P 1  6          Ckt4_2

```

Figure 82. EEsoft Libra[®] Circuit File, Microstrip Rectifier Circuit (Circuit 4-2).

```

TERM
  Ckt4_2  0.0  0.0  0.0  0.0                ! 50 ohm termination
PROC
MODEL
SOURCE
DCTR
  dctr1
  dctr2

FREQ
  SWEEP    0.8  2.8  0.05

POWER
FILEOUT
OUTVAR
OUTEQN
OUT
  Ckt4_2  S11          SC2      ! Smith Chart
  Ckt4_2  DB[S11]      GR1      ! Return Loss for Circuit 4-2
  Ckt4_2  DB[S21]      GR1      ! Transmission for Circuit 4-2
  Ckt4_2  ANG[S11]     GR2
  Ckt4_2  ANG[S21]     GR2

GRID
!  freq
  RANGE    0.8      2.8      0.2      ! range for plot
  GR1      -20.0    0.0      2.0      ! grid

```

Figure 82. EEsoft Libra® Circuit File, Microstrip Rectifier Circuit (Circuit 4-2) (continued)

APPENDIX G. WPT PROPAGATION CALCULATIONS

Wireless power transfer propagation calculations for MAV using Microline horn antenna and AN/SPS-58 radar transmitter. These calculations were conducted using a MathCad spreadsheet:

- (1) Distance to far field for Microline horn transmit antenna used in low power (MAV-1) WPT demonstrations.
- (2) Transmit power required to operate the MAV at various distances.
- (3) Required average and peak power from AN/SPS-58 radar transmitter at various distances.

(1) Far Field Calculations for Microline/FXR Horn Antenna, used for Low Power Lab Transmission Far Field Calculation

Dimensions of Horn

(Height) $a := 41.2 \text{ cm}$ $A := a \cdot 10^{-2}$ $A = 0.412 \text{ meters}$

(Width) $b := 55.6 \text{ cm}$ $B := b \cdot 10^{-2}$ $B = 0.556 \text{ meters}$

(diagonal) $d := \sqrt{A^2 + B^2}$

Frequencies of Interest

(Velocity) $v_p := 3 \cdot 10^8$

Frequencies $f := \begin{bmatrix} 1.0 \\ 1.3 \end{bmatrix}$ $f := f \cdot 10^9$ $f = \begin{bmatrix} 1 \cdot 10^9 \\ 1.3 \cdot 10^9 \end{bmatrix}$

$$\lambda := \left(\frac{v_p}{f} \right)$$

Wavelengths

Far Field Distance Calculation

$$r_{\text{far_field}} := \frac{2 \cdot d}{\lambda} \quad r_{\text{far_field}} = \begin{bmatrix} 4.613 \\ 5.997 \end{bmatrix} \text{ meters}$$

Antenna Gains

Receiving antennas (MAV) Gains from NEC simulations

$G_{\text{MAV_1GHZ}} := 1.48 \text{ dB}$ $G_{\text{MAV_1.3GHZ}} := 1.67 \text{ dB}$

Transmit Horn Antenna, from published specifications

$G_1 := 15 \text{ dB}$

MAV Recieve Antennas

$$G_2 := \begin{bmatrix} G_{\text{MAV_1GHZ}} \\ G_{\text{MAV_1.3GHZ}} \end{bmatrix} \text{ dB}$$

Required input power to the MAV rectifier to turn the motor determined from rectifier measurements
 Value based on results of testing of circuit 4-2 with small german dc motor (page 23 of lab book). MAV-1.3GHz Value
 based on results from testing of circuit m7d-7 on page 78 of lab book

$$P_{in\ 1GHZ} := 15\ \text{dBm}$$

$$P_{in\ 1.3GHZ} := 15\ \text{dB} \quad P_R := \begin{bmatrix} P_{in\ 1GHZ} \\ P_{in\ 1.3GHZ} \end{bmatrix} \text{dBm}$$

Equation for required transmitted power to turn motor

$$P_{trans} := \left[\frac{(4 \cdot \pi \cdot r_{far_field})^2}{G_1 \cdot G_2 \cdot \lambda^2} \right] \cdot P_R$$

Easier to calculate in dB format calculate distance & frequency

$$\text{constant} \quad K_{dB} := \overrightarrow{\left(20 \cdot \log \left(\frac{4 \cdot \pi \cdot r_{far_field}}{\lambda} \right) \right)}$$

Calculate power required in dBm

$$P_T := K_{dB} + P_R - G_1 - G_2 \quad P_T = \begin{bmatrix} 44.242 \\ 48.61 \end{bmatrix} \text{dBm}$$

Converting to mW and Watts

$$P_{T_mW} := \overrightarrow{\left(\frac{P_T}{10} \right)} \quad P_{T_mW} = \begin{bmatrix} 2.656 \cdot 10^4 \\ 7.261 \cdot 10^4 \end{bmatrix}$$

$$P_{T_W} := \overrightarrow{\left(\frac{P_{T_mW}}{1000} \right)} \quad P_{T_W} = \begin{bmatrix} 26.56 \\ 72.61 \end{bmatrix} \text{watts}$$

(2) Required transmit power for MAV operation.

Calculate the required transmit power for MAV operation at various distances. We will be assuming that the far field radiation equation is being used.

Distances to be used

$$r := (.1 \ .3 \ .5 \ 1 \ 2 \ 4 \ 8 \ 9 \ 10 \ 11 \ 12 \ 13 \ 14 \ 15 \ 16 \ 17 \ 18 \ 19 \ 20 \ 21) \quad r := r^T$$

$$K_{dB_1} := \overrightarrow{\left(20 \cdot \log \left(\frac{4 \cdot \pi \cdot r}{\lambda_1} \right) \right)} \quad \lambda_1 = 0.3$$

$$P_{T1} := K_{dB_1} + P_{R_1} - G_1 - G_{2_1}$$

$$K_{dB_2} := \left(20 \cdot \log \left(\frac{4 \cdot \pi \cdot r}{\lambda_2} \right) \right) \quad \lambda_2 = 0.231$$

$$P_{T2} := K_{dB_2} + P_{R_2} - G_1 - G_{2_2}$$

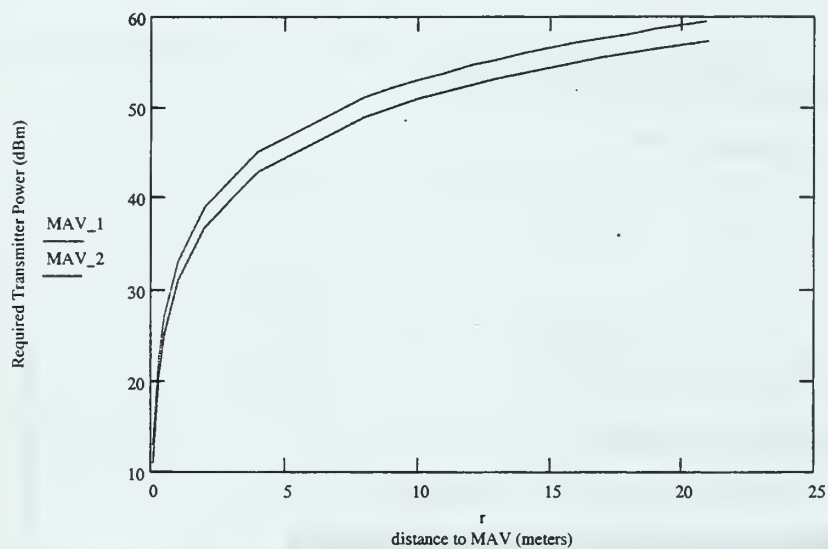
$$P_{T1}^T = \begin{array}{|c|c|c|c|c|c|} \hline 1 & 2 & 3 & 4 & 5 & 6 \\ \hline 10.962 & 20.504 & 24.941 & 30.962 & 36.982 & 43.003 \\ \hline \end{array}$$

$$MAV_1 := P_{T1}$$

$$P_{T2}^T = \begin{array}{|c|c|c|c|c|c|} \hline 1 & 2 & 3 & 4 & 5 & 6 \\ \hline 13.051 & 22.593 & 27.03 & 33.051 & 39.071 & 45.092 \\ \hline \end{array}$$

$$MAV_2 := P_{T2}$$

Plot Required Transmitter Power for Various Distances. Plot assumes that the MAV requires 15 dBm at rectifier to operate motor.



(3) Required Peak Power from AN/SPS-58 Type Radar Transmitter at various distances

Calculate the required transmit power for MAV operation at various distances. We will be assuming that the far field radiation equation is being used. Compare to the output of the AN/SPS-58A Air Search Radar

AN/SPS-58 Transmitter Specifications

Maximum Transmitter Power

$$P_{58A} := 12000 \text{ watts}$$

Pulse Specifications and Duty Cycle

$$\tau := 7 \cdot 10^{-6} \text{ seconds}$$

$$\text{prf} := 3048 \text{ hz}$$

$$\text{duty_cycle} := \tau \cdot \text{prf}$$

$$\text{duty_cycle} = 0.021$$

Frequency & Wavelength

$$f_{\text{mav}_2} := 1.3 \cdot 10^9 \quad \lambda := \frac{3 \cdot 10^8}{f_{\text{mav}_2}} \quad \lambda = 0.231$$

Average Power

$$P_{58A_ave} := P_{58A} \cdot \text{duty_cycle} \quad P_{58A_ave} = 256.032 \text{ watts}$$

Antenna Gain

The SPS-58A uses a C/L Band horn antenna with C-Band reflector. Total Gain for antenna is specified as 23 dB, which is 8dB greater than the Microline/FXR horn used earlier.

$$G_{\text{sps58a}} := 23 \text{ dB}$$

Distances

$$i := 1..40 \quad r_{58}_i := i$$

Constant

$$K_{\text{dB}_{58}} := \left(20 \cdot \log \left(\frac{4 \cdot \pi \cdot r_{58}}{\lambda} \right) \right) \quad \lambda = 0.231$$

Required Average Power from Transmitter (in dBm)

$$P_{\text{T58_ave}} := K_{\text{dB}_{58}} + P_{R_2} - G_{\text{sps58a}} - G_{2_2}$$

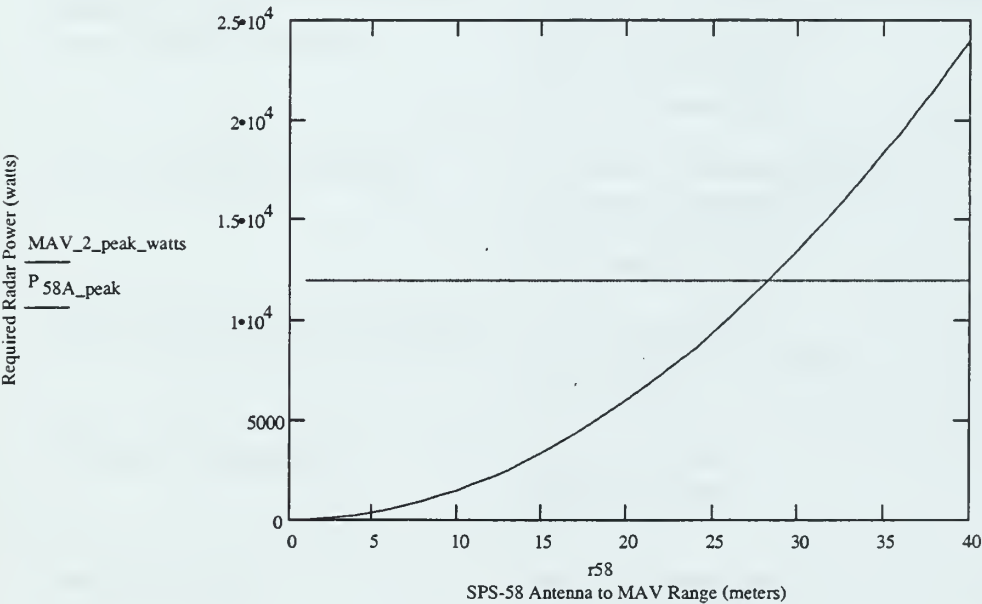
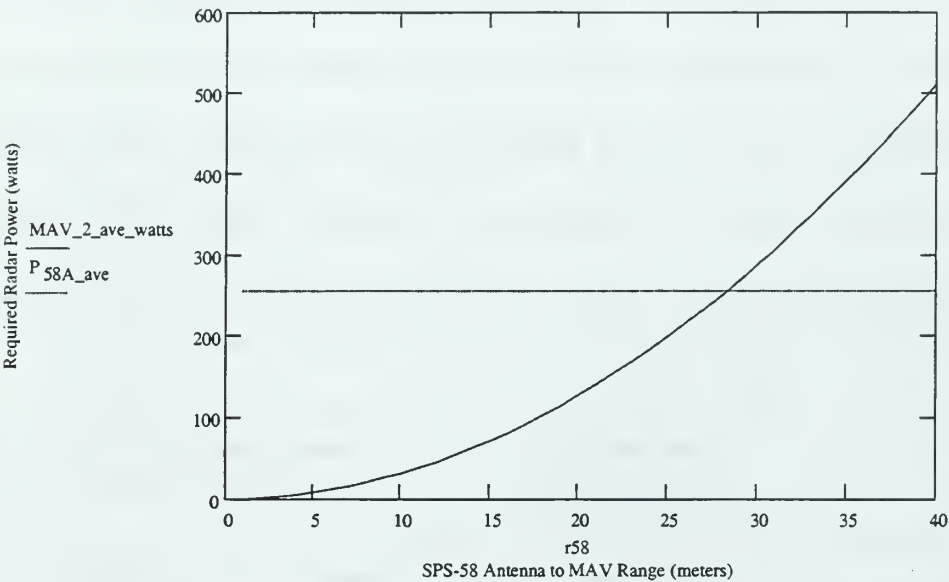
$$P_{\text{T58_ave}}^T = \begin{array}{|c|c|c|c|c|c|c|c|} \hline 1 & 2 & 3 & 4 & 5 & 6 & 7 & 8 \\ \hline 25.051 & 31.071 & 34.593 & 37.092 & 39.03 & 40.614 & 41.953 & 43.112 \\ \hline \end{array} \quad \text{MAV}_2_ave := P_{\text{T58_ave}}$$

Convert average power to average power (watts) and to peak power (watts) for the radar transmitter

$$\text{MAV}_2_ave_watts := \left(\frac{\frac{\text{MAV}_2_ave}{10}}{1000} \right) \quad \text{MAV}_2_peak_watts := \frac{\text{MAV}_2_ave_watts}{\text{duty_cycle}}$$

$$P_{58A_ave}_i := P_{58A_ave} \quad P_{58A_peak} := \frac{P_{58A_ave}}{\text{duty_cycle}}$$

Plot the resulting average and peak pulse power required at various distances from the AN/SPS-58 Radar transmitter antenna in order to operate the MAV. It has been assumed that the MAV requires 15 dBm of power at the rectifier in order to run the rectifier and DC motor combination. AN/SPS-58 average and peak power are plotted for comparison purposes and as a means to determine maximum operating range of the MAV when using the AN/SPS-58 radar transmitter.



APPENDIX H. LISTING OF POTENTIAL CONDUCTIVE COATING OR THIN FILM SUPPLIERS

Table 15 presents a listing of potential suppliers that could help produce a light weight MAV antenna for wireless power transfer. This antenna would be a carbon fiber composite body with a highly conductive metallic outer surface. This conductive outer surface could be applied either by depositing a thin film or by applying a conductive coating. The Lutronix Corporation has produced MAV carbon fiber bodies, the vendors listed in Table 15 would apply the applicable coating or deposit a thin conductive film.

Supplier	Address and Contacts
Conductive Coatings Divisor Chromium Corporation	308 Ellen Trout Lufkin, TX 75904 (409) 633-6387
Thin Film, Vacuum, & Packaging Department The Advanced Manufacturing Processes Laboratory (AMPL) Sandia National Laboratories	Kirkland AFB Albuquerque, NM Robert L. Poole, Manager, (505) 845-9200 Janda Panitz (505) 845-8604 (JKPANIT@scandia.gov) John Zich (505) 845-8571 (JLZICH@scandia.gov)
Advanced Thin Film Technology	Thinfilms Manufacturing Facilities Hillsborough Business Park Bldg #13, 6 Illene Court Belle Mead, NJ 08502
Motson Precision Printing and Finishing	1717 Bethlehem Pike Flourtown, PA 19031-1110 (215) 233-0500
Thin Film Technology, Inc.	153 Industrial Way Buellton, CA 93427 (805) 688-4949
Precision Painting	1005 Orangethorpe Ave. Anaheim, CA 92801 (714) 630-0540

Table 15. Conductive Coating Suppliers for Carbon Fiber MAV Body.

LIST OF REFERENCES

1. Brown, W. C., "The Early History of Wireless Power Transmission and a Discussion of Transportronics for the Future," IEEE-MTTS Wireless Power Transmission Workshop Notes, San Francisco, CA, 17 June 1996.
2. Brown, W.C., "Thermionic Diode Rectifier," in *Microwave Power Engineering, Volume I*, E.C. Okress, editor, pp. 295-298, Academic Press, New York, 1968.
3. Benford, J. and Dickinson, R., "Space Propulsion and Power Beaming using Millimeter Systems," *Society of Photo-Optical Instrumentation Engineers (SPIE)*, San Diego, July 1995.
4. Kaya, Nobuyuki, "WPT'95 Workshop and Demonstration of Microwave Power Transmission to Airship (Ether)," *IEEE Microwave Theory and Technology (MTT-S) International Symposium Workshop on Wireless Power Transfer*, San Francisco, 1996.
5. Hawkins, Joe, "The SABER (Semi-Autonomous BEam Rider) Microwave-Powered Helicopter Project," *IEEE Microwave Theory and Technology (MTT-S) International Symposium Workshop on Wireless Power Transfer*, San Francisco, 1996.
6. Jenn, D.C. and Vitale, R.L., "Wireless Power Transfer for a Micro Remotely Piloted Vehicle," *IEEE International Symposium on Circuits and Systems (ISCAS)*, Monterey, CA, May 31-June 3, 1998.
7. Jenn, D.C., "RPV," *IEEE Potentials*, Vol 16, No. 5, pp. 20-22, December 1997.
8. *Proceeding of the First International Conference on Emerging Technologies for Micro Air Vehicles*, Georgia Institute of Technology, Atlanta, GA, February 19-20, 1997.
9. Gibson, T. B., "Propagation Loss Study and Antenna Design for the Micro-Remotely Powered Vehicle," Master's Thesis, Naval Postgraduate School, Monterey, CA, September 1995.
10. Sedra, A.S. and Smith, K.C., *Microelectronic Circuits*, Oxford University Press, New York, NY, 1991.
11. George, R.H., "Solid State Power Rectifiers," in *Microwave Power Engineering, Volume I*, E.C. Okress, editor, pp. 275-294, Academic Press, New York, 1968.
12. McSpadden, J.O., Yoo, T. and Chang, K., "Theoretical and Experimental Investigation of a Rectenna Element for Microwave Power Transmission," *IEEE Transactions on Microwave Theory and Techniques*, Vol. 40 No. 12, pp. 2359-55, Dec 1992.

13. Pozar, D.M., *Microwave Engineering*, Addison-Wesley Publishing Company, Inc., Reading, MA, June 1990.
14. Balanis, C.A., *Antenna Theory, Analysis and Design*, John Wiley & Sons, New York, NY, 1982.
15. Collin, R.E., *Antennas and Radiowave Propagation*, McGraw-Hill, Inc., New York, NY, 1985.
16. Brown, G.H. and Woodward, O.M., "Experimentally Determined Impedance Characteristics of Cylindrical Antennas," *Proceeding of Institute of Radio Engineers (IRE)*, Vol. 33, pp. 257-262, 1945.
17. Harrington, R.F., *Field Computation by Moment Methods*, Macmillan, New York, NY, 1968.
18. Nittany Scientific, Inc., GNEC-4 Version 1.1 Antenna Analysis Software User's Manual, Nittany Scientific, Inc., 1700 Airline Highway, Suite 361, Hollister, CA, 90523 USA, November 1997.
19. Burke, G.J., Numerical Electromagnetics Code – NEC-4, Method of Moments, Lawrence Livermore National Laboratory, Report UCRL-MA-109338, Livermore, CA, January 1992.
20. Hewlett-Packard Company, Fundamentals of RF and Microwave Power Measurements, Hewlett Packard Application Note 64-1A, Hewlett-Packard Company, Inc., Palo Alto, CA, June 1998.
21. Krause, P.C., Wasynczuk, O. and Sudhoff, S.D., *Analysis of Electric Machinery*, McGraw Hill Inc, New York, NY, 1986.
22. IEEE Standard C95.1-1991, IEEE Standard for Safety levels with Respect to Human Exposure to Radio Frequency Electromagnetic Fields, 3 kHz to 300 GHz, Institute of Electrical and Electronic Engineers, Inc., 345 East 47th Street, New York, NY, 10017 USA, April 27, 1992.
23. Lee, Gary M., Barrett, Ronald, and Jenn, David, MRPV Design Study Final Report, Lutronix Corporation, Del Mar, CA, 1996.
24. Yang, X., Chiochetti, J., Papadopoulos, D., and Susman, L., "Fractal Antenna Elements and Arrays," *Applied Microwave & Wireless*, Vol 11, No. 5, pp. 34-46, May 1999.

INITIAL DISTRIBUTION LIST

	No. Copies
1. Defense Technical Information Center 8725 John J. Kingman Rd., STE 0944 Ft. Belvoir, VA 22060-6218	2
2. Dudley Knox Library Naval Postgraduate School 411 Dyer Rd. Monterey, CA 93943-5101	2
3. Chairman, Code EC..... Department of Electrical and Computer Engineering Naval Postgraduate School Monterey, CA 93943-5121	1
4. Professor David C. Jenn, Code EC/Jn..... Department of Electrical and Computer Engineering Naval Postgraduate School Monterey, CA 93943-5121	3
5. Professor Jeffery B. Knorr, Code EC/Ko..... Department of Electrical and Computer Engineering Naval Postgraduate School Monterey, CA 93943-5121	2
6. Robert L. Vitale, Code EC Department of Electrical and Computer Engineering Naval Postgraduate School Monterey, CA 93943-5121	4
7. Space and Naval Warfare System Command..... Department of the Navy PMW-178 Attn: CAPT. Connel Washington, D.C. 20363-5100	2
8. Dr. Gary Lee Lutronix Corporation 13627 Potofino Drive Del Mar, CA 92014	1

32 473NP6 593
TH
11/02 22527-200 NLE



DUDLEY KNOX LIBRARY



3 2768 00404071 7